

Electronic Thesis and Dissertation Repository

---

8-14-2012 12:00 AM

## Chiral Separation of Racemic Mandelic Acid by the Coupling Crystallization Process and Simulated Moving Bed Technology

Shimin Mao, *The University of Western Ontario*

Supervisor: Dr. Ajay K. Ray, *The University of Western Ontario*

Joint Supervisor: Dr. Sohrab Rohani, *The University of Western Ontario*

A thesis submitted in partial fulfillment of the requirements for the Doctor of Philosophy degree in Chemical and Biochemical Engineering

© Shimin Mao 2012

Follow this and additional works at: <https://ir.lib.uwo.ca/etd>

 Part of the [Process Control and Systems Commons](#)

---

### Recommended Citation

Mao, Shimin, "Chiral Separation of Racemic Mandelic Acid by the Coupling Crystallization Process and Simulated Moving Bed Technology" (2012). *Electronic Thesis and Dissertation Repository*. 690.  
<https://ir.lib.uwo.ca/etd/690>

This Dissertation/Thesis is brought to you for free and open access by Scholarship@Western. It has been accepted for inclusion in Electronic Thesis and Dissertation Repository by an authorized administrator of Scholarship@Western. For more information, please contact [wlsadmin@uwo.ca](mailto:wlsadmin@uwo.ca).

# **Chiral Separation of Racemic Mandelic Acid by the Coupling Crystallization Process and Simulated Moving Bed Technology**

(Spine title: Chiral Separation by the Coupling Crystallization and Simulated Moving  
Bed process)

(Thesis format: Article Integrated)

By

**Shimin Mao**

Graduate Program in  
Chemical and Biochemical Engineering

A thesis submitted in partial fulfillment  
of the requirements for the degree of  
Doctor of Philosophy

The School of Graduate and Postdoctoral Studies  
The University of Western Ontario  
London, Ontario, Canada

© Shimin Mao 2012

## CERTIFICATE OF EXAMINATION

Joint Supervisor

Dr. Ajay K. Ray

Dr. Sohrab Rohani

Supervisory Committee

Dr. Jesse Zhu

Dr. Madhumita B. Ray

Examiners

Dr. Hector Budman

Dr. Mahi Singh

Dr. Jesse Zhu

Dr. Anand Prakash

The thesis by

**Shimin Mao**

entitled:

**Chiral Separation of Racemic Mandelic Acid by the Coupling  
Crystallization Process and Simulated Moving Bed Technology**

is accepted in partial fulfillment of the  
requirements for the degree of  
Doctor of Philosophy

---

Date

---

Chair of the Thesis Examination Board

## Abstract

Chirality is a major concern in the modern pharmaceutical, food and agricultural industries. The importance of enantiopure drugs has risen dramatically in recent years due to Food and Drug Administration regulations requiring that all chiral bioactive molecules must be isolated and tested for the efficacy and safety, and have to be as pure as possible containing a single pure enantiomer. There are essentially three strategies that can be applied to obtain pure isomers: (a) extraction from plants and animal materials (b) enantio-selective asymmetric synthesis so that only one isomer is formed in the first place, or (c) making a racemate and finding a method for separating the enantiomers. Only few enantiomers exist in nature and most of them are racemates. A highly efficient chiral asymmetric synthesis route would be the ideal situation, but it usually takes about 10-15 years to develop a synthesis recipe. Hence, the best strategy would be to synthesize the drug in racemate form and separate the isomers to produce single pure enantiomer.

Among the variety of enantioseparation methods, chromatography and crystallization are the most dominant methods for the recovery of pure enantiomers. However, both methods have limitations. Crystallization cannot obtain enantiopure enantiomers from the racemic compound directly. In Simulated Moving Bed (SMB), solvent consumption increases exponentially if desired purity requirement is close to 100%. In this work, the coupling of SMB for enrichment followed by direct crystallization is applied for the chiral resolution to circumvent limitations of each method. In order to take advantage of both the processes, SMB chromatography is used for partial enrichment thereby reducing solvent consumption followed by direct crystallization to obtain 100% pure enantiomers.

Here, the chiral resolution of mandelic acid (MA) as racemic compound was considered to investigate the performance of the hybrid SMB-crystallization process theoretically as well as experimentally. The solubility and metastable zone limit of (*R,S*)-MA and (*R*)-MA in water and the crystallization kinetics parameters of (*R,S*)-MA and (*R*)-MA by optimization of the crystallization model based on the necessary experimental data collected in unseeded cooling batch crystallizers were determined. For the SMB part, the choice of mobile phase and determination of binary competitive equilibrium isotherms parameters of (*R,S*)-MA and the experimental and modeling studies of SMB process have also been accomplished.

### **Keywords:**

Mandelic acid, racemic compound solubility, metastable zone, cooling crystallization, parameter estimate, nucleation and growth kinetics, FBRM, ATR-FTIR, mobile phase composition, competitive adsorption isotherms, inverse method, frontal analysis, simulated moving bed.

## Co-Authorship Statement

**Chapter 3:** A version of chapter 3 was accepted by Journal of Separation Science:

- ❖ Mao, S.; Zhang, Y; Rohani, S.; Ray, A.K. Chromatographic Resolution and Isotherm Determination of (*R,S*)-Mandelic Acid on Chiralcel OD Column, Accepted for publication in the Journal of Separation Science.

The experiments were designed and conducted by the author. The manuscript was written by the author and revised by Dr. Y. Zhang and Dr. A.K. Ray. And the experiment materials were provided by Dr. A. K. Ray and Dr. S. Rohani.

**Chapter 4:** A version of chapter 4 was submitted to Separation and Purification Technology:

- ❖ Mao, S.; Zhang, Y; Ray, A.K.; Rohani, S. Enantioseparation of Racemic Mandelic Acid by Simulated Moving Bed Chromatography Using Chiralcel OD Column, Submitted to Journal of Separation Science.

Writing the manuscript, collecting the data, designing and performing experiments are completed by the author. Dr. Y. Zhang and Dr. A.K. Ray revised the manuscript. Dr. S. Rohani also provided some suggestion on the manuscript.

**Chapter 5:** A version of chapter 5 was published as:

- ❖ Mao, S.; Zhang, Y; Rohani, S.; Ray, A.K. Kinetics of (*R,S*)-Mandelic Acid and (*R*)-Mandelic Acid in an unseeded cooling batch crystallizer, Journal of Crystal Growth, 312(22), 3340-3348(2010).

All data were collected by the author. The design of the experiments was performed by Dr. Y. Zhang and author under the supervision of Dr. S. Rohani. The manuscript was written by the author and revised by Dr. Y. Zhang and Dr. S. Rohani. Dr. A.K. Ray also provided some suggestion on the manuscript.

**To my parents, grandparents and aunt for endless  
support and love**



## **Acknowledgments**

Acknowledgement and many thanks are due to Dr. Ajay K. Ray and Dr. Sohrab Rohani, my supervisors, for their enthusiasm, patience and advice, and for giving me the continuous support and encouragement on the occasions that I felt frustrated.

I would also like to extend my gratitude to Dr. Yan Zhang who taught me how to do the research from scratch. Many thanks to Dr. Quan He, Dr. Jie Lu and Dr. Milana Trifkovic for their help during my Ph.D study. And I would like to thank Ghodsieh Malekshoar, Housyn Mahmoud, Nillohit Mitra Ray, Noshin Hashim, Pankaj Chowdhury, Pegah Saremirad, Fate Hashemi and Souheil Afara for providing me with a good research environment.

I would like to extend special thanks to my parents, my grandparents and my aunt for their endless love and extreme support and patience throughout this process. I couldn't have done this without you.

# Table of Contents

CERTIFICATE OF EXAMINATION .....	ii
Abstract .....	iii
Co-Authorship Statement.....	v
Acknowledgments.....	viii
Table of Contents .....	ix
List of Tables .....	xiii
List of Figures .....	xv
Nomenclature .....	xix
Chapter 1 .....	1
Introduction.....	1
1.1 Background.....	2
1.2 Research objective and approaches .....	7
1.3 Thesis organization.....	10
1.4 Contribution .....	11
1.5 Reference .....	13
Chapter 2.....	16
Literature Review.....	16
2.1 Simulated moving bed (SMB) .....	17
2.1.1 Background of SMB .....	17
2.1.2 Chromatography .....	18
2.1.3 Continuous counter-current chromatography .....	19
2.1.4 Column model for SMB.....	24
2.1.5 Competitive adsorption isotherm models .....	27

2.1.6	Node model.....	30
2.1.7	Design strategy for SMB .....	31
2.1.8	Performance parameters.....	36
2.2	Direct crystallization.....	38
2.2.1	Background of crystallization.....	38
2.2.2	The mathematical model of crystallization process.....	44
2.2.3	Direct crystallization for the pure enantiomers.....	48
2.3	Coupling of simulated moving bed chromatography and direct crystallization ...	54
2.4	Reference .....	55
Chapter 3.....		66
Chromatographic Resolution and Isotherm Determination of ( <i>R,S</i> )-Mandelic Acid on Chiralcel-OD Column .....		66
3.1	Introduction.....	67
3.2	Modeling.....	70
3.2.1	Competitive modified Langmuir adsorption isotherm model.....	70
3.2.2	Column model.....	71
3.2.3	Isotherm parameters estimation .....	73
3.3	Experimental.....	73
3.3.1	Equipment.....	73
3.3.2	Materials .....	74
3.3.3	Solubility measurement of ( <i>R,S</i> )-MA .....	75
3.3.4	Resolution of ( <i>R,S</i> )-MA and isotherm determination .....	75
3.4	Results and discussion .....	78
3.4.1	Choice of mobile phase.....	78
3.4.2	Parameters estimation, optimization and validation for competitive adsorption isotherm.....	82

3.5 Conclusions.....	91
3.6 References.....	93
Chapter 4.....	97
Enantioseparation of Racemic Mandelic Acid by Simulated Moving Bed Chromatography Using Chiralcel OD Column.....	97
4.1 Introduction.....	98
4.2 Theoretical background .....	100
4.2.1 Isotherm model .....	100
4.3 SMB model.....	101
4.3.1 SMB modeling.....	101
4.3.2 Design of SMB .....	103
4.4 Experiment setting .....	107
4.4.1 Materials and equipments .....	107
4.4.2 SMB operation.....	108
4.5 Results and discussion .....	109
4.5.1 Isotherm parameters and rate coefficients .....	109
4.5.2 Complete separation region .....	110
4.5.3 The effects of operating conditions on SMB performance.....	110
4.5.4 Validation of the SMB model with the experimental data .....	121
4.6 Conclusion .....	125
4.7 Reference .....	126
Chapter 5.....	128
Kinetics of ( <i>R,S</i> )- and ( <i>R</i> )-Mandelic Acid in an Unseeded Cooling Batch Crystallizer. 128	
5.1 Introduction.....	129
5.2 Materials and methods .....	131
5.2.1 Calibration for IR spectrum .....	132

5.2.2	Solubility determination.....	134
5.2.3	Measurement of metastable zone limit .....	134
5.2.4	Unseeded cooling batch crystallization .....	134
5.3	Modeling.....	136
5.4	Optimization and crystallization kinetics parameter estimation.....	138
5.5	Results and discussion .....	139
5.5.1	Calibration model.....	139
5.5.2	Solubility.....	144
5.5.3	Metastable zone width (MSZW).....	145
5.5.4	Kinetics estimation, optimization and validation.....	147
5.5.5	Supersaturation .....	150
5.6	Conclusion .....	156
5.7	Reference .....	157
Chapter 6	.....	160
Conclusions and Recommendations	.....	160
6.1	Conclusions.....	161
6.1.1	Simulated moving bed .....	161
6.1.2	Crystallization.....	163
6.2	Recommendation for future work.....	165
Appendix A: Introduction to genetic algorithm	.....	167
Appendix B: Column dimension	.....	170
Appendix C: Copyrighted material and permissions	.....	171
Curriculum Vitae	.....	173

# List of Tables

## Chapter 2

Table 2- 1: Relationship between a TMB and SMB .....	24
--	----

## Chapter 3

Table 3- 1: The operating conditions for the isotherm measurements.....	76
---	----

Table 3- 2: The selectivity ( $\alpha$ ) and resolution ( $R_s$ )of the band profiles .....	80
---	----

Table 3- 3: Axial dispersion coefficient values with different flow rates of mobile phase .....	83
--	----

Table 3- 4: Competitive modified Langmuir isotherm parameters .....	84
---	----

Table 3- 5: The experimental data for frontal analysis.....	90
---	----

## Chapter 4

Table 4- 1: Transient model equations for SMB chromatography .....	102
--	-----

Table 4- 2: The void fraction of each column in SMB unit.....	107
---	-----

Table 4- 3: Isotherm parameters and rate coefficients of ( <i>R</i> )- and ( <i>S</i> )-MA in SMB column .....	109
---	-----

Table 4- 4: Operation conditions and parameters for the SMB experiments .....	111
---	-----

Table 4- 5: Separation performance of experiments on SMB .....	112
--	-----

## Chapter 5

Table 5- 1: Mandelic acid solutions used for calibration model.....	133
---	-----

Table 5- 2: Operating parameters of cooling crystallization of ( <i>R</i> , <i>S</i> )-MA and ( <i>R</i> )-MA	135
---	-----

Table 5- 3: Estimated kinetics parameters .....	148
Table 5- 4: Comparison of nolume weighted mean size.....	150

# List of Figures

## Chapter 1

Figure 1- 1: Sketch of two enantiomers.....	2
Figure 1- 2: Typical binary phase diagrams illustrating the three types of racemate (1. Conglomerate, 2. Racemic compound, 3. Pseudoracemate) [9]. .....	4
Figure 1- 3: The scheme of the coupling process of SMB and crystallization process for resolution of mandelic acid. ....	8

## Chapter 2

Figure 2- 1: Analogy for elution chromatography.....	19
Figure 2- 2: Analogy for countercurrent elution chromatography.....	20
Figure 2- 3: Typical configuration of the true moving bed. ....	22
Figure 2- 4: Typical configuration of the simulated moving bed. ....	23
Figure 2- 5: Triangle theory: the different separation regimes on the ( $m_2, m_3$ ) plane for the binary separation with linear adsorption isotherm. ....	34
Figure 2- 6: Triangle theory: the different separation regimes on the ( $m_2, m_3$ ) plane for the binary separation with Langmuir adsorption isotherm. ....	36
Figure 2- 7: Equilibrium phase diagram, unseeded crystallization (dash line) and seeded crystallization (dot line). ....	41
Figure 2- 8: The setup of the crystallization experiment: 1.ATR-FTIR, 2.FBRM, 3.ATR-FTIR monitor, 4.FBRM monitor, 5. Double jacketed 200 mL glass crystallizer, 6.Magnetic stirring bar, 7. Magnetic stirrer, 8.Bath circulator...	51
Figure 2- 9: Principle of direct crystallization for racemic compound systems. ....	53



### Chapter 3

Figure 3- 1: Molecular structure of mandelic acid.....	68
Figure 3- 2: Binary phase diagram of the racemic mandelic acid [16].....	70
Figure 3- 3: Solubility of ( <i>R,S</i> )-MA with different ethanol proportions in the mobile phase.....	79
Figure 3- 4: Influence of IPA proportion in the mobile phase on the elution profiles of ( <i>R</i> )-MA and ( <i>S</i> )-MA.....	80
Figure 3- 5: Influence of TFA proportion in the mobile phase on the retention and enantioselectivity of ( <i>R,S</i> )-MA. ....	81
Figure 3- 6: Best-fit of competitive modified Langmuir isotherm. ....	85
Figure 3- 7: Verification of the best-fit isotherm parameters with lower elution flow rate. ....	87
Figure 3- 8: Verification of the best-fit isotherm parameters with medium elution flow rate.....	88
Figure 3- 9: Verification of the best-fit isotherm parameters with higher elution flow rate. ....	89
Figure 3- 10: The competitive modifier Langmuir isotherm models for ( <i>R</i> )- and ( <i>S</i> )-MA obtained by frontal analysis and inverse method, where $q_1=f(c_1, c_2=const)$ and $q_2=f(c_1=const, c_2)$ .....	91

### Chapter 4

Figure 4- 1: Schematic diagram of an open loop four section SMB unit. ....	99
Figure 4- 2: Separation of ( <i>R,S</i> )-MA racemic compound using Chiralcel OD SMB system. Regions of ( $m_2, m_3$ ) plane based on the purity of both outlet stream over 99% when the feed concentration is 30g/L and column configuration is	

1/2/2/1. The numbers with the parenthesis in areas present the four different separation regions: (1) pure raffinate and extract; (2) only pure extract; (3) only pure raffinate; (4) no pure raffinate and extract.....	105
Figure 4- 3: SMB performance as a function of switching time.....	113
Figure 4- 4: SMB performance as a function of feed concentration.....	115
Figure 4- 5: SMB performance as a function of feed flow rate.....	116
Figure 4- 6: SMB performance as a function of extract flow rate.....	118
Figure 4- 7: SMB performance as the column configuration. ....	120
Figure 4- 8: The experimental and simulated separation performance of Run 2.....	122
Figure 4- 9: The experimental and simulated separation performance of Run 6.....	123
Figure 4- 10: The experimental and simulated separation performance of Run 12.....	124

## Chapter 5

Figure 5- 1: IR spectra of mandelic acid water solutions with different concentrations. (a, raw data; b, intensity difference with respect to the intensity height at $1136\text{ cm}^{-1}$ ) .....	141
Figure 5- 2: IR spectra of mandelic acid water solution at various temperatures. (a, raw data; b, intensity difference with respect to the intensity height at $1136\text{ cm}^{-1}$ ) .....	142
Figure 5- 3: Concentration measurement from gravimetry method and from the ATR-FTIR calibration model at different temperatures.....	143
Figure 5- 4: Solubility curves for ( <i>R</i> )-MA and ( <i>R,S</i> )-MA in water. ....	144
Figure 5- 5: Metastable zone limits of ( <i>R</i> )-MA and ( <i>R,S</i> )-MA in water.....	146

Figure 5- 6: ( <i>R</i> )-MA and ( <i>R,S</i> )-MA concentration profiles by experimental measurement and model prediction.....	149
Figure 5- 7: Model validation based on concentration profiles. ....	149
Figure 5- 8: Effect of initial concentration on the nucleation and growth rate of ( <i>R</i> )-MA and ( <i>R,S</i> )-MA. ....	151
Figure 5- 9: Comparison of nucleation and growth rates of ( <i>R</i> )-MA and ( <i>R,S</i> )-MA with the same initial saturated temperature.....	153
Figure 5- 10: Effect of cooling rate on the nucleation and growth rates of ( <i>R,S</i> )-MA. ...	155

# Nomenclature

## Chapter 2

$a$	Activity coefficient of a component
$a^*$	Activity coefficient of a saturation solution
$a_0$	Particle size distribution of the seeds based on the uniform crystal shape
$B$	Nucleation rate (no./ $(L \cdot \text{min})$ )
$b$	Equilibrium constant (L/g)
$c$	Solution concentration (g/L) Note: solute mass per solvent volume
$c^*$	Solubility (g/L)
$c_0$	Initial concentration (g/L)
$\Delta c$	Supersaturation (g/L)
$D_a$	Apparent dispersion coefficient ( $\text{cm}^2/\text{min}$ )
$D_L$	Dispersion coefficients ( $\text{cm}^2/\text{min}$ )
$DR$	Desorbent requirement (g mobile phase /g feed)
$E_b$	Activation energy of nucleation (kJ/mol)
$E_g$	Activation energy of growth (kJ/mol)
$f$	Function of the adsorption isotherm
$G$	Growth rate (m/min)
$H$	Coefficient for the non-specific adsorption sites
$k_b$	Nucleation rate coefficient (no./ $(\text{m}^3 \cdot \text{min})$ )
$k_{b0}$	Nucleation frequency factor
$k_g$	Growth rate coefficient (m/min)
$k_{g0}$	Growth frequency factor
$k_m$	Lumped rate coefficient ( $\text{s}^{-1}$ )
$k_v$	Volume shape factor
$L$	Column length (cm) in SMB and Crystal size (m) in crystallization
$L_{max}$	Maximum size of the seeds (m)
$L_{min}$	Minimum size of the seeds (m)
$MA$	Mandelic acid

$M_T$	Magma or suspension density (g/g of solvent)
$m$	Flow rate ratio
$m_i$	$i$ th moment of the crystal size distribution ( $m^i/L$ solvent)
$n$	Population density (no/ $\mu\text{m}$ . L)
$Pr$	Productivity (g feed/(g stationary phase·min))
$Pu$	Purity of the extract or raffinate stream (%)
$Q$	Mobile phase flow rate (mL/min)
$Q_s$	Solid phase flow rate (mL/min)
$q^*$	Adsorbed amount in the stationary phase (g/L)
$q_s$	Saturation capacities (g/L)
$R$	Universal gas constant (J/(mol·K))
<b>Rac</b>	Racemic compound
<b>Re</b>	Recovery of the components (%)
<b>SMB</b>	Simulated moving bed
$S_s$	Fundamental supersaturation (g/L)
$T$	absolute temperature (K or °C)
$T_{end}$	End temperature (°C)
$T_{start}$	Start temperature (°C)
$T_0$	initial temperature (°C)
<b>TMB</b>	True moving bed
$t$	Time (min)
$t^*$	Switching time (min)
$t^R$	Retention time (min)
$t_0$	Holdup time of the column (min)
$u$	Interstitial fluid velocity (cm/min)
$V$	Geometric column volume (mL)
$V^D$	Dead volume (mL)
<b>Greek symbols</b>	
$\nu$	Exponent constant
$\varepsilon$	Void fraction of the column
$\varepsilon_p$	Intraparticle void fraction

$\rho_s$	Solid phase density (g/cm <sup>3</sup> )
$\rho_c$	Crystal density (g/m <sup>3</sup> )
$\mu$	Chemical potential (J/mol)
$\mu_0$	Standard chemical potential (J/mol)

***Subscripts and superscripts***

<b><i>1</i></b>	Non-selective sites
<b><i>2</i></b>	Selective sites
<b><i>A</i></b>	More retained component of racemic compound (( <i>R</i> )-Mandelic acid)
<b><i>B</i></b>	Less retained component of racemic compound (( <i>S</i> )-Mandelic acid)
<b><i>b</i></b>	Nucleation order
<b><i>D</i></b>	Desorbent port
<b><i>E</i></b>	Extract port
<b><i>F</i></b>	Feed or feed port
<b><i>g</i></b>	Growth order
<b><i>i</i></b>	Component index ( <i>i</i> =A or B)
<b><i>k</i></b>	Section index
<b><i>R</i></b>	Raffinate port
<b><i>T</i></b>	Total
<b><i>z</i></b>	Space coordinate

**Chapter 3**

<b><i>b</i></b>	Equilibrium constants (L/g)
<b><i>c</i></b>	Solution concentration (g/L) Note: solute mass per solvent volume
<b><i>c<sub>m</sub></i></b>	Concentration of component in the first plateau (g/L)
<b><i>D<sub>L</sub></i></b>	Dispersion coefficients (cm <sup>2</sup> /min)
<b><i>D<sub>m</sub></i></b>	Molecular diffusion coefficient of the solute in the mobile phase
<b><i>d<sub>p</sub></i></b>	Diameter of the particle size (μm)
<b><i>IPA</i></b>	Isopropyl alcohol
<b><i>TFA</i></b>	Trifluoroacetic acid
<b><i>k</i></b>	Total number of the experimental data
<b><i>k<sub>v</sub></i></b>	Lumped rate coefficient (s <sup>-1</sup> )

$L$	Column length (cm)
$m$	Coefficient for the non-specific adsorption sites
$MA$	Mandelic acid
$q^*$	Adsorbed amount in the stationary phase (g/L)
$q_s$	Saturation capacities (g/L)
$R$	R-Mandelic acid
$R_s$	Resolution
$S$	S- Mandelic acid
$t$	Time (min)
$t_p$	Length of a rectangular injection (min)
$t_0$	Holdup time of the column (min)
$t_1$	Retention time of the first breakthrough fronts (min)
$t_2$	Retention time of the second breakthrough fronts (min)
$t_p$	Length of a rectangular injection (min)
$u$	Interstitial fluid velocity (cm/min)
$V_a$	Molar volume (cm <sup>3</sup> /mol)
$w$	Molar fraction
$z$	Space coordinate

***Greek symbols***

$\alpha$	Selectivity
$\varepsilon$	Void fraction of the column
$\mu$	Viscosity of solvent (kg/(s·m))

***Subscripts and superscripts***

$cal$	Calculated results from the model
$exp$	Experiment results
$F$	Feed
$i$	Component ( $i=1$ or $2$ , 1 represent (S)-MA and 2 represent (R)-MA)

**Chapter 4**

$b$	Equilibrium constants (L/g)
$c$	Solution concentration (g/L)

$c_F$	Feed concentration of each components (g/ L)
$D_L$	Dispersion coefficients (cm <sup>2</sup> /min)
$H$	Coefficient for the non-specific adsorption sites
$k_v$	Lumped rate coefficient (s <sup>-1</sup> )
$L$	Column length (cm)
$m$	Flow rate ratio
$MA$	Mandelic acid
$N$	Number of switches
$N_T$	Total number of the columns
$Pu$	Purity of the extract or raffinate stream (%)
$Q$	Mobile phase flow rate (mL/min)
$q^*$	Adsorbed amount in the stationary phase (g/ L)
$q_s$	Saturation capacities (g/ L)
$t$	Time (min)
$t^*$	Switching time (min)
$t_0$	Holdup time of the column (min)
$u$	Interstitial fluid velocity (cm/min)
$V$	geometric column volume (cm <sup>3</sup> )
$V^D$	Dead volume (cm <sup>3</sup> )
$x$	Column number
$z$	Space coordinate (cm)

***Greek symbols***

$\varepsilon$  Void fraction of the column

***Subscripts and superscripts***

$A$	More retained component of racemic compound (( <i>R</i> )-Mandelic acid)
$B$	Less retained component of racemic compound (( <i>S</i> )-Mandelic acid)
$Ex$	Extract stream
$F$	Feed
$g$	Section index
$i$	Component index ( $i=A$ or $B$ )
$j$	Column index



<b><i>Ra</i></b>	Raffinate stream
<b><i>Re</i></b>	Recovery of the components (%)

## Chapter 5

<b><i>ABS</i></b>	Absorbance
<b><i>ATR-FTIR</i></b>	Attenuated total reflection Fourier transform infrared spectroscopy
<b><i>B</i></b>	Nucleation rate (no/ L·s)
<b><i>C</i></b>	Solute concentration (g/ L) Note: solute mass per solvent volume
<b><i>C*</i></b>	Solubility of solution (g/L)
<b><i>C*<sub>TI</sub></i></b>	Concentration of solution at the metastable zone limit(g/L)
<b><math>\Delta C</math></b>	Supersaturation (g/L)
<b><math>\Delta C_{max}</math></b>	Maximal attainable supersaturation (g/L)
<b><i>E<sub>b</sub></i></b>	Nucleation activation energy (kJ/mol)
<b><i>E<sub>g</sub></i></b>	Growth activation energy (kJ/mol)
<b><i>FBRM</i></b>	Focused beam reflectance measurement
<b><i>G</i></b>	Growth rate ( $\mu\text{m/s}$ )
<b><i>k<sub>b</sub></i></b>	Nucleation rate coefficient
<b><i>k<sub>b0</sub></i></b>	Nucleation frequency factor
<b><i>k<sub>g0</sub></i></b>	Growth frequency factor
<b><i>k<sub>g</sub></i></b>	Linear growth rate coefficient
<b><i>k<sub>v</sub></i></b>	Volume shape factor
<b><i>L</i></b>	Crystal size ( $\mu\text{m}$ )
<b><i>L<sub>[4,3]</sub></i></b>	Volume weighted mean particle size ( $\mu\text{m}$ )
<b><i>MA</i></b>	Mandelic acid
<b><i>n</i></b>	Population density (no/ $\mu\text{m}$ . L)
<b><i>N</i></b>	Number of experimental data
<b><i>P</i></b>	Absorbance value of the peak
<b><i>R</i></b>	Gas constant(8.314 J/(K·mol))
<b><i>t</i></b>	Time (s)
<b><i>T</i></b>	Temperature of solution ( $^{\circ}\text{C}$ )
<b><i>T<sub>l</sub></i></b>	Temperature at metastable zone limit ( $^{\circ}\text{C}$ )

$T_s$	Temperature of the saturation concentration (°C)
$\Delta T_{max}$	Maximal attainable supercooling of the metastable zone (°C)

***Greek symbols***

$\Delta$	Differential, difference
$\mu$	$i$ th moment of the crystal size distribution (m <sup>3</sup> /L)
$\rho_c$	Crystal density (g/μm <sup>3</sup> )

***Subscripts and superscripts***

$b$	Nucleation order
$cal$	Results calculated by the crystallization model
$exp$	Experiment results measured for ATR-FTIR
$g$	Growth order
$grav$	Results measured by the gravimetric method

# **Chapter 1**

## **Introduction**

## 1.1 Background

Chirality is referred to the geometric property of an object that cannot be superposed onto its' mirror image. The original object and its mirror image are considered as the two enantiomorphous forms of the chiral object which could be a hand or a snail shell. In chemistry, that object is indicated as the molecules, and the two enantiomorphous forms are named as enantiomers. A chiral center shown in Figure 1-1 is composed of a carbon atom and four different atoms or groups. The chiral molecules are commonly found in nature, such as amino acids, sugar and enzymes, even DNAs.

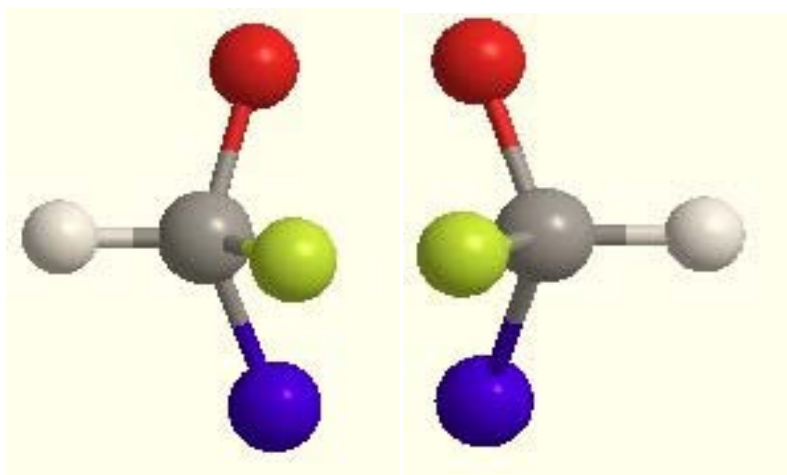


**Figure 1- 1: Sketch of two enantiomers.**

Chirality has attracted more and more attention in the modern pharmaceutical, food and agricultural industries. The sale of chiral drugs is close to one-third of all drug sales worldwide. Ordinary chemical production methods for chiral drugs produce a racemic mixture containing enantiomers having identical chemical compositions but different

structural orientations in space. It is quite common to find that one isomeric form has a therapeutic effect on the human body while its enantiomer is ineffective or even harmful. The tragedy caused by thalidomide happened in 1960s' is a frequently quoted example: (*R*)-thalidomide was the beneficial agent for preventing morning sickness in pregnant women while the other caused serious birth defects [1]. Hence, there is obvious benefit from separating the two enantiomers to enhance drug's safety and tolerability. The importance of enantiopure drugs has risen dramatically in recent years due to new FDA regulations requiring that all chiral bioactive molecules must be isolated and tested for the efficacy and safety, and has to be as pure as possible containing a single pure enantiomer [2]. More and more other countries have also established guidelines on development and marketing of enantiopure drugs. Until 2007, FDA approved 70% of the new small molecules which had one chiral center at least [3]. The percentage of single-enantiomeric drugs in the market increased from 27% in 1996 to about 39% in 2002 [4]. A survey by Frost & Sullivan estimated that the worldwide revenue of single-enantiomer compounds was about \$4.8 billion in 1999 and would reach about \$15 billion by the end of 2009 [5]. Regulation and market sales stimulate the development of the techniques to get pure enantiomers in industry and academic research.

Not all the chiral compounds can be found in pure enantiomer forms. Many chiral compounds are racemates defined as the compounds composed of two enantiomers with equimolar. Roozeboom [6] classified the racemates into three fundamental types by their melting points: conglomerate, racemic compound and pseudoracemate (solid solution), which are shown in Figure 1-2. Conglomerate is a mechanical mixture with equimolecular of two enantiomers. For the racemic compound, the two enantiomers

coexist in the same unit cell with an order 1:1 ratio, which causes the difficult chiral separation. However, more than 90% of racemates belong to the racemic compound [7]. As homogenous racemic solid solution, pseudoracemate is racemic modification in the solid state and composed of the equal amount of two enantiomers disarrayed in the crystal lattice [8].

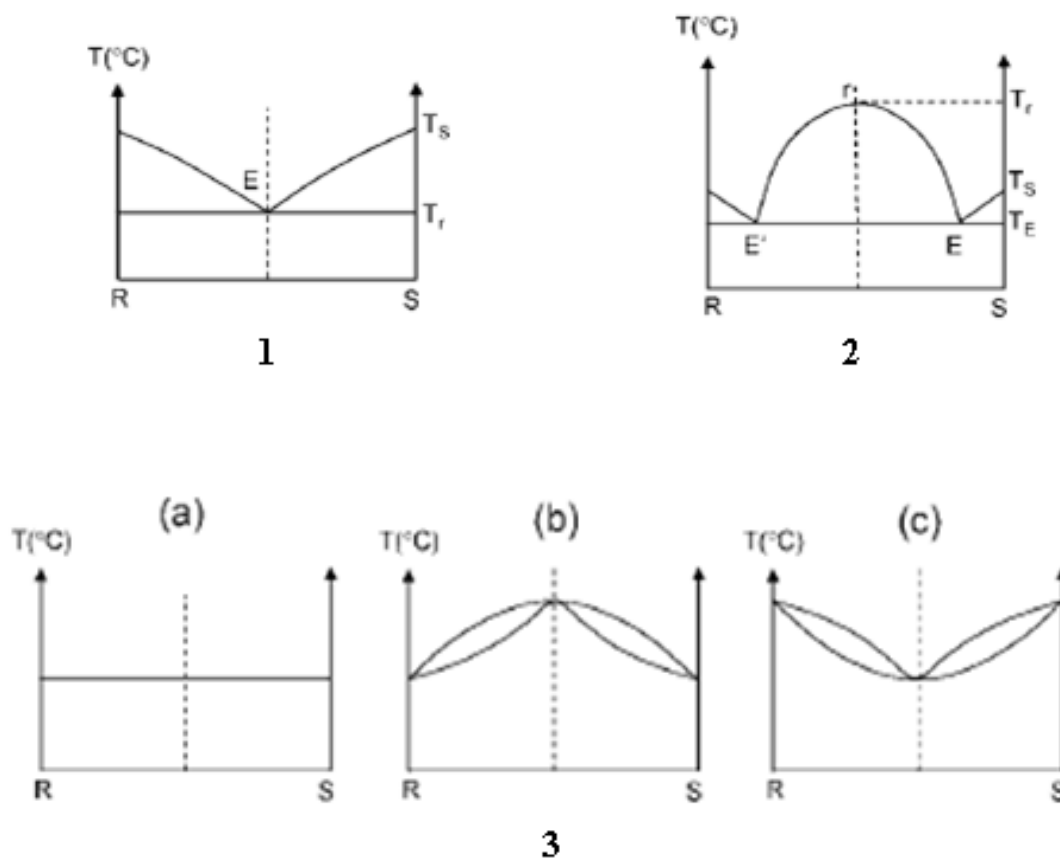


**Figure 1- 2: Typical binary phase diagrams illustrating the three types of racemate (1. Conglomerate, 2. Racemic compound, 3. Pseudoracemate) [9].**

There are essentially three methods that can be applied to obtain single pure enantiomers: extraction, synthesis and separation.

Some of chiral molecules are pure enantiomers in nature, such as carbohydrates, terpene and alkaloids, which can be obtained by extraction method from the plant or animal materials [7]. Pure enantiomers can also be synthesized from the chirality pool by chemical manipulation or asymmetrically synthesized by prochiral substrates. For example, enantiopure pyrroline N-oxides was used as the chiral pool molecules for  $\alpha$ -cyclopropyl- $\beta$ -homoprolines [10] and Mitsunaga *et al.* applied the asymmetric synthesis to produce the cyclic  $\alpha$ -amino acid derivatives by the intramolecular reaction of magnesium carbenoid with an N-magnesium arylamine [11]. The limitation of this method is the availability of a molecule or an enantioselective catalyst suitable for the synthesis of the target enantiomer and the long period for the development of a synthesis recipe. Whereas, the chemistry involved in making a racemate form is much faster and less expensive. Therefore, the best approach would be to synthesize the drug in racemate form and separate the racemate to produce single pure enantiomer.

The process for the separation of the racemate, called enantiochiral resolution, enantioseparation or chiral separation, includes the kinetic, membrane, capillary electrophoresis, chromatography, and crystallization resolution. Kinetic resolution is based on the different reaction rates of two enantiomers with a chiral entity, such as catalysts [12]. The membrane resolution applies the chiral recognized sites on the membrane to achieve the separation of the racemate [13]. The limitations of those two methods are that the lifetime of catalysts and membranes is short and the recovery of catalysts and membranes is energy and time consuming. Capillary electrophoresis can be used to separate ionic species by their charge and frictional forces [14]. Although this method has been proved to be quite efficient, it has the limitation of the concentration

detection and the low productivity [15]. Crystallization is a very powerful technique but is more system-specific. For a given racemate, finding a suitable crystallization process usually involves elaborate experimental investigation. Crystallization resolution includes the diastereomeric crystallization and direct crystallization. For diastereomeric crystallization, diastereomeric salts, which are the products from the reaction of the racemate with an optically active base, have different solubility and then they can be separated by crystallization [16]. The direct crystallization can produce pure enantiomers in the supersaturated partially enriched solution with the desired enantiomer seeds adding [17, 18]. Crystallization resolution can produce the pure enantiomers in industrial scale. However, it needs a large amount of the optically active base and the partially enriched solution which cannot be obtained easily. Chromatography resolution is used to separate the racemate by chiral stationary phase (CSP) with a single or a multi-column process, such as high performance liquid chromatography (HPLC) [19] and simulated moving bed (SMB) chromatography [20, 21]. This method can generate the pure enantiomers efficiently in preparative scale, but a large amount of the chiral stationary phase and mobile phase are required. A simulated moving bed unit is comprised of several fixed-bed chromatographic columns in series and is divided into four sections by valves and inlet/outlet ports, which can be switched periodically in the direction of the fluid flow synchronously or non-synchronously to mimic the continuous countercurrent movement of the solid phase. Compared with the conventional chromatographic techniques, SMB has advantages with its continuous, stable, the less solvent consumption and the productivity per mass of the chiral stationary phase [22].



To overcome the drawbacks of these single separation processes, a “Hybrid” process has been proposed, combining two or more single separation processes to produce pure enantiomers with the minimization of the costs and energy [23, 24].

## **1.2 Research objective and approaches**

The major objective of this thesis is as follows:

*Apply and evaluate the coupling process of SMB and direct crystallization to separate racemic compound (i.e. mandelic acid).*

In this coupling process, SMB chromatography is used to obtain a partially enriched stream and followed by direct crystallization to achieve the complete chiral separation. The lower purity requirement for SMB and solvent recycle can reduce the consumption of the solvent and chiral stationary phase for SMB operation. The scheme of this coupling process for racemic mandelic acid system is shown in Figure 1-3.

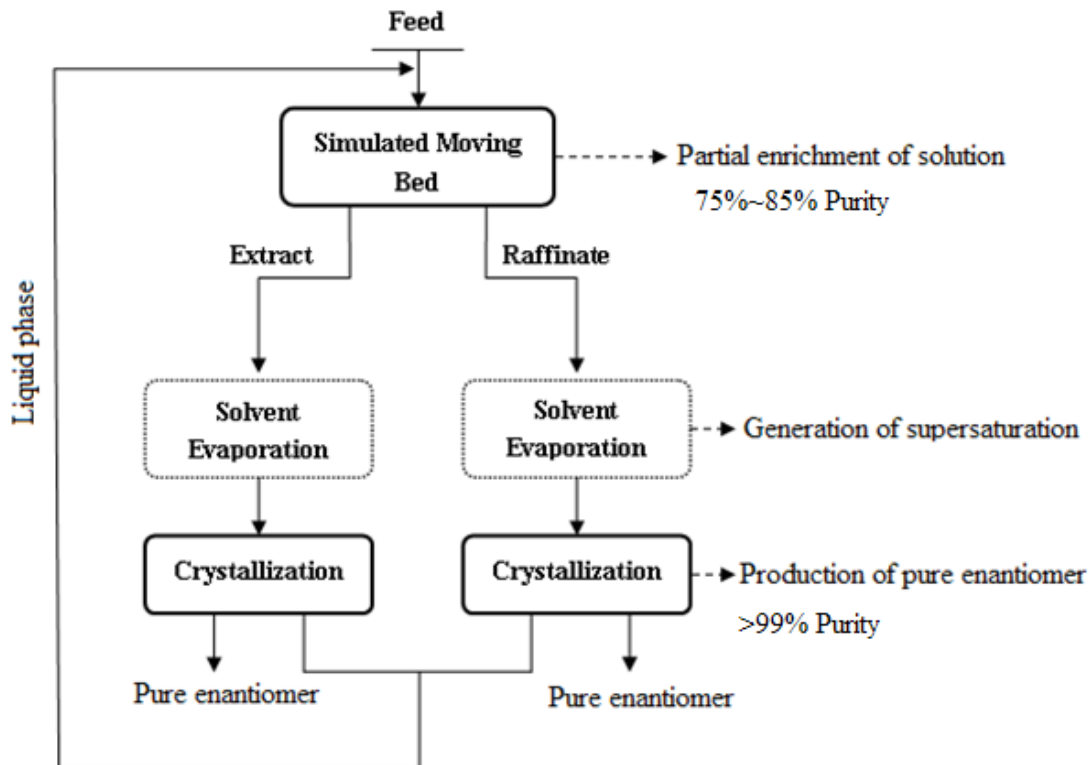


**Figure 1- 3: The scheme of the coupling process of SMB and crystallization process for resolution of mandelic acid.**

It is noticed that only the enantioseparation of the racemic compound (*R,S*)-mandelic acid by SMB and the crystallization process of the enantiomer and racemic compound have been investigated in this thesis. I did some studies about the coupling process. However, the results were not good. So, I didn't include in this thesis. The simulation and optimization for the coupling process will be studied in future.

Specifically, this study aims to achieve the following objectives:

- Chiral separation by SMB technology
  - ✓ Choice of mobile phase

- ✓ Determination of the adsorption isotherm of the racemic compound on the chiral stationary phase
- ✓ Chiral separation of the racemic compound
- Direct crystallization
  - ✓ Development of metastable zone (MSZ) of the crystallization
  - ✓ Estimate the kinetics parameters for the crystallization process
  - ✓ Online-monitor the crystallization process

The following research activities have been carried out in this study to meet the major objectives:

- ❖ The mobile phase has been chosen based on the selectivity and resolution of the racemic compound on the chiral stationary phase using HPLC.
- ❖ The adsorption isotherm of the racemic mandelic acid has been determined by inverse method and frontal analysis method.
- ❖ Separation of the racemic mandelic acid was accomplished using a semi-preparative SMB unit.
- ❖ The metastable zone limit of mandelic acid in water was measured by ATR-FTIR and FBRM.
- ❖ The crystallization kinetic parameters of (*R,S*)-mandelic acid and (*R*)-mandelic acid from aqueous solution have been determined by fitting the experimental data with calculated crystallization process model.
- ❖ Online monitoring of the crystallization process of mandelic acid has been carried out using ATR-FTIR and FBRM.

### 1.3 Thesis organization

This thesis is organized based on the article-integrated format and is composed of 6 main chapters.

Chapter 1 gives a general overview of this thesis and followed by a comprehensive review for the background of simulated moving bed technology and the crystallization process in Chapter 2.

In Chapter 3, the resolution of racemic mandelic acid ((*R,S*)-MA) and numerical determination of binary competitive isotherm of (*R,S*)-MA on the Chiralcel OD column have been investigated in this study. The effects of the alcohol modifier and acidic additive in the mobile phase on the retention and enantioseparation of (*R,S*)-MA were studied at first. The inverse method was then used to determine the competitive isotherm parameters of (*R,S*)-MA by minimizing the sum of square deviations between the model predictions and the measured elution profiles. And the adsorption isotherm was verified by frontal analysis method.

Chapter 4 depicts the chiral separation of the racemic mandelic acid ((*R,S*)-MA) by simulated moving bed chromatography with Chiralcel OD columns experimentally and numerically. The transport dispersion model combined with the modified Langmuir isotherm was applied to predict the dynamic behaviour and separation performance of the SMB process. The triangle theory was used to obtain the complete separation region of the SMB operation. The influences of the switching time, loading, extract flow rate and column configuration on the SMB performance were also studied. Good agreement

between the experimental data and model predictions proved the efficiency and reliability of SMB modeling and triangle theory in the design as well as the operation of SMB chromatography.

Chapter 5 presents the determination of the nucleation and growth kinetics of (*R,S*)-mandelic acid ((*R,S*)-MA) and (*R*)-mandelic acid ((*R*)-MA) in aqueous solutions using an unseeded cooling crystallization process. To obtain the nucleation and growth kinetics, the solubility, metastable zone limits and supersaturation were measured by in-situ attenuated total reflection Fourier transform infrared (ATR-FTIR) spectroscopy and focused beam reflectance measurement (FBRM). The nucleation rate and growth rate parameters were determined by a nonlinear optimization algorithm. The effects of initial concentration and cooling rate on supersaturation and the nucleation rate were also discussed.

In Chapter 6, the overall conclusion is made according to the results shown in the previous chapters. It is also summarized that the limitations and recommendations of this thesis. In addition, the future works are listed in final.

## **1.4 Contribution**

The major contributions of this study are threefold. First of all, the adsorption isotherm of the racemic mandelic acid on the preparative column by inverse method is studied at the first time. The transport dispersive column model is combined with competitive modified Langmuir isotherm model to simulate the chiral separation process on the HPLC. Those parameters of the adsorption isotherm are vital for the design of the SMB. Secondly, it is

also the first time to report the separation of the racemic mandelic acid on SMB unit in preparative scale as well as the effects of operating conditions for mandelic acid systems on SMB with Chiralcel OD columns. Those optimal operating conditions on the SMB are significant to get the partially enriched solution for the crystallization. Moreover, the solubility and metastable zone limit of mandelic acid in water as well as nucleation and growth kinetics of mandelic acid have been studied systematically, which is essential to get the pure enantiomers by direct crystallization.

## 1.5 Reference

1. Maier, N.M., P. Franco, and W. Lindner, *Separation of enantiomers: needs, challenges, perspectives*. Journal Of Chromatography A, 2001. **906**(1): p. 3-33.
2. Food and Drug Administration, *FDA'S policy statement for the development of new stereoisomeric drugs*. Chirality, 1992. **4**(5): p. 338-340.
3. Thayer, A.M., *Chiral Chemistry*. Chemical & Engineering News, 2008. **86**(31): p. 12-20.
4. Caner, H., et al., *Trends in the development of chiral drugs*. Drug discovery today, 2004. **9**(3): p. 105-110.
5. Rouhi, A.M., *Chiral Chemistry: Traditional methods thrive despite numerous hurdles, including tough luck, slow commercialization of catalytic processes*. Chemical & Engineering News, 2004. **82**(24): p. 47-62.
6. Roozeboom, H.W.B., *Löslichkeit und Schmelzpunkt als Kriterien für racemische Verbindungen, pseudoracemische Mischkristalle und inaktive Konglomerate*. Z. Phys. Chem, 1899. **28**: p. 494.
7. Sheldon, R.A., *Chirotechnology :industrial synthesis of optically active compounds*. 1993, New York: Marcel Dekker. 423.
8. Jacques, J., A. Collet, and S.H. Wilen, *Enantiomers, racemates, and resolutions*. 1981, New York ;; Toronto: Wiley. 447.
9. Wang, Y. and A.M. Chen, *Enantioenrichment by Crystallization*. Organic Process Research & Development, 2008. **12**(2): p. 282-290.
10. Cordero, F.M., et al., *Synthesis of  $\alpha$ -Cyclopropyl- $\beta$ -homoprolines*. The Journal of organic chemistry, 2009. **74**(11): p. 4225-4231.

11. Mitsunaga, S., et al., *Asymmetric synthesis of cyclic  $\alpha$ -amino acid derivatives by the intramolecular reaction of magnesium carbenoid with an N-magnesium arylamine*. *Tetrahedron: Asymmetry*, 2009. **20**(14): p. 1697-1708.
12. Zhang, J.-Y., et al., *Application of kinetic resolution using HCS as chiral auxiliary: Novel synthesis of  $\beta$ -blockers (S)-betaxolol and (S)-metoprolol*. *Chirality*, 2009. **21**(8): p. 745-750.
13. Xiong, W.-W., et al., *Chiral separation of (R,S)-2-phenyl-1-propanol through glutaraldehyde-crosslinked chitosan membranes*. *Journal of Membrane Science*, 2009. **328**(1-2): p. 268-272.
14. Kuhn, R. and S. Hoffstetter-Kuhn, *Chiral separation by capillary electrophoresis*. *Chromatographia*, 1992. **34**(9): p. 505-512.
15. Wang, X., et al., *Chiral separation of propranolol hydrochloride through an SMB process integrated with crystallization*. *Journal of Industrial and Engineering Chemistry*, 2006. **12**(6): p. 868-876.
16. Kozma, D., *CRC handbook of optical resolutions via diastereomeric salt formation*. 2002: CRC.
17. Lorenz, H., D. Polenske, and A. Seidel-Morgenstern, *Application of preferential crystallization to resolve racemic compounds in a hybrid process*. *Chirality*, 2006. **18**(10): p. 828-840.
18. Zhang, Y., et al., *Nucleation and Growth Kinetics of (R)-Mandelic Acid from Aqueous Solution in the Presence of the Opposite Enantiomer*. *Crystal Growth & Design*, 2010. **10**(7): p. 2879-2887.
19. Yu, L., et al., *Simultaneous determination of diastereoisomeric and enantiomeric impurities in (1R,3R)-1-(1,3-benzodioxol-5-yl)-2-(chloroacetyl)-2,3,4,9-tetrahydro-1H-pyrido [3,4-b] indole-3-carboxylic acid methyl ester a key intermediate of tadalafil by chiral high performance liquid chromatography*. *Chirality*, 2012. **24**(4): p. 303-306.



20. Zhang, Y., K. Hidajat, and A.K. Ray, *Enantio-separation of racemic pindolol on Formula Not Shown -acid glycoprotein chiral stationary phase by SMB and Varicol*. Chemical Engineering Science, 2007. **62**(5): p. 1364-1375.
21. Rajendran, A., G. Paredes, and M. Mazzotti, *Simulated moving bed chromatography for the separation of enantiomers*. Journal of Chromatography A, 2009. **1216**(4): p. 709-738.
22. Francotte, E.R. and P. Richert, *Applications of simulated moving-bed chromatography to the separation of the enantiomers of chiral drugs*. Journal of Chromatography A, 1997. **769**(1): p. 101-107.
23. Lim, B.-G., et al., *Recovery of (-)-praziquantel from racemic mixtures by continuous chromatography and crystallisation*. Chemical Engineering Science, 1995. **50**(14): p. 2289-2298.
24. Svang-Ariyaskul, A., W.J. Koros, and R.W. Rousseau, *Chiral separation using a novel combination of cooling crystallization and a membrane barrier: Resolution of DL-glutamic acid*. Chemical Engineering Science, 2009. **64**(9): p. 1980-1984.

## **Chapter 2**

### **Literature Review**

## **2.1 Simulated moving bed (SMB)**

### **2.1.1 Background of SMB**

The increasing awareness of the importance of chirality in terms of therapeutic effects has stimulated a stricter regulation and a growing market demand for the pure enantiomers. The ever-increasing demand for the pure enantiomers makes the development of the efficient approaches for the separation of the racemic mixture. Chromatographic separation has become one of the most efficient methods for the chiral separation. Compared to the traditional batch chromatography, the continuous counter current chromatography has its advantages with the maximization of the mass transfer driving force, the reduction of the solvent consumption and the increase of the purity and productivity[1]. However, the movement of the solid phase leads to the problems of attrition and mixing. To overcome those drawbacks of the true moving bed (TMB), the concept of the simulated moving bed (SMB), a continuous countercurrent multi-column chromatographic separation technique as the practical implement of the true moving bed (TMB) process, was invented by Broughton and Gerhold [2] in 1961.

SMB process was first applied in 1960s by the UOP Inc. to separate the p-xylene from the mixture on zeolites. In the early stage of the development, commercial large-scale SMB units were widely implemented not only in the petro-chemical industry but also in the sugar industry, such as separation of glucose and fructose on ion exchange resins.

The development of the HPLC techniques and the stationary phases made the shorter columns operated under the high pressure with smaller stationary phase particles

available for the chromatographic separation process in 1970s. In addition, SMB unit was downscaled based on the HPLC separation technology in the earlier 1990s. Due to the increasing demand for the pure enantiomers by the regulation of FDA, SMB has been increasingly adopted in fine chemistry, biological technology and pharmaceutical science, especially for chiral separation [3-6]. The first chiral resolution by SMB was performed on phenyl-ethyl alcohol by Negawa and Shoji in 1992 [4]. Daicel chemicals and UCB pharma have applied SMB unit to produce the pure enantiomers since 1998 with the production of several tons per year [7]. With the pioneering works and the development of the chiral stationary phase, SMB is more popular as the method of chiral resolution in the pharmaceutical area [8-11].

### **2.1.2 Chromatography**

Chromatography is a separation process based on the different partition between a flowing fluid (mobile phase) and a solid adsorbent (stationary phase). This technology was first applied by Mikhail Tswett (1872-1919) for the separation of the plant pigments with the calcium carbonate in 1906.

The principle of the elution chromatography can be illustrated in Figure 2-1, where the blue triangle with the letter 'A' and the yellow triangle with the letter 'B' are considered as the more and less retained substances, respectively. Although starting together, the triangle 'B' will be completely separated from the triangle 'A' and washes out with the fluid flow first and then the triangle 'A' flows out later, since the triangle 'B' has less interaction with the steady conveyor belt than triangle 'A'.

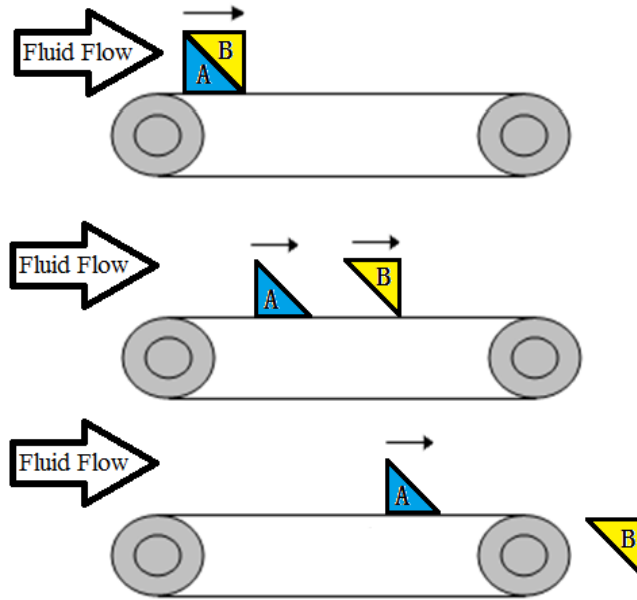


**Figure 2- 1: Analogy for elution chromatography.**

### **2.1.3 Continuous counter-current chromatography**

The counter-current chromatography is that the mobile phase and solid phase move in the opposite direction, which can be illustrated in Figure 2-2. The triangle 'A' and 'B' are pushed by the fluid flow on the conveyer belt moving in the opposite direction. The triangle 'A' is more affinity to the conveyer belt than triangle 'B' which is easier to leave the conveyer belt with the flowing fluid. So the triangle 'A' moves slower than 'B'. Then there are three cases in terms of the velocity of the conveyer belt. If the velocity of the conveyer belt is larger than that of 'B' or less than that of 'A', the net velocity with one direction will push both of the triangles to the right end or to the left end of the belt. Another case is that the velocity of the conveyer belt is intermediate to that of two triangles which leads to two opposite directions of the net velocities, one for 'A' to the left and the other for 'B' to the right. Then the 'A' and 'B' can be separated and collected in two ends of the belt,

respectively. The key of the process design is to determine the intermediate velocity which will be discussed in the following section. In the counter-current flow, the maximization of the separation driving force between the solid and liquid phase makes the separation more efficient.

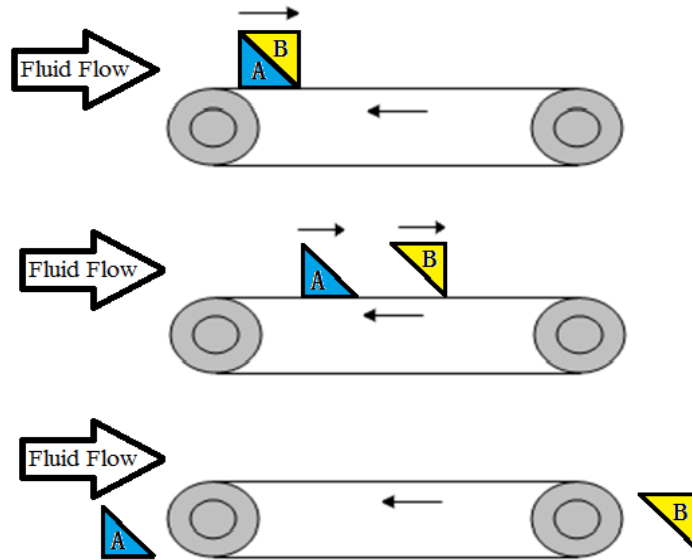


**Figure 2- 2: Analogy for countercurrent elution chromatography.**

Here, ‘continuous’ means the continuous injection of the feed stream. The continuous chromatography has its advantages with the minimum capital operating costs and maximum throughput.

### **2.1.3.1 True moving bed (TMB)**

It is called true moving bed because the solid phase is moving naturally. A typical configuration of the true moving bed is illustrated in Figure 2-3 for the binary separation of species A and B. Here, A and B are assumed as the more and less retained component, respectively. The column is divided into four sections by the inlet (feed and desorbent)

and outlet (raffinate and extract) ports. The solid phase is introduced at the top of the column and moves downward with gravity. Meanwhile, the mobile phase comes from the bottom and moves upward. The sample with species A and B is fed continuously in the middle of the column between section II and III and diluted by the desorbent flow D. The strongly adsorbed A is absorbed by the sinking solid phase in section II and III. And then that solid phase with A is washed by the rising mobile phase in section I. So A can be collected in the extract port. As a less adsorptive product, B is gradually desorbed by the rising mobile phase from the solid phase in section II and III and can be collected in the raffinate port. The solid phase can be regenerated in section I by desorbing A with the rising mobile phase. And the desorbent (mobile phase) can also be cleaned by removing B with the sinking solid phase in section IV.

The earliest large-scale moving bed process is known as the hypersorption process [12, 13]. Although the true moving bed system can be used to carry out a lot of work [14], the practical problems in design and operation are insuperable. The physical movement of the solid phase leads a number of problems such as the particle attrition, expansion of the bed and so on.

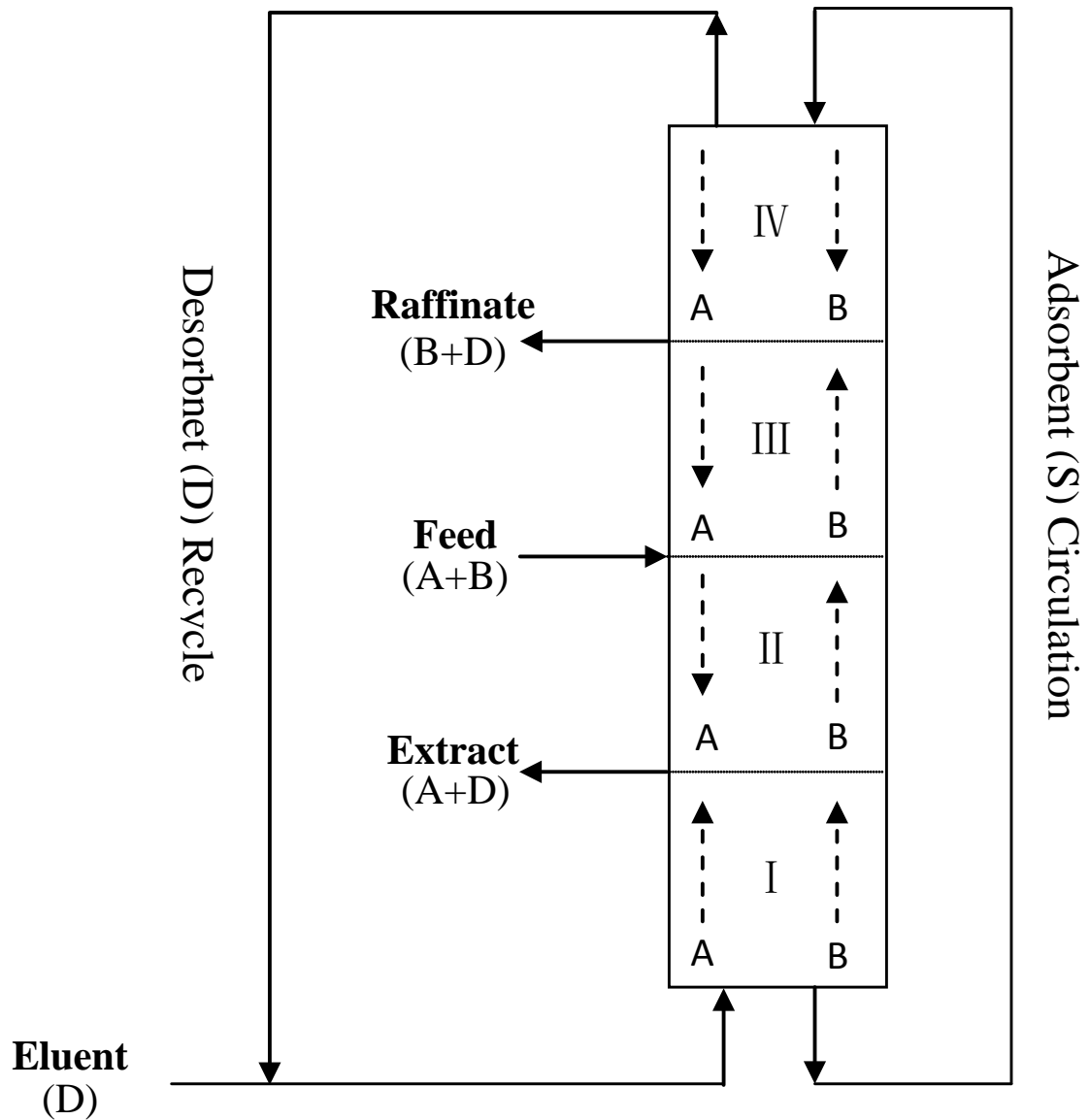


**Figure 2- 3: Typical configuration of the true moving bed.**

### 2.1.3.2 Simulated moving bed (SMB)

The simulated moving bed process overcomes the problems caused by the movement of solid phase in true moving bed process. A simulated moving bed unit is comprised of several fixed-bed chromatographic columns in series and is divided into four sections by valves and inlet/outlet ports, which can be switched periodically in the direction of the



fluid flow synchronously or non-synchronously to mimic the continuous countercurrent movement of the solid phase [15]. A typical configuration of the SMB is shown in Figure 2-4.

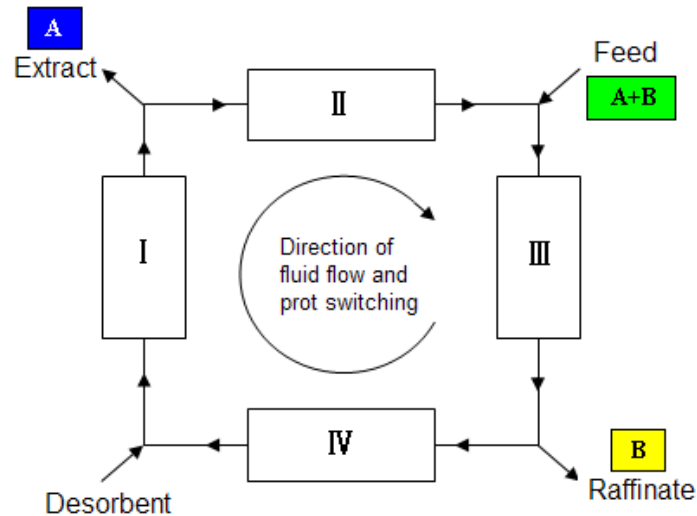


**Figure 2- 4: Typical configuration of the simulated moving bed.**

Compared with the TMB, SMB system uses the fixed solid phase in the series columns instead of the moving solid phase to reduce the particle attrition and bed expansion effectively and make the system cleaner and more environmentally attractive. Meanwhile, the countercurrent movement of the solid phase is accomplished by shifting all the ports over one column simultaneously in the same direction as fluid flow instead of moving by gravity, which is much easier to control the movement of solid. When the length of SMB columns becomes infinitesimal and the number of the columns becomes infinite, the SMB can be assumed as TMB. The relationship between TMB and SMB is illustrated in Table 2-1[16].

**Table 2- 1: Relationship between a TMB and SMB**

TMB	SMB
Solid phase	Fixed SMB columns
Steady state	Periodic steady state
Solid flow rate	Shift all ports periodically
$Q_s$	$t^* = V(1 - \varepsilon)/Q_s$ (2-1)
Internal flow rate	Internal flow rate
$Q_k^{TMB}, k = I, II, III, IV$	$Q_k^{SMB} = Q_k^{TMB} + \left(\frac{\varepsilon}{1-\varepsilon}\right) Q_s$ (2-2)

Nowadays, the simulated moving bed process has replaced true moving bed as a popular technique of the continuous counter-current chromatography in the industry.

#### 2.1.4 Column model for SMB

In this section, the column model for the SMB process is presented. The assumptions of the model are listed as follows [17].

- 1) The column is radial homogeneous for the column, i.e. homogeneity and stability of column packing.
- 2) The axial dispersion coefficient is constant.
- 3) The fluid flow is constant and the void fraction is the same in the column.
- 4) The compressibility of the mobile phase is neglected.

- 5) Both of the phases have the same partial molar volumes of the sample components.
- 6) In the isotherm definition, the solvent or the weak solvent is not adsorbed by the stationary phase.
- 7) There are no thermal effects and the heat effects on the adsorption. i.e. the migration of a band is not effected by temperature.
- 8) Operating condition is constant, i.e. constant temperature, pressure, mobile phase, flow rate.

#### 2.1.4.1 Ideal model

The assumption of the ideal model is that the equilibrium between solid and liquid phases is instantaneous and the column efficiency is infinite. But the axial dispersion and the mass transfer resistance are neglected. The column mass balance under the ideal model is written as

$$\frac{\partial c_{ik}}{\partial t} + \frac{1-\varepsilon}{\varepsilon} \cdot \frac{\partial q_{ik}}{\partial t} + u \cdot \frac{\partial c_{ik}}{\partial z} = 0, (i = A, B) \quad (2-3)$$

where  $c_{ik}$  and  $q_{ik}$  are the concentrations of the solute in the liquid and solid phases of the enantiomer  $i$  in the section  $k$ , respectively.  $z$  is space coordinate and  $t$  is time.  $\varepsilon$  is the void fraction of the column.  $u$  is interstitial fluid velocity. Several cases [18-20] with ideal model showed an excellent agreement between the concentration profiles calculated from the model and from the experiment data.

#### 2.1.4.2 Equilibrium dispersive (ED) model

The equilibrium dispersive model assumes instantaneous and constant equilibrium between the both phases, and takes account for the axial dispersion and the mass transfer resistance. However, the mass transfers are fast. A lumped apparent dispersion coefficient,  $D_a$ , is used to generalize both effects. That dispersion coefficient is assumed as constant in all the columns of the SMB process for the sake of the simplicity. The column mass balance under the equilibrium dispersive is written as

$$\frac{\partial c_{ik}}{\partial t} + \frac{1-\varepsilon}{\varepsilon} \cdot \frac{\partial q_{ik}}{\partial t} + u \cdot \frac{\partial c_{ik}}{\partial z} = D_a \cdot \frac{\partial^2 c_{ik}}{\partial z^2}, (i = A, B) \quad (2-4)$$

The apparent dispersion coefficient can be derived from the column efficiency which is expressed by the number of theoretical plates,  $N_p$ .

$$D_a = \frac{uL_c}{2N_p} \quad (2-5)$$

where  $u$  is interstitial fluid velocity and  $L_c$  is column length. This numerical solution of the model was successfully applied in many cases [11, 17, 21].

#### 2.1.4.3 Transport dispersive (TD) model

The transport dispersive (TD) model is frequently applied to describe the mass transfer in the solid phase and the mass balance between solid phase and liquid phase along the column in liquid chromatography. In this model, the kinetics of adsorption–desorption is infinitely fast but not for the mass transfer kinetics [22-24]. The mass transfer kinetics of the solute to the surface of the adsorbent is given by the linear driving force model. Here,

the solid film linear driving force is used in the model. The differential mass balance and the lumped kinetic models are shown in the following equations.

$$\frac{\partial c_{ik}}{\partial t} + \frac{1-\varepsilon}{\varepsilon} \cdot \frac{\partial q_{ik}}{\partial t} + u \cdot \frac{\partial c_{ik}}{\partial z} = D_L \cdot \frac{\partial^2 c_{ik}}{\partial z^2}, (i = A, B) \quad (2-6)$$

$$\frac{\partial q_{ik}}{\partial t} = k_m(q_{ik}^* - q_{ik}) \quad (2-7)$$

where  $D_L$  is the dispersion coefficient.  $k_m$  is the lumped rate coefficient.  $q_{ik}^*$  is the adsorbed amount of each enantiomers in the stationary phase equilibrated with the mobile phase at the concentration  $c_{ik}$ . That can be evaluated by the competitive adsorption isotherm for the binary separation.

The initial and boundary conditions for this problem are

$$c_{ik}(z, t = 0) = 0, q_{ik}(z, t = 0) = 0 \quad (2-8)$$

$$c_{ik}(z = 0, t) = c_{ik}^{in}, q_{ik}(z = 0, t) = f_i(c_{A,k}^{in}, c_{B,k}^{in}) \quad (2-9)$$

where  $f$  is the function of the adsorption isotherm.

## 2.1.5 Competitive adsorption isotherm models

The competitive adsorption isotherm is the equilibrium isotherm which describes the distribution of dilute sample solutes with two components between the stationary and the mobile phase. Those adsorption behaviours are described by several models [17] which are used to determine the possible adsorption isotherm on the column. In this section, three models are introduced.

### 2.1.5.1 Competitive Langmuir isotherm

The competitive Langmuir isotherm model assumes that the monolayer of the adsorbate molecules can be held by a homogeneous adsorbent surface [17]. At equilibrium, the rate of adsorption and desorption is equal for each component. The model is given as

$$q_i^* = \frac{q_s b_i c_i}{1 + b_A c_A + b_B c_B} \quad (2-10)$$

where  $q_s$  is the monolayer capacity for the stationary phase,  $b_i$  is the ratio of the rate constants of adsorption and desorption. This model is widely used to study the adsorption behaviour on the chiral stationary phase. Enmark *et al.* [25] applied this model to determine the adsorption behaviour of racemic methyl mandelate on a tris-(3,5-dimethylphenyl) carbamoyl cellulose chiral stationary phase. Asnin *et al.* [26] used it to study the adsorption of Naproxen enantiomers on the chiral stationary phase Whelk-O1. That model can also be used in SMB. For example, Mihlbachler *et al.* [27, 28] studied the effect of the homogeneity of the column set on the SMB performance based on the competitive Langmuir isotherm model.

### 2.1.5.2 Competitive biLangmuir isotherm

This model assumes two different types of binding sites with either one being homogeneous on the surface of the stationary phase. Competitive bi-Langmuir isotherm model is written as:

$$q_i^* = \frac{q_{1s} b_{1,i} c_i}{1 + b_{1,A} c_A + b_{1,B} c_B} + \frac{q_{2s} b_{2,i} c_i}{1 + b_{2,A} c_A + b_{2,B} c_B}, (i = A, B) \quad (2-11)$$

where  $q_{1s}$  and  $q_{2s}$  are the saturation capacities of the two sites;  $b_{1,i}$  and  $b_{2,i}$  are the equilibrium constants of the two sites for two enantiomers  $i$ . The competitive biLangmuir adsorption isotherm is widely applied to describe the competitive retention mechanism of chiral molecules on various chiral stationary phases. This model was applied in the numerical determination of the competitive isotherm of the racemic mixture of the 1-phenyl-1-propanol enantiomers [29] and in the development of a new approach about the inverse method on plateaus for isotherm determination[30]. And it was also used to study the isotherm behaviour of the mandelic acid enantiomers mixture on cellulose-based chiral stationary phase [24].

### 2.1.5.3 Competitive Tóth isotherm

The competitive Tóth model [31] can also be applied to describe adsorption isotherm. This model assumes that the sites on the sorbent are heterogeneous and there exists the maximum adsorption energy which is larger than the sorption energy generated by the most sites.

$$q_i^* = \frac{q_s b_i c_i}{[1+(b_A c_A + b_B c_B)^v]^{\frac{1}{v}}} \quad (0 < v < 1), (i = A, B) \quad (2-12)$$

where  $q_s$  is the monolayer capacity of the chiral stationary phase,  $b_i$  is the equilibrium constants of the adsorption and  $v$  is an exponent constant. Felinger *et al.* [32] applied this model to determine the adsorption isotherm of the 1-indanol enantiomers. This model was also applied by Zhang *et al.* [24] to analyze the isotherm behaviour of the mandelic acid enantiomers.

### 2.1.6 Node model

For a classic SMB process, the node models describing the mass balances of flow rates at each node are given as [16]

Desorbent inlet node (Eluent)

$$Q_D = Q_1 - Q_4 \quad (2-13)$$

$$c_{i,D} = \frac{Q_1 c_{i,1}^{in} - Q_4 c_{i,4}^{out}}{Q_D} \quad (2-14)$$

Extract withdrawal node

$$Q_E = Q_1 - Q_2 \quad (2-15)$$

$$c_{i,E} = c_{i,1}^{out} = c_{i,2}^{in} \quad (2-16)$$

Feed inlet node

$$Q_F = Q_3 - Q_2 \quad (2-17)$$

$$c_{i,F} = \frac{Q_3 c_{i,3}^{in} - Q_2 c_{i,2}^{out}}{Q_F} \quad (2-18)$$

Raffinate withdrawal node

$$Q_R = Q_3 - Q_4 \quad (2-19)$$

$$c_{i,R} = c_{i,3}^{out} = c_{i,4}^{in} \quad (2-20)$$



where  $Q_D$  is the desorbent flow rate,  $Q_E$  is the extract flow rate,  $Q_F$  is the feed flow rate and  $Q_R$  is the raffinate flow rate. The superscripts “in” and “out” refer to the inlet and outlet streams, respectively.

### 2.1.7 Design strategy for SMB

The operation of a given SMB process to isolate the racemates is dictated by several parameters, namely the flow rates in the four sections and the switch time, based on the target performance [33]. Morbidelli groups [34, 35] exploited a triangle theory to ascertain these parameters for the design of SMB process. They introduced the net flow rate ratio,  $m_k$ , based on the assumption that all kinetics is neglected and the SMB is similar to TMB which means that the internal mobile phase velocity of SMB is the same as that of TMB columns, and the solid phase velocity in the TMB units is equal to the simulated solid velocity in the SMB. The TMB and SMB process have been proven to be equivalent if the conversion rules in Table 2-1 are fulfilled.

Then, the net flow rate ratio can be written as

$$m_k = \frac{Q_k t^* - V\varepsilon - V_k^D}{V(1-\varepsilon)} \quad (k = I, \dots, IV) \quad (2-21)$$

where  $Q_k^{SMB}$  and  $Q_k^{TMB}$  are the flow rates of the fluid phase in section  $k$  of a SMB unit and in the equivalent TMB unit, respectively.  $Q_s$  is the solid phase flow rate in TMB unit.  $V$  is the column volume and  $t^*$  is the switching time. A triangle shape region, formed in the  $(m_2, m_3)$  plane for linear and nonlinear isotherms, with or without mass transfer resistant, is identified as the complete separation region.

### 2.1.7.1 Linear isotherm

Triangle theory with linear adsorption isotherm was applied to the SMB design firstly.

The linear isotherm is described as

$$q_i = H_i c_i \quad (2-22)$$

$$H_i = \frac{t_{i,k}^R - t_{0,k}}{t_{0,k}} \frac{\varepsilon}{(1-\varepsilon)} \quad (2-23)$$

$$t_{0,k} = \frac{V\varepsilon}{Q_k} \quad (2-24)$$

where  $H_i$  is the Henry constant of the component  $i$ .  $t_{ik}^R$  and  $t_{0k}$  are the retention time and the dead time of component  $i$  in section  $k$ , respectively.

Considering the specific function of each section in SMB, the criteria of the complete separation of the binary mixture in linear case can be determined. The complete separation requires the switch time in the section II and III should be larger than the retention time of component B and smaller than that of component A. It ensures the component B goes out in the raffinate port without the pollution of component A. That also assures the component B completely removes from the stationary phase and does not contaminate the extract port after next switch whereas component A remains in the stationary phase and is eluted by the desorbent flow to the extract port. Section I is used for the solid phase regeneration which means component A should be completely wash out stationary phase. So, the switch time should be larger than the retention time of component A. To ensure the desorbent regeneration in section IV, i.e. no component in the

mobile phase, the switch time in this section should be smaller than the retention time of component B. Those conditions can be expressed as following constraints [1]:

$$t_{A,1}^R \leq t^* \quad (2-24a)$$

$$t_{B,2}^R \leq t^* \leq t_{A,2}^R \quad (2-24b)$$

$$t_{B,3}^R \leq t^* \leq t_{A,3}^R \quad (2-24c)$$

$$t^* \leq t_{B,4}^R \quad (2-24d)$$

Those constraints can be converted into the inequalities of the net flow rate ratio [35] based on Eqs.(2-1), (2-2),(2- 21), (2- 23) and (2-24)

$$H_A < m_1 < \infty \quad (2-25a)$$

$$H_B < m_2 < H_A \quad (2-25b)$$

$$H_B < m_3 < H_A \quad (2-25c)$$

$$\frac{-\varepsilon_p}{1-\varepsilon_p} < H_B < m_4 \quad (2-25d)$$

To get the positive feed flow rate, the condition should enforce to  $m_2 < m_3$ . So combining with Eqs. (2-25b , c), the constraints are shown as

$$H_B < m_2 < m_3 < H_A \quad (2-25e)$$

The projection of the triangle region of the complete separation zone defined by the inequality (Eq. (2-25e)) on the  $(m_2, m_3)$  and  $(m_1, m_4)$  planes is shown in Figure 2-5.

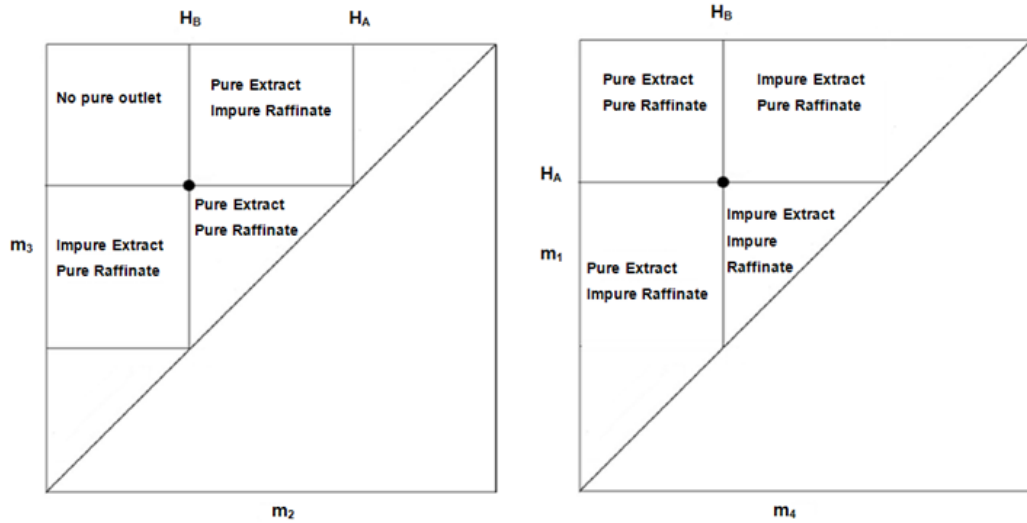


**Figure 2- 5: Triangle theory: the different separation regimes on the  $(m_2, m_3)$  plane for the binary separation with linear adsorption isotherm.**

The triangle region in the  $(m_2, m_3)$  plane indicates that 100% pure enantiomers can be collected both in the extract and raffinate ports. The upper-right square is the region in which the operating conditions lead to only the pure extract, but not the pure raffinate. The opposite results are shown in the lower-left square when  $m_2 < H_B$ . Neither pure extract nor pure raffinate can be found under the operating conditions located in the upper-left square where  $m_2 < H_B$  and  $m_3 > H_A$ .

### 2.1.7.2 Nonlinear Isotherm

The triangle theory is extended to the adsorption behaviour which is described by nonlinear adsorption isotherm. The competitive Langmuir isotherm was given as an example as follows.

The design conditions on the net flow rate ratio  $m_k$  to complete separation is derived from the equilibrium model equation with the adsorption isotherm, Eqs. (2-4) and (2-10), and the following constrains [34, 36, 37]:

$$H_A = m_{1,min} < m_1 < \infty \quad (2-26a)$$

$$m_{2,min}(m_2, m_3) < m_2 < m_3 < m_{3,max}(m_2, m_3) \quad (2-26b)$$

$$\frac{-\varepsilon_p}{1-\varepsilon_p} < H_B < m_{4,max}(m_2, m_3) = \frac{1}{2} \left\{ H_B + m_3 + b_B c_{B,F}(m_3 - m_2) - \sqrt{[H_B + m_3 + b_B c_{B,F}(m_3 - m_2)]^2 - 4H_B m_3} \right\} \quad (2-26c)$$

Compared with boundary for  $m_2$  and  $m_3$ , the lower bound on  $m_1$  and upper bound on  $m_4$  are found to be explicit. However, the region for the complete separation in the  $(m_2, m_3)$  plane is still a triangle-shaped illustrated in Figure 2-6.

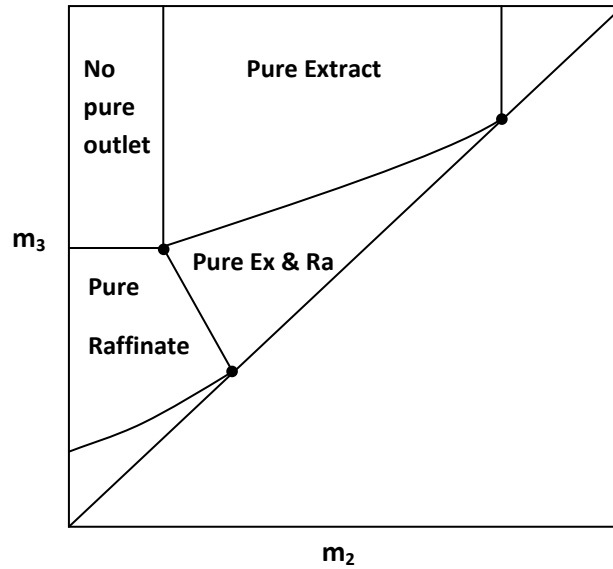


**Figure 2- 6: Triangle theory: the different separation regimes on the  $(m_2, m_3)$  plane for the binary separation with Langmuir adsorption isotherm.**

Triangle theory is now widely used for SMB process design. Those procedures employed for binary separation is further applied to the design of multi-component systems subject to a number of different nonlinear isotherm, namely the modified Langmuir isotherm [27, 38], biLangmuir [11, 39] and the generalized Langmuir isotherm [40, 41].

### **2.1.8 Performance parameters**

The performance parameters are used to evaluate the performance of the separation process and optimize SMB operation. In this section, several parameters are introduced.

### 2.1.8.1 Purity

The purity,  $Pu$ , is defined as the ratio of the component B concentration to the solute concentration of the raffinate stream or the ratio of the component A concentration to the solute concentration of the extract stream.

$$Pu_R = \int_t^{t+t^*} \frac{c_{B,R}}{c_{A,R}+c_{B,R}} dt \quad (2-27a)$$

$$Pu_E = \int_t^{t+t^*} \frac{c_{A,E}}{c_{A,E}+c_{B,E}} d \quad (2-27b)$$

where  $Pu_R$  and  $Pu_E$  are the purities of the raffinate and extract eluent, respectively. And  $c_{i,R}$  and  $c_{i,E}$  are the concentrations of the solute in the raffinate and extract stream of the component  $i$ , respectively.

### 2.1.8.2 Recovery

The recovery,  $Re$ , is determined by the ratio of the mass flow rate of component B in the raffinate stream or that of the component A in the extract stream to that in the feed flow.

$$Re_A = \frac{Q_E}{Q_F} \int_t^{t+t^*} \frac{c_{A,E}}{c_{B,F}} \quad (2-28a)$$

$$Re_B = \frac{Q_R}{Q_f} \int_t^{t+t^*} \frac{c_{B,R}}{c_{B,F}} dt \quad (2-28b)$$

where  $c_{i,R}$  and  $c_{i,E}$  are the concentrations of the solute in the raffinate and extract eluent of the component  $i$ , respectively.

### 2.1.8.3 Productivity

The productivity,  $Pr$ , is measured by the ratio of the mass of feed to that of the chiral stationary phase.

$$Pr = \frac{Q_F c_{T,F}}{(1-\varepsilon)\rho_s V_T} \quad (2-29)$$

where  $c_{T,F}$  is the overall concentration of feed mixture. And  $\rho_s$  is the density of the solid phase.

### 2.1.8.4 Desorbent requirement

The desorbent requirement,  $Dr$ , is defined as the ratio of the mass of desorbent to that of feed.

$$DR = \frac{(Q_D + Q_E)\rho_D}{Q_F c_{T,F}} \quad (2-30)$$

where  $\rho_D$  is the desorbent density.

## 2.2 Direct crystallization

### 2.2.1 Background of crystallization

Crystallization from the solution is known as one of the oldest unit operations in the chemical engineering discipline. As the solid-liquid separation and purification process, it is widely applied in the pharmaceutical, food, bulk chemicals and agriculture industries with a significant impact on the overall process efficiency and cost. In addition, this process can control the properties of the final product, such as size, shape and the mass of



crystals produced, especially for the pharmaceutical industry [42]. Crystallization can be performed by cooling [43], evaporation [44], addition of antisolvent [45], reaction [46] or isoelectric precipitation [47] and can be classified into batch [48-51] and continuous [52-54] process. Here, the cooling batch crystallization [43, 49, 55-59] as the dominate technology of the crystallization in the pharmaceutical industry will be investigated in this thesis.

### 2.2.1.1 Solubility, metastable zone width and supersaturation

The fundamental driving force for the crystallization is the difference between the chemical potential ( $\mu$ ) of the given substance in solution and in the crystal. The chemical potential is the molar Gibbs free energy of a substance and is a measure of the potential that a substance has and is defined as [60]

$$\mu = \mu_0 + RT \ln a \quad (2-31)$$

where  $\mu_0$  is the standard chemical potential,  $R$  is the universal gas constant,  $T$  is the absolute temperature, and  $a$  is the activity of a component. So, for the crystallization from a binary solution, the chemical potential difference is

$$\Delta\mu = RT \ln \left( \frac{a}{a^*} \right) = RT \ln S_s \quad (2-32)$$

$$S_s = e^{\frac{\Delta\mu}{RT}} \quad (2-33)$$

where  $a^*$  is the activity of a saturation and  $S_s$  is the fundamental supersaturation. Therefore, supersaturation is assumed as the driving force for the nucleation, growth of fresh nuclei, agglomeration and breakage in crystallization and it also has a major effect

on the polymorphism, and crystal size distribution [42].

The supersaturated solution refers to the solution containing more solute than its solubility under the unstable conditions. The supersaturation can be produced in the crystallizer by cooling, evaporation, addition of antisolvent, reaction or isoelectric precipitation. The cooling method is the most economical approach to generate the supersaturation by reducing the solubility with the temperature. But the prerequisite of this method is that the solubility of the solute should be a strong function of the temperature. This kind of crystallization is named cooling crystallization, which will be studied in this thesis. The supersaturation is determined by the difference between solution concentration and solubility( $c^*$ ) at the same temperature  $\Delta c = c - c^*$ , or the ratio of the two concentrations  $S_s = c/c^*$ .

Solubility refers to the concentration of a saturated solution which is equilibrated with the solute and cannot dissolve any more solute under certain temperature and pressure. As a foremost thermodynamical factor, the solubility curve is used to determine the starting and ending point of the crystallization.

The solution is unstable when it is supersaturated. But the spontaneous nucleation occurs only when the level of supersaturation is high enough. So, the maximum of the supersaturation degree without the spontaneous nucleation is named as metastable limit and the difference between the solubility curve and the metastable limit is referred to as the metastable zone width (MSZW). Solubility curve, red line in Figure 2-7, consists of a series of 'clear points' at which the suspended solid material disappears from a solution. While metastable limit curve, blue line in Figure 2-7, consists of a series of 'cloud points'

on the falling temperature profile at which the crystal nucleation is first observable.

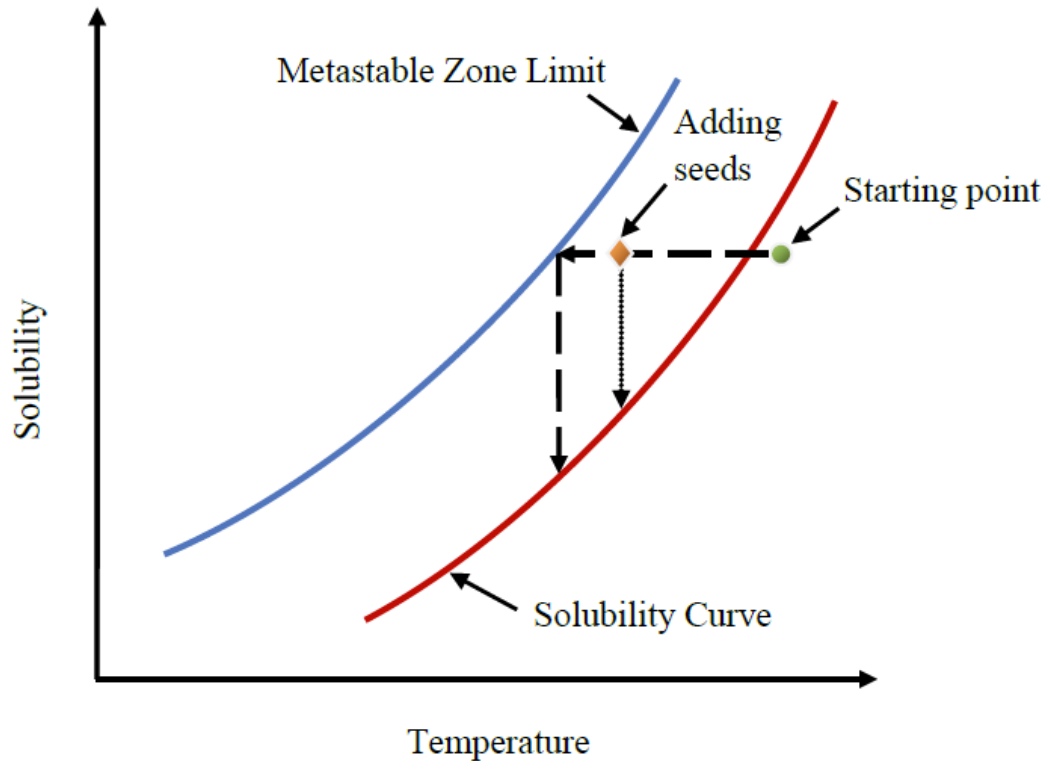


**Figure 2- 7: Equilibrium phase diagram, unseeded crystallization (dash line) and seeded crystallization (dot line).**

An accurate measurement of the solubility, metastable zone width (MSZW) and supersaturation is essential to design, operate and control the crystallization processes. There are several methods to measure the solubility curve. The polythermal method measures the temperature at which an incremental amount of solute just dissolves in the solution. The isothermal method determines the solubility by adding extra small portions of fresh solvent repeatedly into the known composition of the solution where the solid

phase is still visible until the solution becomes homogenous liquid phase under the isothermal conditions [60]. The solubility measurement can be completed only by differential scanning calorimetry (DSC) [61] according to the detection of release or absorption of heat when the solute dissolves in the solvent. The solubility also can be determined by measuring the concentration of the supernatant fluid in the solution where the solid phase is in excess by offline approaches, such as HPLC and gravimetric methods, or by online ways, such as density meter [62] and conductivity meter [63]. Recently, the attenuated total reflection Fourier transform infrared spectroscopy (ATR-FTIR) has emerged as an in-situ tool for the solubility measurement [43]. ATR-FTIR can be used to monitor the liquid concentration by measuring the changes of a totally internally reflected infrared beam when the attenuated evanescent wave of that beam is in contact with a sample. Since the small depth of penetration of the evanescent wave results in little or no interference of the solid phase on the ATR infrared spectrum of the solution, the solute concentration in the liquid phase can be determined by ATR-FTIR even in the presence of the solid phase. In addition to the experimental measurements, the solubility can also be predicted by model, in which our group has made a significant contribution [62, 64-67].

The MSZW is the maximum level of the supersaturation that can be influenced by mixing [68], cooling rate[69] and the presence of impurities [70]. The MSZW can be obtained accurately by cooling the supersaturated solution with known concentration until the first nuclei appear. Various technologies are adopted to obtain the MSZW [43, 71, 72]. The focused beam reflectance measurement (FBRM) is commonly applied to detect the occurrence of nucleation [71, 73, 74]. The principle of the FBRM is based on the

measurement of the chord length distribution (CLD) of the particles in front of the probe window by a rotating focused laser beam [73]. The technology of the ATR-FTIR couple with the FBRM is not only used to measure the solubility and MSZW but also to determine the degree of the supersaturation [57, 75-81]. The technology is verified to be a powerful method to monitor the polymorphism transformation [82-84] and the particle size [58, 85] during the crystallization process.

### **2.2.1.2 Nucleation and growth in a cooling batch crystallizer**

During the crystallization process, the nucleation and growth are incurred by supersaturation. The nucleation refers to a phenomenon of the birth of nuclei within a fluid. Primary nucleation occurs in a supersaturated solution which is the absence of crystals. It always happens in the unseeded process. Secondary nucleation is induced by the presence of crystals in the supersaturated solution. Following the nucleation, the crystal growth initiates immediately where the crystal size increases. Then the crystal growth competes with the nucleation to consume the available supersaturation in the solution until the solution concentration reaches the solubility of the solute at certain temperature. Those stages play a crucial role in determining the property of the final crystals, such as crystal size and crystal size distribution (CSD). However, the study of theoretical treatment of the nucleation kinetics is still not clear since the critical size of the clusters which lead to the nucleation is too small and cannot be measured by the current technology [86]. So, the nucleation kinetics in solution just can be characterized based on the empirical method [87-89]. The study of the growth process is easier than the nucleation. An excellent overview of published growth theory is available in literature [60, 90]. The desirable final product with uniform crystal size and the narrow CSD cannot

be achieved without the control of the supersaturation, nucleation and growth. Nowadays, these two stages can be detected by the in-suit technologies, such as FBRM, particle vision and measurement (PVM) [71] and process video imaging (PVI) [91].

## 2.2.2 The mathematical model of crystallization process

The crystallization process can also be described mathematically. The cooling batch is considered as a perfectly mixed batch crystallizer of constant volume with the crystal breakage and agglomeration neglected. The population balance equation (PBE), Eq. 2-34, for the size independent growth rate [52] and mass balance for the solute concentration in continuous phase, Eq. 2-35, are the main equations for the model.

$$\frac{\partial n(L,t)}{\partial t} + G(t) \frac{\partial n(L,t)}{\partial L} = 0 \quad (2-34)$$

$$\frac{dc(t)}{dt} = -\rho_c k_v \frac{dm_3(t)}{dt} = -3\rho_c k_v G(t) m_2(t) \quad (2-35)$$

where  $n$  is the population density,  $G$  is the size-independent crystal growth rate,  $L$  is the crystal length,  $c$  is the solute concentration,  $\rho_c$  is the crystal density, and  $k_v$  is the volume shape factor,  $m_i$  is the  $i$ th moment of the crystal size distribution, shown as

$$m_i(t) = \int_0^{\infty} n(L,t) L^i dL \quad (2-36)$$

where  $n(L,t)$  is the population density.

### 2.2.2.1 Unseeded cooling batch crystallization

In an unseeded cooling batch crystallizer, the nucleation ( $B$ ) dominates the growth process. The primary nucleation occurs in the one phase solution when the

supersaturation of the solution exceeds the metastable zone limit at this temperature and leads to the generation of a large number of the nuclei. The primary nucleation rate per unit mass of solvent can be represented by an empirical expression [87] as

$$B(t) = k_b \Delta c(t)^b \quad (2-37)$$

which is frequently used for the unseeded crystallizer [43, 56]. The secondary nucleation starts after the primary nucleation, which will be discussed in the following section.

Following the nucleation, the nuclei grow in size. The size-independent growth rate [52] is given as

$$G(t) = k_g \Delta c(t)^g \quad (2-38)$$

In the above equations,  $B$  is the nucleation rate,  $b$  is the nucleation order,  $G$  is the growth rate, and  $g$  is the growth order.  $k_b$ ,  $k_g$  are the nucleation and growth rate coefficients as functions of the temperature.

$$k_b = k_{b0} \exp\left(\frac{-E_b}{RT}\right) \quad (2-39)$$

$$k_g = k_{g0} \exp\left(\frac{-E_g}{RT}\right) \quad (2-40)$$

where  $k_{b0}$  and  $E_b$  are the frequency factor and the activation energy of nucleation, respectively. And  $k_{g0}$  and  $E_g$  are the frequency factor and the activation energy of growth, respectively. Here, the supersaturation is defined as

$$\Delta c = c - c^* \quad (2-41)$$

where  $c$  is the solution concentration calculated by the crystallization model and  $c^*$  is the solubility of the solute which is the function of the temperature. In a cooling batch crystallizer, temperature is a function of the time determined by the cooling profile.

The initial and boundary conditions for the unseeded crystallization are

$$c(0) = c_0 \quad (2-42)$$

$$T(0) = T_0 \quad (2-43)$$

$$n(0, t) = n^0 = \left. \frac{B(t)}{G(t)} \right|_{L=0} \quad (2-44)$$

$$n(L, 0) = 0 \quad (2-45)$$

where  $c_0$  is the initial concentration and  $T_0$  is the initial temperature.  $n^0$  and  $n(L, 0)$  are the boundary and initial conditions for population density.

The kinetics of the nucleation and growth, as well as the final crystal quality, in an unseeded crystallizer depends on the initial saturation concentration and the cooling rate. The unseeded crystallizer is not a common method of the cooling batch crystallization applied in the industry, since the nucleation as the dominant process causes a wide crystal size distribution and small crystal size. Compared with unseeded crystallizer, the seeded crystallizer can avoid those disadvantages under the certain operating conditions.



### 2.2.2.2 Seeded cooling batch crystallization

The secondary nucleation is the dominant nucleation in the seeded crystallization since the crystals already exist in the solution. The secondary nucleation rate can be described [49, 92] as

$$B(t) = k_b M_T \Delta c(t)^b \quad (2-46)$$

where  $M_T$  is called the magma or suspension density and can be obtained by

$$M_T = \rho_c k_v m_3 \quad (2-47)$$

The crystal growth rate in the seeded crystallization is the same as that in the unseeded crystallization shown in Eq. (2-38) since it occurs only when the solid phase exists.

The initial and boundary conditions are given by

$$c(0) = c_0 \quad (2-48)$$

$$T(0) = T_0 \quad (2-49)$$

$$n(0, t) = n^0 = \left. \frac{B(t)}{G(t)} \right|_{L=0} \quad (2-50)$$

$$n(L, 0) = \begin{cases} a_0 (L_{max} - L)(L - L_{min}) & L_{min} < L < L_{max} \\ 0 & \text{elsewhere} \end{cases} \quad (2-51)$$

where the coefficient for the parabolic distribution of the seeds,  $a_0$ , is based on the uniform crystal shape, and can be determined by the mass balance.  $L_{max}$  and  $L_{min}$  are the maximum and minimum size of the seeds.

To solve the PBE, the partial differential equation (PDE) was discretized and then transformed into a set of ordinary differential equations (ODEs). Since the ODEs proved to be stiff, the *ode15s* function in Matlab™ was used to solve these initial value problems (IVP) – ODEs.

The characteristics of the desired final produced crystals are the unimodal peak of the crystal size distribution (CSD) and the maximum of the crystal size. They can be induced by suppressing the secondary nucleation and increasing the crystal growth rate in the seeded crystallizer. In the cooling batch crystallization, the following approaches can be employed to achieve the desired final product. One approach is the optimization of the cooling profile or cooling rate. Many authors proved that the cooling rate should be slow in the beginning of the stage where the nucleation and crystal growth just occur and accelerate when the surface area of the solid is increased [55, 93-95]. Another approach is the control of the seed loading and the seed size. The seed should be added in the crystallizer before the nucleation happens to restrain the nucleation process. The larger seed loading leads to reduce the nucleation and increase the crystal growth, and the smaller seed size increases the surface area per unit mass and promotes the growth phenomenon as the dominant process [63, 96].

### **2.2.3 Direct crystallization for the pure enantiomers**

Gernez is first to uncover that the resolution of the double salt sodium ammonium racemate could be accomplished by adding the seeds of the object enantiomer in the supersaturated solution of the racemate in 1865 [97]. However, this method was not explained theoretically for almost a century until Secor summed up the studies of the

previous researchers and raised the rational approach for the direct crystallization in 1962 [97]. “Enantiomer, Racemate and Resolution”, as the classic book published in 1981, elaborated the characteristics of the racemates and their enantiomers and the principle of the resolution, which revitalized the interest in the resolution by direct crystallization. An upsurge for the study of direct crystallization came from the introduction of policy about the pure enantiomers by FDA in 1992 [98]. This resolution method has been drawing the significant attention since it has been demonstrated as a powerful solid-liquid separation technology for the purification of the enantiomers [51, 99-104]. Potter *et al.* [105] studied the oscillating crystallization of the enantiomers of the bicyclic lactam during the direct crystallization. The performance of the resolution of DL- threonine by direct crystallization had been studied by Proir *et al.* [106]. The research group led by Seidel-Morgenstern in Germany made significant contributions in the study of the direct crystallization. They used the polarimeter to online monitor the direct crystallization process [107], described this crystallization process by simplified mathematical model which was verified experimentally [108], extended the direct crystallization to the resolution of the racemic compound [109], experimentally and mathematically investigated the enantioseparation by direct crystallization in the two coupled vessels [103, 110], studied the direct crystallization in the chiral solvent [111, 112] and so on [113-117]. Ching’s group in Singapore also did some work on the direct crystallization. They applied the direct crystallization to the resolution of propranolol hydrochloride [102], 4-hydroxy-2-pyrrolidone [118] and so on [104, 119]. Our group has also studied the nucleation and growth kinetics of (*R*)- mandelic acid during the resolution of mandelic acid by direct crystallization [51]. Compared with other enantioseparation

technologies, direct crystallization allows to achieve high purity and low energy consumption. However, the main drawback of the direct crystallization is the requirement for the raw racemates and partially enriched solution. That means only the conglomerate and some racemic compound with close eutectic points can be separated using the direct crystallization with high purity and productivity. In this thesis, the pure enantiomers are obtained in a cooling batch crystallizer from a partially enriched solution with the desired enantiomer seeds. The set up of the crystallizer is shown in the Figure 2-8.

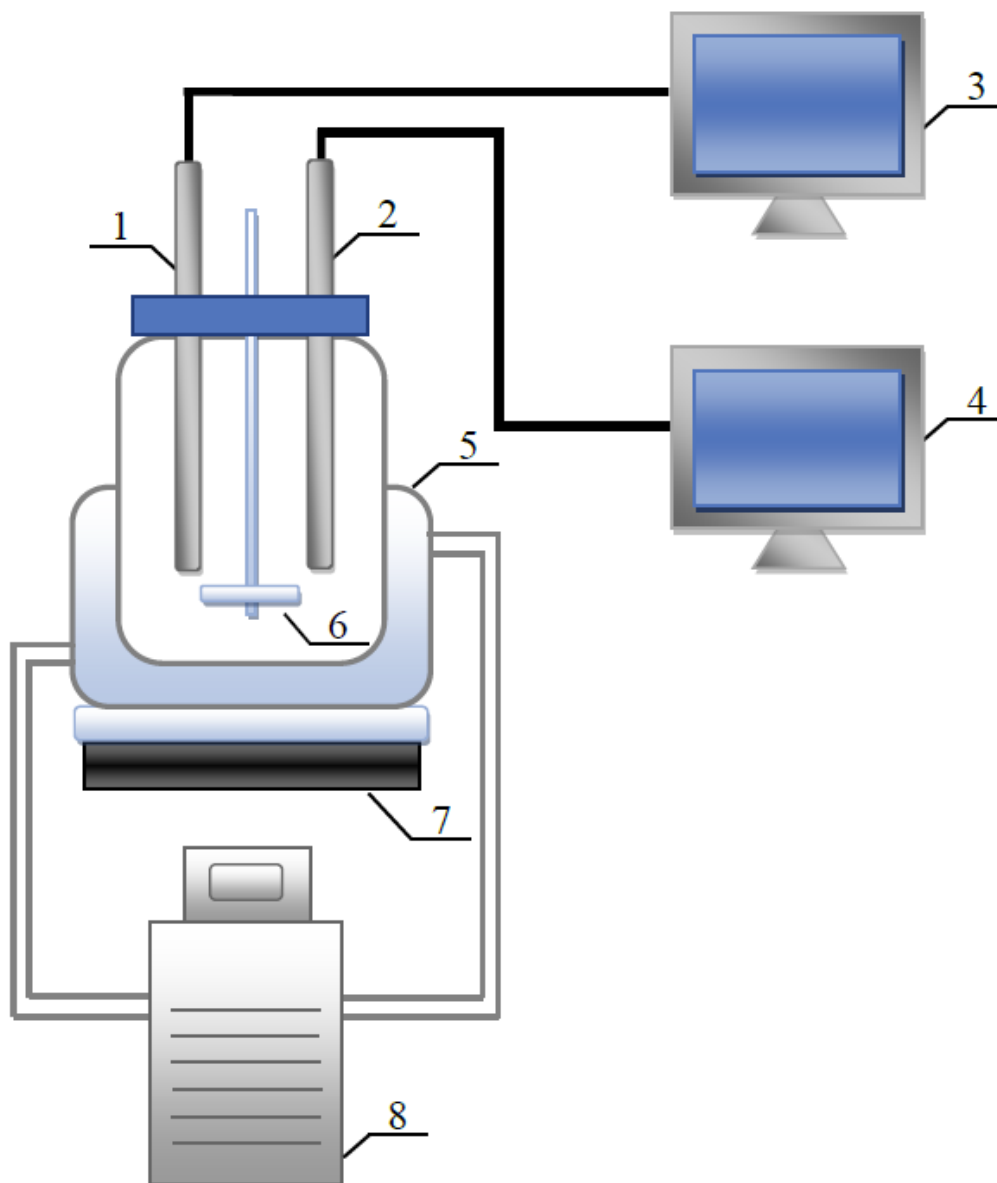


**Figure 2- 8: The setup of the crystallization experiment: 1.ATR-FTIR, 2.FBRM, 3.ATR-FTIR monitor, 4.FBRM monitor, 5. Double jacketed 200 mL glass crystallizer, 6.Magnetic stirring bar, 7. Magnetic stirrer, 8.Bath circulator.**

Figure 2-9 shows the ternary solubility phase diagram for the racemic compound (*Rac*). The different enantiomeric excess compounds can be considered as the physical mixture of the enantiomers and racemic compound, since the racemic compound is also the stable solid phase, which is the same as the two pure enantiomers (*R* and *S*). So, the one racemic compound diagram can be regarded as the combination of two conglomerate ternary solubility phase diagrams, *R-Rac* and *S-Rac*. They are both same, because of the symmetry in chiral system. In this figure, point A and C represent the solubility of the pure enantiomer and racemic compound, respectively, in the solvent at a given temperature  $T_{start}$ . Point B represents the eutectic point at this temperature. The tie line, *A-B-C*, is the solubility curve at this temperature. And *Solvent-B-E* is the eutectic line in the ternary phase diagram. One-phase region, unsaturated solution, is the area of *Solvent-A-B-C*, where enantiomer and racemic compound coexist as liquid phase. The areas of *A-B-R* and *C-B-Rac* represent the two-phase regions where pure enantiomers or racemic compound as solid phase or supersaturated solution coexist with saturated solution of a composition. And the triangle area *R-B-Rac* is the three-phase region for the two solid phases with solution at equilibrium [120].

To generate the pure *R*, we want the solution composition falls in the area of *Solvent-B-R*, since in these areas, the enantiomer is more than racemic compound in the solution, which is opposite with the area of *Solvent-B-Rac-C*. Because the two solid phases coexist in the area of *R-B-Rac*, the pure enantiomer cannot be obtained by enrichment method in this region. For a partially enriched solution of composition in the *Solvent-B-A* (point *D*), i.e. the solution from the Simulated Moving Bed (SMB) is dilute and undersaturated, it can be evaporated to remove a certain amount of solvent and then achieve to point *F*. The

mixture at point  $F$  is saturated at the  $T_{start}$ . But the  $R$ -enantiomer is more than the racemic compound in the solution. Then the solution is crystallized by cooling with  $R$ -enantiomer seeds as the enantiopure resolving agent until  $T_{end}$ . Using the seeds is to induce the growth of the  $R$ -enantiomer and inhibit the occurrence of the instantaneous nucleation of the racemic compound from the solution. The  $R$ -enantiomer is deposited along line  $FG$  until point  $G$  where the racemic compound and enantiomers are in equilibrium with the eutectic composition at  $T_{end}$ .

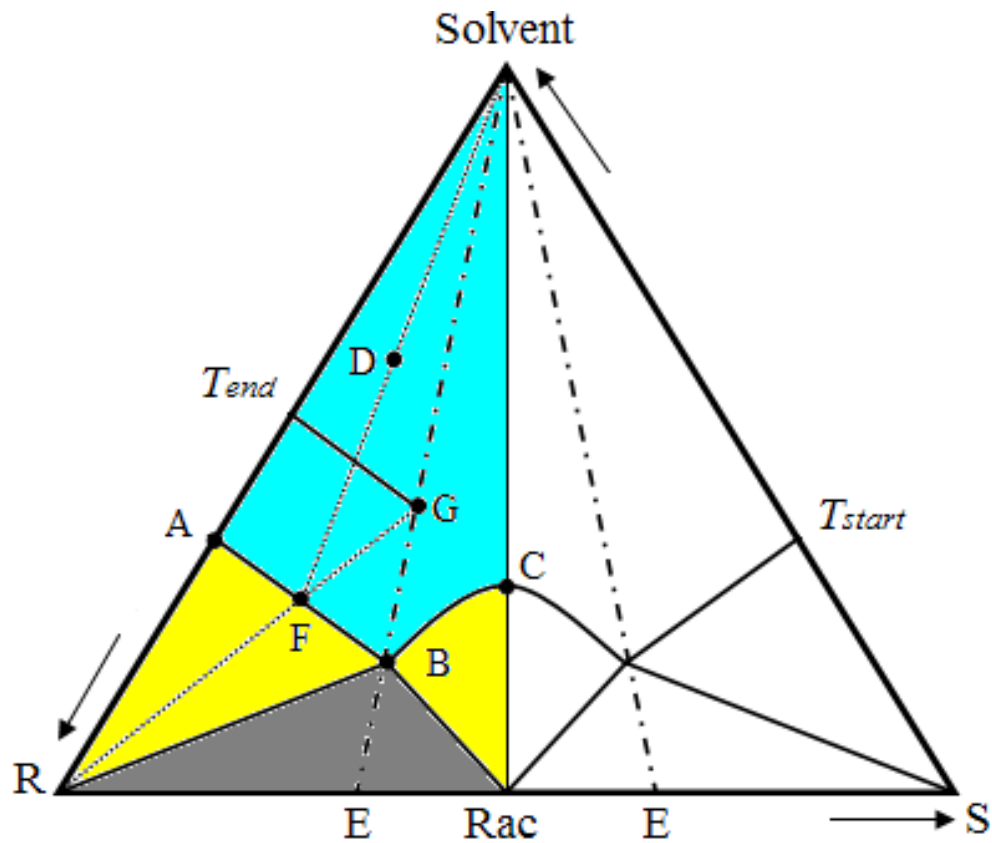


**Figure 2- 9: Principle of direct crystallization for racemic compound systems.**

## 2.3 Coupling of simulated moving bed chromatography and direct crystallization

The concept of coupling the simulated moving bed technology and direct crystallization refers to the partially enriched solution obtained from the SMB chromatography to be introduced into the seeded cooling batch crystallizer to gain the pure enantiomers. Lim *et al.* was first to propose and apply the coupling of SMB chromatography and selective crystallization for the Praziquantel system [121, 122]. Lorenz *et al.* analyzed the efficiency of the coupling process by designing the two processes separately [123]. Ströhlein *et al.* developed the design method for the optimal coupling process [124]. Amanullah *et al.* used and optimized this process for the Tröger's base system [125, 126]. Kaspereit *et al.* evaluated the hybrid process by a shortcut approach [127]. Gedicke *et al.* studied the design and feasibility of this process for stereoisomer separations [128]. Recently, Kaemmerer *et al.* employed the coupling process for the racemic bicalutamide [129].

It is obvious that the coupling process is an efficient method for the chiral separation. The lower purity requirement for SMB and solvent recycle can reduce the consumption of the solvent and chiral stationary phase demand to achieve the high purity enantiomers and high productivity economically. And the partially enriched solution can be obtained easily from the SMB chromatography.



## 2.4 Reference

1. Rajendran, A., G. Paredes, and M. Mazzotti, *Simulated moving bed chromatography for the separation of enantiomers*. Journal of Chromatography A, 2009. **1216**(4): p. 709-738.
2. Broughton, D.B. and C.G. Gerhold, *Continuous sorption process*. 1961.
3. Nicoud, R.M., et al., *Preparative scale enantioseparation of a chiral epoxide: Comparison of liquid chromatography and simulated moving bed adsorption technology*. Chirality, 1993. **5**(4): p. 267-271.
4. Negawa, M. and F. Shoji, *Optical resolution by simulated moving-bed adsorption technology*. Journal of Chromatography A, 1992. **590**(1): p. 113-117.
5. Guest, D.W., *Evaluation of simulated moving bed chromatography for pharmaceutical process development*. Journal of Chromatography A, 1997. **760**(1): p. 159-162.
6. Cavoy, E., et al., *Laboratory-developed simulated moving bed for chiral drug separations: Design of the system and separation of Tramadol enantiomers*. Journal of Chromatography A, 1997. **769**(1): p. 49-57.
7. Blehaut, J. and R.M. Nicoud, *Recent aspects in simulated moving bed*. Analisis, 1998. **26**(7): p. M60-M70.
8. Schulte, M. and J. Strube, *Preparative enantioseparation by simulated moving bed chromatography*. Journal of Chromatography A, 2001. **906**(1-2): p. 399-416.
9. Zhang, Z., et al., *Multiobjective optimization of SMB and varicol process for chiral separation*. AIChE Journal, 2002. **48**(12): p. 2800-2816.
10. Zhang, Y., K. Hidajat, and A.K. Ray, *Optimal design and operation of SMB bioreactor: production of high fructose syrup by isomerization of glucose*. Biochemical engineering journal, 2004. **21**(2): p. 111-121.
11. Zhang, Y., K. Hidajat, and A.K. Ray, *Enantio-separation of racemic pindolol on Formula Not Shown -acid glycoprotein chiral stationary phase by SMB and Varicol*. Chemical Engineering Science, 2007. **62**(5): p. 1364-1375.
12. Berg, C., *Hypersorption Process for Separation of Light Gases*. Transactions of the American Institute of Chemical Engineers, 1946. **42**(4): p. 665-680.

13. Kehde, H., et al., *Ethylene Recovery - Commercial Hypersorption Operation*. Chemical Engineering Progress, 1948. **44**(8): p. 575-582.
14. Fitch, G., M. Probert, and P. Tiley, 1952. *Preliminary studies of moving-bed chromatography*. Journal of the Chemical Society (Resumed), 1962: p. 4875-4881.
15. Zhang, Z.Y., M. Morbidelli, and M. Mazzotti, *Experimental assessment of PowerFeed chromatography*. AIChE Journal, 2004. **50**(3): p. 625-632.
16. Ruthven, D.M. and C. Ching, *Counter-current and simulated counter-current adsorption separation processes*. Chemical Engineering Science, 1989. **44**(5): p. 1011-1038.
17. Guiochon, G., et al., *Fundamentals of preparative and nonlinear chromatography*. Vol. 2nd. 2006, Amsterdam: Elsevier Academic Press. 975.
18. Yun, T., G. Zhong, and G. Guiochon, *Simulated moving bed under linear conditions: Experimental vs. calculated results*. AIChE Journal, 1997. **43**(4): p. 935-945.
19. Zhong, G. and G. Guiochon, *Analytical solution for the linear ideal model of simulated moving bed chromatography*. Chemical Engineering Science, 1996. **51**(18): p. 4307-4319.
20. Yun, T., G. Zhong, and G. Guiochon, *Experimental study of the influence of the flow rates in SMB chromatography*. AIChE Journal, 1997. **43**(11): p. 2970-2983.
21. Ahmad, T. and G. Guiochon, *Numerical determination of the adsorption isotherms of tryptophan at different temperatures and mobile phase compositions*. Journal of Chromatography A, 2007. **1142**(2): p. 148-163.
22. Lisec, O., P. Hugo, and A. Seidel-Morgenstern, *Frontal analysis method to determine competitive adsorption isotherms*. Journal Of Chromatography A, 2001. **908**(1-2): p. 19-34.
23. Gritti, F. and G. Guiochon, *Influence of a buffered solution on the adsorption isotherm and overloaded band profiles of an ionizable compound*. Journal of Chromatography A, 2004. **1028**(2): p. 197-210.
24. Zhang, Y., S. Rohani, and A.K. Ray, *Numerical determination of competitive adsorption isotherm of mandelic acid enantiomers on cellulose-based chiral stationary phase*. Journal of Chromatography A, 2008. **1202**(1): p. 34-39.

25. Enmark, M., et al., *Characterization of an unusual adsorption behavior of racemic methyl-mandelate on a tris-(3,5-dimethylphenyl) carbamoyl cellulose chiral stationary phase*. Journal of Chromatography A, 2011. **1218**(38): p. 6688-6696.
26. Asnin, L., K. Kaczmarski, and G. Guiochon, *The adsorption of Naproxen enantiomers on the chiral stationary phase Whelk-O1 under reversed-phase conditions: The effect of buffer composition*. Journal of Chromatography A, 2010. **1217**(45): p. 7055-7064.
27. Mihlbachler, K., et al., *Effect of the homogeneity of the column set on the performance of a simulated moving bed unit: I. Theory*. Journal of Chromatography A, 2001. **908**(1-2): p. 49-70.
28. Mihlbachler, K., et al., *Effect of the homogeneity of the column set on the performance of a simulated moving bed unit: II. Experimental study*. Journal of Chromatography A, 2002. **944**(1-2): p. 3-22.
29. Felinger, A., A. Cavazzini, and G. Guiochon, *Numerical determination of the competitive isotherm of enantiomers*. Journal of Chromatography A, 2003. **986**(2): p. 207-225.
30. Arnell, R., P. Forssen, and T. Fornstedt, *Accurate and rapid estimation of adsorption isotherms in liquid chromatography using the inverse method on plateaus*. Journal of Chromatography A, 2005. **1099**(1-2): p. 167-174.
31. Tóth, J., *Adsorption: theory, modeling, and analysis*. Vol. 107. 2002: CRC.
32. Felinger, A., D. Zhou, and G. Guiochon, *Determination of the single component and competitive adsorption isotherms of the 1-indanol enantiomers by the inverse method*. Journal of Chromatography A, 2003. **1005**(1-2): p. 35-49.
33. Charton, F. and R.-M. Nicoud, *Complete design of a simulated moving bed*. Journal of Chromatography A, 1995. **702**(1-2): p. 97-112.
34. Storti, G., et al., *Robust design of binary countercurrent adsorption separation processes*. AIChE Journal, 1993. **39**(3): p. 471-492.
35. Mazzotti, M., G. Storti, and M. Morbidelli, *Optimal operation of simulated moving bed units for nonlinear chromatographic separations*. Journal of Chromatography A, 1997. **769**(1): p. 3-24.
36. Mazzotti, M., G. Storti, and M. Morbidelli, *Robust design of countercurrent adsorption separation processes: 2. Multicomponent systems*. AIChE Journal, 1994. **40**(11): p. 1825-1842.

37. Mazzotti, M., G. Storti, and M. Morbidelli, *Robust design of countercurrent adsorption separation: 3. Nonstoichiometric systems*. AICHE Journal, 1996. **42**(10): p. 2784-2796.
38. Sá Gomes, P., M. Minceva, and A.E. Rodrigues, *Simulated moving bed technology: old and new*. Adsorption, 2006. **12**(5-6): p. 375-392.
39. Gentilini, A., et al., *Optimal operation of simulated moving-bed units for non-linear chromatographic separations: II. Bi-Langmuir isotherm* Part I of this series is Mazzotti et al., 1997. Journal of Chromatography A, 1998. **805**(1-2): p. 37-44.
40. Mazzotti, M., *Design of simulated moving bed separations: generalized Langmuir isotherm*. Industrial & Engineering Chemistry Research, 2006. **45**(18): p. 6311-6324.
41. Mazzotti, M., *Equilibrium theory based design of simulated moving bed processes for a generalized Langmuir isotherm*. Journal of Chromatography A, 2006. **1126**(1-2): p. 311-322.
42. Rohani, S., *Applications of the crystallization process in the pharmaceutical industry*. Frontiers of Chemical Engineering in China, 2010. **4**(1): p. 2-9.
43. Mao, S., et al., *Kinetics of (R, S)-and (R)-mandelic acid in an unseeded cooling batch crystallizer*. Journal Of Crystal Growth, 2010. **312**(22): p. 3340-3348.
44. He, G., et al., *Direct growth of  $\gamma$ -glycine from neutral aqueous solutions by slow, evaporation-driven crystallization*. Crystal Growth & Design, 2006. **6**(8): p. 1746-1749.
45. Schöll, J., et al., *Antisolvent Precipitation of PDI 747: Kinetics of Particle Formation and Growth*. Crystal Growth & Design, 2007. **7**(9): p. 1653-1661.
46. Rodríguez-Hornedo, N., et al., *Reaction crystallization of pharmaceutical molecular complexes*. Molecular pharmaceutics, 2006. **3**(3): p. 362-367.
47. Bramaud, C., P. Aimar, and G. Daufin, *Whey protein fractionation: Isoelectric precipitation of  $\alpha$ -lactalbumin under gentle heat treatment*. Biotechnology And Bioengineering, 1997. **56**(4): p. 391-397.
48. Tadayon, A., S. Rohani, and M.K. Bennett, *Estimation of nucleation and growth kinetics of ammonium sulfate from transients of a cooling batch seeded crystallizer*. Industrial & Engineering Chemistry Research, 2002. **41**(24): p. 6181-6193.
49. Qiu, Y. and Å.C. Rasmuson, *Estimation of crystallization kinetics from batch cooling experiments*. AICHE Journal, 1994. **40**(5): p. 799-812.

50. Yokota, M., A. Sato, and N. Kubota, *A simple method for evaluating kinetic parameters in non-isothermal batch crystallization*. Chemical Engineering Science, 2000. **55**(3): p. 717-722.
51. Zhang, Y., et al., *Nucleation and Growth Kinetics of (R)-Mandelic Acid from Aqueous Solution in the Presence of the Opposite Enantiomer*. Crystal Growth & Design, 2010. **10**(7): p. 2879-2887.
52. Randolph, A.D. and M.A. Larson, *Theory of particulate processes: analysis and techniques of continuous crystallization*. Vol. 1. 1971: Academic Press San Diego, CA.
53. Rohani, S., M. Haeri, and H. Wood, *Modeling and control of a continuous crystallization process Part 2. Model predictive control*. Computers & Chemical Engineering, 1999. **23**(3): p. 279-286.
54. Lawton, S., et al., *Continuous crystallization of pharmaceuticals using a continuous oscillatory baffled crystallizer*. Organic Process Research & Development, 2009. **13**(6): p. 1357-1363.
55. Miller, S.M. and J.B. Rawlings, *Model identification and control strategies for batch cooling crystallizers*. AIChE Journal, 1994. **40**(8): p. 1312-1327.
56. Mohameed, H.A., B. Abu-Jdayil, and M. Al Khateeb, *Effect of cooling rate on unseeded batch crystallization of KCl*. Chemical Engineering and Processing, 2002. **41**(4): p. 297-302.
57. Feng, L. and K.A. Berglund, *ATR-FTIR for determining optimal cooling curves for batch crystallization of succinic acid*. Crystal Growth & Design, 2002. **2**(5): p. 449-452.
58. Doki, N., et al., *Process control of seeded batch cooling crystallization of the metastable  $\alpha$ -form glycine using an in-situ ATR-FTIR spectrometer and an in-situ FBRM particle counter*. Crystal Growth & Design, 2004. **4**(5): p. 949-953.
59. Cheon, Y.H., K.J. Kim, and S.H. Kim, *A study on crystallization kinetics of pentaerythritol in a batch cooling crystallizer*. Chemical Engineering Science, 2005. **60**(17): p. 4791-4802.
60. Mullin, J.W., *Crystallization*. Vol. 3. 1993, Oxford ;; Boston: Butterworth-Heinemann. 527.
61. Mohan, R., H. Lorenz, and A.S. Myerson, *Solubility measurement using differential scanning calorimetry*. Industrial & Engineering Chemistry Research, 2002. **41**(19): p. 4854-4862.
62. Hojjati, H. and S. Rohani, *Measurement and prediction of solubility of paracetamol in water-isopropanol solution. Part 1. Measurement and data analysis*. Organic Process Research & Development, 2006. **10**(6): p. 1101-1109.

63. Kubota, N., et al., *Seeding policy in batch cooling crystallization*. Powder Technology, 2001. **121**(1): p. 31-38.
64. Manifar, T. and S. Rohani, *Measurement and prediction of solubility of four arylamine molecules in benzene, hexane, and methanol*. Journal of Chemical & Engineering Data, 2005. **50**(6): p. 1794-1800.
65. Hojjati, H. and S. Rohani, *Measurement and Prediction of Solubility of Paracetamol in Water-Isopropanol Solution. Part 2. Prediction*. Organic Process Research & Development, 2006. **10**(6): p. 1110-1118.
66. Mirmehrabi, M., S. Rohani, and L. Perry, *Thermodynamic modeling of activity coefficient and prediction of solubility: Part 2. Semipredictive or semiempirical models*. Journal Of Pharmaceutical Sciences, 2006. **95**(4): p. 798-809.
67. Zhang, Y., A. Ray, and S. Rohani, *Measurement and prediction of phase diagrams of the enantiomeric 3-chloromandelic acid system*. Chemical Engineering Science, 2009. **64**(2): p. 192-197.
68. O'Grady, D., et al., *The effect of mixing on the metastable zone width and nucleation kinetics in the anti-solvent crystallization of benzoic acid*. Chemical Engineering Research and Design, 2007. **85**(7): p. 945-952.
69. Nývlt, J., et al., *Metastable zone-width of some aqueous solutions*. Journal Of Crystal Growth, 1970. **6**(2): p. 151-162.
70. Sangwal, K. and E. Mielniczek-Brzoska, *Effect of impurities on metastable zone width for the growth of ammonium oxalate monohydrate crystals from aqueous solutions*. Journal Of Crystal Growth, 2004. **267**(3): p. 662-675.
71. Barrett, P. and B. Glennon, *Characterizing the metastable zone width and solubility curve using Lasentec FBRM and PVM*. Trans. IChemE, 2002. **80**: p. 799-805.
72. Simon, L.L., Z.K. Nagy, and K. Hungerbuhler, *Comparison of external bulk video imaging with focused beam reflectance measurement and ultra-violet visible spectroscopy for metastable zone identification in food and pharmaceutical crystallization processes*. Chemical Engineering Science, 2009. **64**(14): p. 3344-3351.

73. Tadayyon, A. and S. Rohani, *Determination of Particle Size Distribution by Par - Tec® 100: Modeling and Experimental Results*. Particle & Particle Systems Characterization, 1998. **15**(3): p. 127-135.
74. Barthe, S. and R.W. Rousseau, *Utilization of focused beam reflectance measurement in the control of crystal size distribution in a batch cooled crystallizer*. Chemical Engineering & Technology, 2006. **29**(2): p. 206-211.
75. Dunuwila, D.D., L.B. Carroll II, and K.A. Berglund, *An investigation of the applicability of attenuated total reflection infrared spectroscopy for measurement of solubility and supersaturation of aqueous citric acid solutions*. Journal of Crystal Growth, 1994. **137**(3-4): p. 561-568.
76. Lewiner, F., et al., *On-line ATR FTIR measurement of supersaturation during solution crystallization processes. Calibration and applications on three solute/solvent systems*. Chemical Engineering Science, 2001. **56**(6): p. 2069-2084.
77. Togkalidou, T., et al., *Solute concentration prediction using chemometrics and ATR-FTIR spectroscopy*. Journal Of Crystal Growth, 2001. **231**(4): p. 534-543.
78. Yu, Z.Q., P.S. Chow, and R.B.H. Tan, *Application of Attenuated Total Reflectance –Fourier Transform Infrared (ATR –FTIR) Technique in the Monitoring and Control of Anti-solvent Crystallization*. Industrial & Engineering Chemistry Research, 2006. **45**(1): p. 438-444.
79. Sheikhzadeh, M., M. Trifkovic, and S. Rohani, *Real-time optimal control of an anti-solvent isothermal semi-batch crystallization process*. Chemical Engineering Science, 2008. **63**(3): p. 829-839.
80. Trifkovic, M., M. Sheikhzadeh, and S. Rohani, *Kinetics Estimation and Single and Multi-Objective Optimization of a Seeded, Anti-Solvent, Isothermal Batch Crystallizer*. Industrial & Engineering Chemistry Research, 2008. **47**(5): p. 1586-1595.
81. Trifkovic, M., M. Sheikhzadeh, and S. Rohani, *Determination of metastable zone width for combined anti-solvent/cooling crystallization*. Journal Of Crystal Growth, 2009. **311**(14): p. 3640-3650.
82. O'Sullivan, B., et al., *In situ monitoring of polymorphic transitions*. Organic Process Research & Development, 2003. **7**(6): p. 977-982.

83. O'Sullivan, B. and B. Glennon, *Application of in situ FBRM and ATR-FTIR to the monitoring of the polymorphic transformation of D-mannitol*. Organic Process Research & Development, 2005. **9**(6): p. 884-889.
84. Schöll, J., et al., *In situ monitoring and modeling of the solvent-mediated polymorphic transformation of L-glutamic acid*. Crystal Growth & Design, 2006. **6**(4): p. 881-891.
85. Liotta, V. and V. Sabesan, *Monitoring and feedback control of supersaturation using ATR-FTIR to produce an active pharmaceutical ingredient of a desired crystal size*. Organic Process Research & Development, 2004. **8**(3): p. 488-494.
86. Schüth, F., et al., *Techniques for analyzing the early stages of crystallization reactions*. Solid State Sciences, 2001. **3**(7): p. 801-808.
87. Nývlt, J., *Kinetics of nucleation in solutions*. Journal of Crystal Growth, 1968. **3-4**(Journal Article): p. 377-383.
88. Denk Jr, E.G. and G.D. Botsaris, *Fundamental studies in secondary nucleation from solution*. Journal Of Crystal Growth, 1972. **13**: p. 493-499.
89. Erdemir, D., A.Y. Lee, and A.S. Myerson, *Nucleation of crystals from solution: classical and two-step models*. Accounts Of Chemical Research, 2009. **42**(5): p. 621-629.
90. Chernov, A., *Formation of crystals in solutions*. Contemporary Physics, 1989. **30**(4): p. 251-276.
91. Kougoulos, E., et al., *Use of focused beam reflectance measurement (FBRM) and process video imaging (PVI) in a modified mixed suspension mixed product removal (MSMPR) cooling crystallizer*. Journal Of Crystal Growth, 2005. **273**(3): p. 529-534.
92. Tavare, N. and J. Garside, *Simultaneous estimation of crystal nucleation and growth kinetics from batch experiments*. Chemical Engineering Research & Design, 1986. **64**(2): p. 109-118.
93. Jones, A., *Optimal operation of a batch cooling crystallizer*. Chemical Engineering Science, 1974. **29**(5): p. 1075-1087.
94. Lang, Y., A.M. Cervantes, and L.T. Biegler, *Dynamic optimization of a batch cooling crystallization process*. Industrial & Engineering Chemistry Research, 1999. **38**(4): p. 1469-1477.
95. Barrett, P., et al., *A review of the use of process analytical technology for the understanding and optimization of production batch crystallization processes*. Organic Process Research & Development, 2005. **9**(3): p. 348-355.



96. Hojjati, H. and S. Rohani, *Cooling and seeding effect on supersaturation and final crystal size distribution (CSD) of ammonium sulphate in a batch crystallizer*. Chemical Engineering and Processing: Process Intensification, 2005. **44**(9): p. 949-957.
97. Secor, R.M., *Resolution of Optical Isomers by Crystallization Procedures*. Chemical Reviews, 1963. **63**(3): p. 297-309.
98. Food and Drug Administration, *FDA'S policy statement for the development of new stereoisomeric drugs*. Chirality, 1992. **4**(5): p. 338-340.
99. Collet, A., M.J. Brienne, and J. Jacques, *Optical resolution by direct crystallization of enantiomer mixtures*. Chemical Reviews, 1980. **80**(3): p. 215-230.
100. Shiraiwa, T., et al., *Optical resolution by preferential crystallization of (2RS, 3SR)-2- amino- 3- chlorobutanoic acid hydrochloride*. Chirality, 1997. **9**(7): p. 656-660.
101. Lorenz, H., et al., *Crystallization of enantiomers*. Chemical Engineering & Processing, 2006. **45**(10): p. 863-873.
102. Wang, X., J. Lu, and C.B. Ching, *Application of direct crystallization for racemic compound propranolol hydrochloride*. Journal Of Pharmaceutical Sciences, 2007. **96**(10): p. 2735-2745.
103. Elsner, M.P., G. Ziomek, and A. Seidel -Morgenstern, *Efficient separation of enantiomers by preferential crystallization in two coupled vessels*. AIChE Journal, 2009. **55**(3): p. 640-649.
104. Lu, Y., X. Wang, and C.B. Ching, *Application of preferential crystallization for different types of racemic compounds*. Industrial & Engineering Chemistry Research, 2009. **48**(15): p. 7266-7275.
105. Potter, G.A., et al., *Oscillating Crystallization of (+) and (-) Enantiomers during Resolution by Entrainment of 2-Azabicyclo [2.2. 1] hept- 5- en- 3- one*. Angewandte Chemie International Edition in English, 1996. **35**(15): p. 1666-1668.
106. Profir, V.M. and M. Matsuoka, *Processes and phenomena of purity decrease during the optical resolution of-threonine by preferential crystallization*. Colloids and Surfaces A: Physicochemical and Engineering Aspects, 2000. **164**(2-3): p. 315-324.
107. Rodrigo Alvarez, A., H. Lorenz, and A. Seidel -Morgenstern, *Online monitoring of preferential crystallization of enantiomers*. Chirality, 2004. **16**(8): p. 499-508.
108. Elsner, M.P., et al., *Experimental study and simplified mathematical description of preferential crystallization*. Chirality, 2005. **17**(S1): p. S183-S195.

109. Lorenz, H., D. Polenske, and A. Seidel-Morgenstern, *Application of preferential crystallization to resolve racemic compounds in a hybrid process*. Chirality, 2006. **18**(10): p. 828-840.
110. Elsner, M.P., G. Ziomek, and A. Seidel-Morgenstern, *Simultaneous preferential crystallization in a coupled batch operation mode. Part II: Experimental study and model refinement*. Chemical Engineering Science, 2011. **66**(6): p. 1269-1284.
111. Tulashie, S.K., et al., *Potential of chiral solvents for enantioselective crystallization. 1. Evaluation of thermodynamic effects*. Crystal Growth and Design, 2008. **8**(9): p. 3408-3414.
112. Tulashie, S.K., H. Lorenz, and A. Seidel-Morgenstern, *Potential of Chiral Solvents for Enantioselective Crystallization. 2. Evaluation of Kinetic Effects*. Crystal Growth and Design, 2009. **9**(5): p. 2387-2392.
113. Polenske, D., H. Lorenz, and A. Seidel-Morgenstern, *Separation of Propranolol Hydrochloride Enantiomers by Preferential Crystallization: Thermodynamic Basis and Experimental Verification*. Crystal Growth & Design, 2007. **7**(9): p. 1628-1634.
114. Qamar, S., et al., *Numerical solutions of population balance models in preferential crystallization*. Chemical Engineering Science, 2008. **63**(5): p. 1342-1352.
115. Polenske, D., H. Lorenz, and A. Seidel-Morgenstern, *Potential of different techniques of preferential crystallization for enantioseparation of racemic compound forming systems*. Chirality, 2009. **21**(8): p. 728-737.
116. Czaplá, F., et al., *Parameterization of population balance models for polythermal auto seeded preferential crystallization of enantiomers*. Chemical Engineering Science, 2009. **64**(4): p. 753-763.
117. Tulashie, S.K., et al., *Chiral Task-Specific Solvents for Mandelic Acid and Their Impact on Solution Thermodynamics and Crystallization Kinetics*. Crystal Growth & Design, 2011.
118. Wang, X.J. and C.B. Ching, *A systematic approach for preferential crystallization of 4-hydroxy-2-pyrrolidone: Thermodynamics, kinetics, optimal operation and in-situ monitoring aspects*. Chemical Engineering Science, 2006. **61**(8): p. 2406-2417.
119. Wang, X., et al., *Intrinsic MSZW characteristics of racemic species: Implication for chiral crystallization*. AIChE Journal, 2008. **54**(9): p. 2281-2292.
120. Jacques, J., A. Collet, and S.H. Wilen, *Enantiomers, racemates, and resolutions*. 1981, New York ;; Toronto: Wiley. 447.

121. Lim, B.g., et al., *Solubility phase diagram of praziquantel enantiomeric system*. Chirality, 1995. **7**(2): p. 74-81.
122. Lim, B.-G., et al., *Recovery of (-)-praziquantel from racemic mixtures by continuous chromatography and crystallisation*. Chemical Engineering Science, 1995. **50**(14): p. 2289-2298.
123. Lorenz, H., P. Sheehan, and A. Seidel-Morgenstern, *Coupling of simulated moving bed chromatography and fractional crystallisation for efficient enantioseparation*. Journal of Chromatography A, 2001. **908**(1-2): p. 201-214.
124. Ströhlein, G., M. Schulte, and J. Strube, *Hybrid processes: Design method for optimal coupling of chromatography and crystallization units*. Separation Science And Technology, 2003. **38**(14): p. 3353-3383.
125. Amanullah, M., S. Abel, and M. Mazzotti, *Separation of Tröger's Base Enantiomers Through a Combination of Simulated Moving Bed Chromatography and Crystallization*. Adsorption, 2005. **11**(1, suppl. Supl. 1, pp. 893-897): p. July.
126. Amanullah, M. and M. Mazzotti, *Optimization of a hybrid chromatography-crystallization process for the separation of Troger's base enantiomers*. Journal of Chromatography A, 2006. **1107**(1-2, pp. 36-45): p. February.
127. Kaspereit, M., et al., *Shortcut method for evaluation and design of a hybrid process for enantioseparations*. Journal of Chromatography A, 2005. **1092**(1): p. 43-54.
128. Gedicke, K., et al., *Conceptual design and feasibility study of combining continuous chromatography and crystallization for stereoisomer separations*. Chemical Engineering Research and Design, 2007. **85**(7): p. 928-936.
129. Kaemmerer, H., et al., *Study of system thermodynamics and the feasibility of chiral resolution of the polymorphic system of malic acid enantiomers and its partial solid solutions*. Crystal Growth and Design, 2009. **9**(4): p. 1851-1862.

## **Chapter 3**

### **Chromatographic Resolution and Isotherm Determination of (*R,S*)-Mandelic Acid on Chiralcel-OD Column**

A version of this chapter was published as:

Mao, S.; Zhang, Y; Rohani, S.; Ray, A.K Chromatographic Resolution and Isotherm Determination of (*R,S*)-Mandelic Acid on Chiralcel-OD Column, accepted for publication in Journal of Separation Science.

### 3.1 Introduction

There is an increased demand for the separation of racemic compounds into their chiral constituents in the pharmaceutical and biochemical industries due to the recognition of differences in pharmacological activity of enantiomeric molecules. In recent years, preparative high performance liquid chromatography (HPLC) using chiral stationary phase (CSP) has become one of the best technologies for chiral separations because of its wide range of applications, ease of operation, high efficiency and reproducibility. Nowadays, simulated moving bed (SMB) chromatography, a well-developed continuous liquid chromatographic technique, has been widely used for the enantioseparation. Enantioseparation by SMB chromatography is usually operated under strongly nonlinear conditions. Therefore, a good understanding of the competitive adsorption isotherms is essential for the design and optimization of such separation process [1, 2]

The competitive isotherm data can be acquired by several chromatographic methods. All have their advantages and limitations in terms of rapidity, consumption of chemicals, and accuracy[3, 4]. Frontal analysis (FA) is considered to be the most accurate method for adsorption isotherm determination[5, 6]. In frontal analysis, the equilibrium amounts adsorbed in the stationary phase are determined directly from the experimental data. Isotherm parameters can then be acquired by fitting the equilibrium data to different isotherm models. The other commonly used method is the pulse or perturbation method (PM), which derives the isotherm parameters from a least square fitting of the simulated eluted times of perturbations at different feed concentrations to the experimental ones[3,

7]. Both methods are of high accuracy, however, they suffer a large amount of solute and time consumptions.

Numerical methods can also be used for determining competitive adsorption isotherms from overloaded elution profiles. The so-called inverse method (IM) allows the rapid estimation of the best values of the isotherm parameters by minimizing the difference between the overloaded band profiles generated from the model and those measured from the experiment [1, 8-11]. IM was first used to determine the competitive adsorption isotherm parameters of the ketoprofen enantiomers on a cellulose-based chiral stationary phase by James *et al.* [8]. Recently, comparison of the front analysis and inverse method on the estimation of adsorption isotherm of the proline in hydrophilic interaction chromatography was studied by Vajda *et al.*[12]. And Cornel *et al.* developed the direct inverse method which used directly the overloaded profiles from the detector signals without any calibration [11]. Compared to FA and PM, inverse method is fast and consumes the least amount of solutes, however, the isotherm derived from this method can be accurate only within the range of concentration extending from zero to the band maximum.

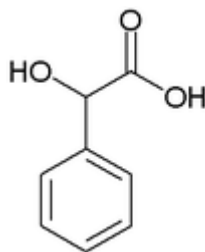


**Figure 3- 1: Molecular structure of mandelic acid.**

The purpose of this work is to study the resolution of racemic mandelic acid ((*R*, *S*)-MA, Fig. 3-1) and the competitive adsorption isotherm of its chiral constituents, i.e., (*R*)-MA and (*S*)-MA under nonlinear conditions. Kaspereit *et al.* [13] has studied the influence of the adsorption isotherm parameters of the mixture of (*R*)-MA and (*S*)-MA on the performance of the SMB with the different column and mobile phase. Zhang *et al.* [14] has studied the competitive adsorption isotherm of (*R*)-MA and (*S*)-MA based on the solution of an equimolar mechanical mixture of pure (*R*)-MA and (*S*)-MA. However, mandelic acid usually exists as the racemic compound [15, 16] which is present in equal quantities in a well-defined arrangement within the crystal lattice. The solid-liquid equilibria of mandelic acid system are shown in Figure 3-2 [16]. It can be seen from Figure 3-2 that melting temperature of (*R,S*)-MA is much higher than that of equimolar mechanical mixture of pure (*R*)-MA and (*S*)-MA . Therefore, the solubility of (*R,S*)-MA in liquid solvent is much lower and this lower solubility of (*R,S*)-MA will have some effect on its resolution by liquid chromatography [14, 17]. In this work resolution and competitive adsorption isotherm study of (*R,S*)-MA is carried out as the first step toward a future achievement of enantioseparation of (*R,S*)-MA using the hybrid SMB chromatography and crystallization process. The selection of the optimal mobile phase for the resolution of (*R,S*)-MA on the cellulose tris(3,5-dimethylphenylcarbamate) chiral stationary phase as well as the determination of the competitive isotherms of (*R,S*)-MA by inverse method is majorly presented in this study.

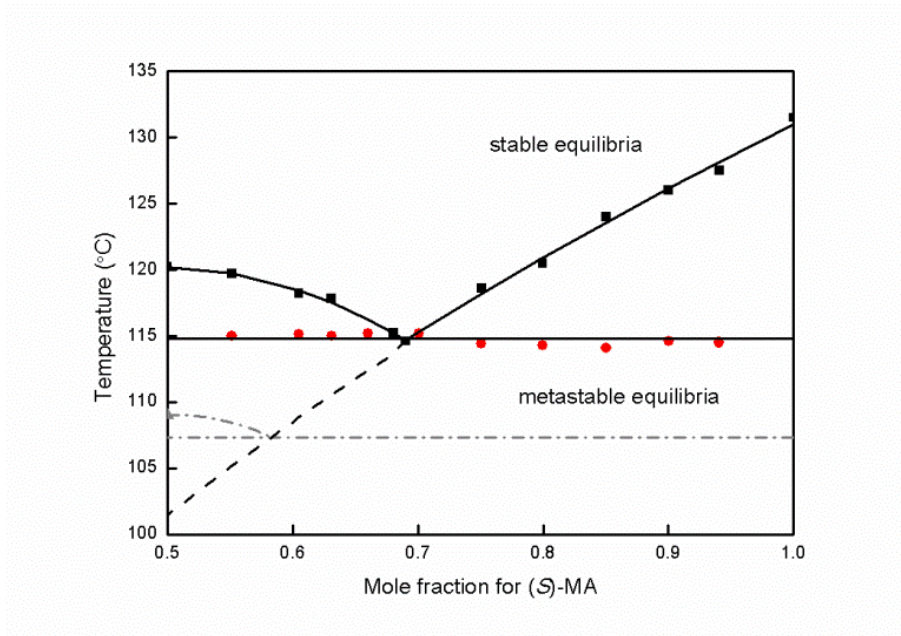


Figure 3- 2: Binary phase diagram of the racemic mandelic acid [16].

## 3.2 Modeling

### 3.2.1 Competitive modified Langmuir adsorption isotherm model

To determine the most suitable isotherm parameters by inverse method, different isotherm models need to be used. The competitive modified Langmuir adsorption isotherm was applied to describe the competitive retention mechanism of chiral molecules on cellulose-based chiral stationary phase [18]. Two different types of binding sites with either one being homogeneous on the surface of the stationary phase are assumed in this model. Competitive modified Langmuir isotherm model is written as:

$$q_i^* = m_i c_i + \frac{q_s b_i c_i}{1 + \sum_{j=1}^2 b_j c_j} \quad (3-1)$$



where  $q_i^*$  is the adsorbed amount of component  $i$  in the stationary phase equilibrated with the mobile phase at the concentration  $c_i$ .  $m_i$  is the coefficient for the non-specific adsorption sites. And  $q_s$  and  $b_i$  are the saturation capacities and the equilibrium constants for component  $i$  ( $i=1$  or  $2$ ), respectively. The components 1 and 2 represent the less retained component ((*S*)-MA) and more retained component ((*R*)-MA), respectively. It should be noticed that the adsorption isotherm was studied here only for the final mobile phase we used without considering the effects of acid and alcoholic content, which have been studied by other researchers [19-21].

### 3.2.2 Column model

The transport dispersive (TD) model is applicable in liquid chromatography to describe the mass balances of solutes in liquid and solid phases as well as the mass transfer of solutes between phases. In this model, the isothermal operation of a chromatographic column is described by a dispersed plug-flow model with linear-driving-force approximation for mass transfer [5, 6, 14]. The lumped solid-diffusion version of the model can be written as:

$$\frac{\partial c_i}{\partial t} + \frac{1-\varepsilon}{\varepsilon} \cdot \frac{\partial q_i}{\partial t} + u \cdot \frac{\partial c_i}{\partial z} = D_L \cdot \frac{\partial^2 c_i}{\partial z^2} \quad (3-2)$$

$$\frac{\partial q_i}{\partial t} = k_v(q_i^* - q_i) \quad (3-3)$$

where  $c_i$  and  $q_i$  are the concentrations of the solute in the liquid and solid phases, respectively;  $z$  is space coordinate and  $t$  is time;  $\varepsilon$  is the void fraction of the column;  $u$  is interstitial fluid velocity;  $D_L$  is the dispersion coefficient and calculated in section 4.2.1[22]; while  $k_v$  is the lumped rate coefficient.

The initial conditions for Eqs. (3-2) and (3-3) are given by

$$c_i(0, z) = 0, \quad q_i(0, z) = 0 \quad (3-4)$$

The boundary conditions at the column:

$$c_i(t, 0) = c_{F,i} \quad \text{when } 0 < t < t_p \quad (3-5)$$

$$c_i(t, 0) = 0 \quad \text{when } t > t_p \quad (3-6)$$

$$D_L \left. \frac{\partial c_i}{\partial z} \right|_{z=L} = 0 \quad (3-7)$$

where  $c_{F,i}$  is the feed concentration of the component,  $t_p$  is the length of a rectangular injection and  $L$  is the column length. The rectangular injection profiles have been employed in the calculation for the sake of simplicity. Although the use of real injection profiles would give us slightly more accurate results of the isotherm parameters, this would generate much complexity in the simultaneous fitting of the isotherm parameters because the injection profiles become more eroded with the increasing flow rates and size of the solute [23-25]. The error generated from the simplified injection profiles is maximum 2-3% [14, 23], which is acceptable in this case.

To solve these equations, the partial differential equations (PDEs) in Eqs. (3-2) and (3-3) were discretized and transformed into a set of ordinary differential equations (ODEs) using the method of lines. These resultant ODEs together with Eqs. (3-4)-(3-7) were then solved by a stiff ODE solver, DIVPAG which is based on Gear's method in IMSL (International Mathematics and Statistics Library), to get the calculated concentration profiles.

### 3.2.3 Isotherm parameters estimation

To determine the isotherm parameters, inverse method was used to minimize the difference between the experimental and calculated concentration profiles by the isotherm model and column model. The optimal set of the parameter values,  $[m_1, m_2, q_s, b_1, b_2, k_v]$ , can be generated by minimizing the error function  $f(k)$  defined as below,

$$f(k) = \min_{\theta} \sum_{j=1}^k (c_j^{exp} - c_j^{cal})^2, \theta = [m_1, m_2, q_s, b_1, b_2, k_v] \quad (3-8)$$

where  $k$  is the total number of the experimental data. There are 2001 experiment data for the band profile of Runs 7 to 15. The optimization is carried out by tuning those seven variables to minimize the error function. Non-dominated sorting genetic algorithm (NSGA-II-JG) [23] was used in this study to obtain the best-fit values of the isotherm parameters.

## 3.3 Experimental

### 3.3.1 Equipment

The experiments for the screening of mobile phase and the frontal analysis were performed on an Agilent 1200 series liquid chromatography system (Agilent Technologies, Palo Alto, CA, USA), which consists of a vacuum degasser, a quaternary pump, an auto injector with a 100 $\mu$ L sample loop, a thermostatted column compartment, a diode array and multiple wave length UV detector and the Agilent chemstation software. The detector was calibrated for each of the mobile phases used, at each temperatures set, and at the wavelengths of 254 and 280 nm. Linear calibration curve was

obtained in each case, which was further employed to determine the concentrations of the solutes.

The overload band profiles for inverse method were measured using the laboratory preparative chromatographic system, which includes the online vacuum degasser (Agilent Technologies, CA, USA), the Jasco PU-2080 pump (Jasco, Tokyo, JP), an injector with 50 $\mu$ L (Vici Valco, TX, USA) and the Jasco UV-2075 (Jasco, Tokyo, JP). All the wavelength of UV detectors was set at 254nm and calibration of detector was made using standard mandelic acid solutions with different concentrations. The calibration curve shows extremely good linearity.

A 100mm $\times$ 10mm semi-preparative Chiralcel OD column (Chiral Technologies, West Chester, PA, USA), packed with cellulose tris(3,5-dimethylphenylcarbamate) coated on 20  $\mu$ m silica-gel substrate, was used for all measurements. The total column void fraction was 0.708, determined by the retention volume of 1,3,5-tri-tert-butylbenzene (TTB) (TCI American, Portland, USA).

### **3.3.2 Materials**

The (*R,S*)-MA (99%) was purchased from Alfa Aesar (Heysham Lancashire, UK). Hexane (Calendon, Gergetown, ON, CA), isopropyl alcohol (IPA), (Calendon, Gergetown, ON, CA), and trifluoroacetic acid (TFA), (Alfa Aesar, MA, USA) were all HPLC grade.

### **3.3.3 Solubility measurement of (*R,S*)-MA**

Solubility of (*R,S*)-MA in the mobile phase with different compositions of hexane and IPA (hexane/IPA: 100/0, 90/10, 85/15, 80/20, 70/30, 60/40 (v/v)) was measured under room temperature ( $23 \pm 0.5^\circ\text{C}$ ). This measurement was conducted by adding the weighted solute in the 2mL prepared solvent followed by equilibrium for 2 hours and repeated those steps until the solutions became saturated. After the equilibrium of the final solution for 24 hours, pipet 100  $\mu\text{L}$  of supernates into individual 10 mL volumetric flask. Dilute to volume with the corresponding mobile phases. The solubility of (*R,S*)-MA in different mobile phases was then determined by measuring the concentration of the diluted solutions using HPLC. It should be mentioned that all the sample solutions used for isotherm determination were below the solubility of (*R,S*)-MA in the corresponding mobile phases.

### **3.3.4 Resolution of (*R,S*)-MA and isotherm determination**

All experiments were performed at room temperature ( $23 \pm 0.5^\circ\text{C}$ ). Experiments with either small injection (pulse test) or large injection (frontal analysis) were conducted. The major purposes of the pulse test are twofold. Firstly, screening the best mobile phase for the resolution of (*R,S*)-MA was performed by pulse test. Secondly, pulse tests also aimed to obtain elution concentration profiles of (*R,S*)-MA, which would have been used to derive the isotherm parameters by inverse method. Mobile phase with different compositions of hexane/IPA/TFA were used to resolve (*R,S*)-MA. Different flow rates of mobile phase were also tested for the good resolution of (*R,S*)-MA with different injection amounts. Details for the operating parameters can be found in Table 3-1.

**Table 3- 1: The operating conditions for the isotherm measurements**

Run	Mobile phase Hexane/IPA/TFA (v/v/v)	Flow rate (mL/min)	Injection amount ( $\mu\text{g}$ )
1	90/10/0.3	4	500
2	85/15/0.3	4	500
3	80/20/0.3	4	500
4	70/30/0.3	4	500
5	85/15/0	4	500
6	85/15/0.15	4	500
7	85/15/0.3	2	300
8	85/15/0.3	2	900
9	85/15/0.3	2	1500
10	85/15/0.3	3	300
11	85/15/0.3	3	900
12	85/15/0.3	3	1500
13	85/15/0.3	4	300
14	85/15/0.3	4	900
15	85/15/0.3	4	1500

The single step frontal analysis method was used to verify the adsorption isotherm derived by inverse method. Frontal analysis experiment was carried out using Agilent

1200 series liquid chromatography system equipped with the semi-preparative Chiralcel OD column. Two pump channels were used, with one for pure mobile phase and the other one for the sample solution with a concentration of 26.2 g/L. After the column was pre-equilibrated with the mobile phase, the sample solution, mixed with mobile phase proportionally, was fed into the column. The flow rate of the mixed solution was 3.0 mL/min. When the first plateau was reached, the effluent was collected before the next breakthrough appeared. After the column was equilibrated with the solution and the elution of the breakthrough curves was recorded by the DAD detector at 280nm wavelength, the column was regenerated by washing the sample away with the pure mobile phase and ready for the next injection. The sample solution of (R,S)-MA and the collected effluent were analyzed with HPLC. The series of frontal analysis experiments was performed by the proportions of the sample solution in the mixed solution with 1, 2.5, 5, 7.5, 10, 25, 50, 75, 100%. The amount adsorbed in stationary phase,  $q_i^*$ , in equilibrium with a mobile phase concentration,  $c_{F,i}$ , can be calculated by [24]

$$q_i^* = \frac{(t_2 - t_0) \times (c_{F,i} - c_{initial,i}) - (t_2 - t_1) \times (c_{m,i} - c_{initial,i})}{\frac{1-\varepsilon}{\varepsilon} t_0} \quad (3-9)$$

where the value of  $c_{initial,i}$  is 0 in this case and  $c_{m,i}$  is the concentration of component  $i$  in the first plateau;  $t_0$  is the holdup time of the column,  $t_1$  and  $t_2$  are the retention time of the first and the second breakthrough fronts, respectively.

These measured equilibrium data will be used to verify the accuracy of the isotherm derived from inverse method.

## 3.4 Results and discussion

### 3.4.1 Choice of mobile phase

Selection of a suitable mobile phase for the enantioseparation of (*R,S*)-MA is a little bit challenging. As normal phase liquid chromatographic mode was used to resolve (*R,S*)-MA in this study, the choice for mobile phase has been restricted to the non-polar or weakly polar organic solvent, usually the mixture of hydrocarbon (hexane or heptane) and alcohol. Nevertheless, (*R,S*)-MA has very limited solubility in weakly polar organic solvents. In order to increase the solubility of (*R,S*)-MA in mobile phase, strongly polar alcohol needs to be used, which may result in a decrease in resolution.

#### 3.4.1.1 Effect of isopropanol content

Alcohol concentration in the mobile phase has been proved to have great influence on the resolution of racemic compounds on the polysaccharide-based CSPs [25-28]. In this study, the effects of isopropanol (IPA) concentration in mobile phase on the resolution of (*R,S*)-MA are twofold. Firstly, IPA concentration has a remarkable influence on the solubility of (*R,S*)-MA. The solubility of (*R,S*)-MA with the different IPA concentrations in the mobile phase is shown in Figure 3-3. It is observed that (*R,S*)-MA is insoluble in pure hexane and the solubility of (*R,S*)-MA increases exponentially with the increase of IPA concentrations. This experiment result coincides with the research observation by Miller *et al.* [29] which reported that the racemic compounds have higher solubility in alcoholic solvents than the mixed alcohol-hydrocarbon solvent with high hydrocarbon content. In liquid chromatography, the concentration overloading conditions typically



result in better performance than volume overloading, therefore, mobile phase resulting in high solute solubility is preferred.

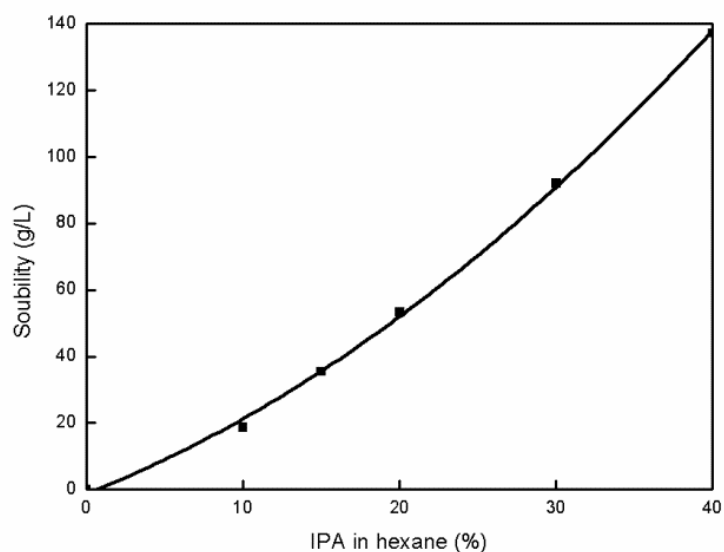


**Figure 3- 3: Solubility of (R,S)-MA with different ethanol proportions in the mobile phase.**

Secondly, IPA concentrations in mobile phase also affect the retention, band profile shapes and enantioseparation of the two enantiomers. It was found that retention times of (*R*)-MA and (*S*)-MA become shorter with the increasing amount of IPA in mobile phase. But poor resolution from Table 3-2 was obtained when higher isopropanol concentrations were used in the mobile phase. Comparison of the elute profiles for different isopropanol contents is demonstrated in Figure 3-4. These results once again prove that alcoholic modifier molecules, IPA in this case, compete with solute molecules for the chiral adsorption sites on the CSP. As a result, the separation performance, i.e. the retention,

enantioselectivity and resolution, has been altered by changes of the IPA concentration in the mobile phase.

**Table 3- 2: The selectivity ( $\alpha$ ) and resolution ( $R_s$ ) of the band profiles**

Run	1	2	3	4	5	6
* $\alpha$	1.48	1.57	1.64	1.73	1	1.56
* $R_s$	2.37	2.24	2.07	1.69	0	2.22

\*Selectivity ( $\alpha$ ) and resolution ( $R_s$ ) are defined as  $\alpha = \frac{t_2-t_0}{t_1-t_0}$  and  $R_s = \frac{t_2-t_1}{0.5(w_2+w_1)}$ ,

respectively.

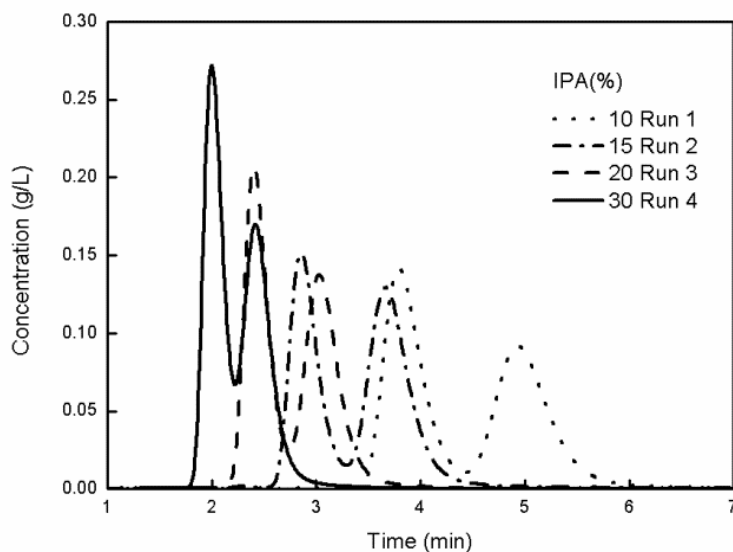


**Figure 3- 4: Influence of IPA proportion in the mobile phase on the elution profiles of (R)-MA and (S)-MA.**

### 3.4.1.2 Effect of the trifluoroacetic acid

When polysaccharide-based CSPs are used, it has long been recognized that basic or acidic additives enhance the separation quality, both in terms of selectivity and peak shape efficiency [30, 31]. In this study, trifluoroacetic acid (TFA) was added into the mobile phase to increase the enantioselectivity and minimize peak broadening. In Figure 3-5 the impact of TFA on retention and peak shapes is shown. It is observed that retention decreases with increasing additive level between 0 and 0.3v%. Enantioselectivity and column efficiency also increase between 0 and 0.3v% TFA. These observations indicate that TFA exerts its effect by minimizing interactions between solute molecules and non-selective binding sites of the CSP. However, TFA higher than 0.5v% in mobile phase is not recommended because CSP may be damaged under high concentration of acidic additives.

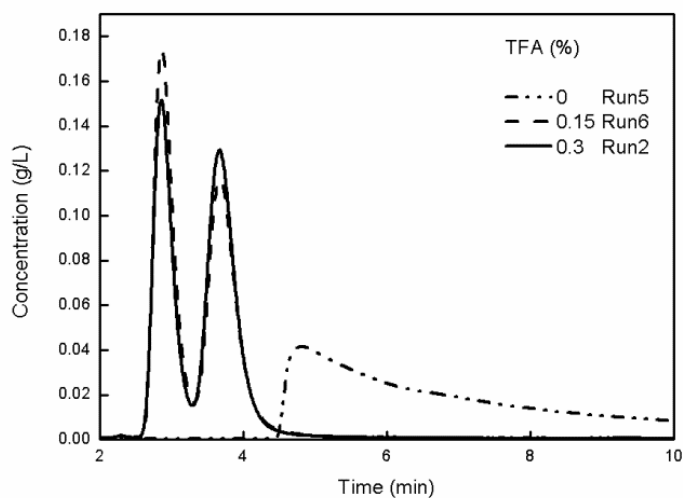


**Figure 3- 5: Influence of TFA proportion in the mobile phase on the retention and enantioselectivity of (R,S)-MA.**

The mixed solution, hexane/IPA/TFA with 85/15/0.3 (v/v/v) were selected as the mobile phase for the enantioseparation of (R,S)-MA in this study based on the overall consideration of the solubility, retention time, resolution performance of (R,S)-MA as well as the column limitation,

### 3.4.2 Parameters estimation, optimization and validation for competitive adsorption isotherm

#### 3.4.2.1 Axial dispersion coefficient, $D_L$

The axial dispersion coefficient,  $D_L$ , can be calculated by the molecular diffusion and eddy diffusion [22] in terms of

$$D_L = 0.7D_m + 0.5ud_p \quad (3-10)$$

where  $d_p$  is the diameter of the particle size.  $D_m$  is the molecular diffusion coefficient of the solute in the mobile phase which can be determined as follows

$$D_m = [D_m(w_{hexane} = 1)]^{w_{hexane}} [D_m(w_{IPA} = 1)]^{w_{IPA}} \quad (3-11)$$

where  $w_{hexane}$  and  $w_{IPA}$  are molar fractions of hexane and IPA which are 0.77 and 0.23, respectively. The equation above is based on the diffusion coefficient in the dilute solutions [32]. The  $D_m(w_{hexane}=1)$  and  $D_m(w_{IPA}=1)$  represent the molecular diffusion coefficient of (R,S)-MA in pure hexane and pure IPA, respectively, which can be computed from Hayduk-Laudie correlation[33]

$$D_m = \frac{13.25 \times 10^{-5}}{\mu^{1.4} V_a^{0.589}} \quad (3-12)$$

where  $\mu$  is the viscosity of solvent whose value is 0.29 cps for hexane and 1.96 cps for IPA. And based on the Le Bas additivity constants[34], the molar volume  $V_a$  can be estimated as 200 cm<sup>3</sup>/mol. So, the value of  $D_L$  is changed by the interstitial mobile phase velocity which is shown in Table 3-3.

**Table 3- 3: Axial dispersion coefficient values with different flow rates of mobile**

<b>phase</b>	
Flow rate (mL/min)	$D_L \times 10^{-3}(\text{cm}^2/\text{min})$
2	3.48
3	4.86
4	5.57

### 3.4.2.2 Parameter estimation and optimization

The isotherm parameters and the lumped rate coefficient  $k_v$  were derived from three overloaded band profiles with different amount of injections. To get the possible range of each decision variable, numerical simulations were performed initially. The isotherm parameters were then determined by minimizing the square difference between experimental and model predicated band profiles through optimization. The best-fit isotherm parameters for the competitive modified Langmuir isotherm models are listed in Table 3-4, respectively. Figure 3-6 illustrates the comparison of the three sets of experimental and simulated concentration profiles with competitive modified Langmuir isotherm. A good agreement between the measured and calculated band profiles can be seen from Figure 3-6.

**Table 3- 4: Competitive modified Langmuir isotherm parameters**

$k_v(s^{-1})$	$m_1$	$m_2$	$q_s(g/L)$	$b_1(L/g)$	$b_2(L/g)$
13.3	1.99	2.45	5.5	0.13	0.31

Note: Confidence interval of the data above at the confidence level = 95%

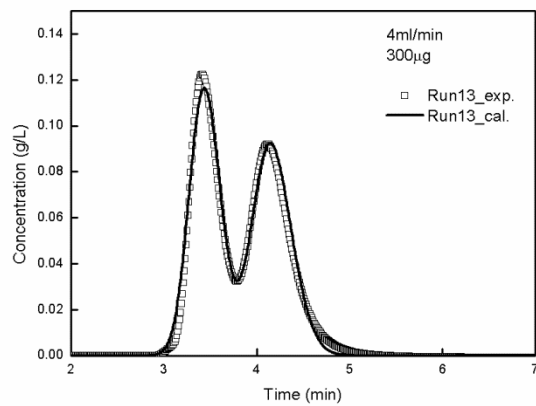
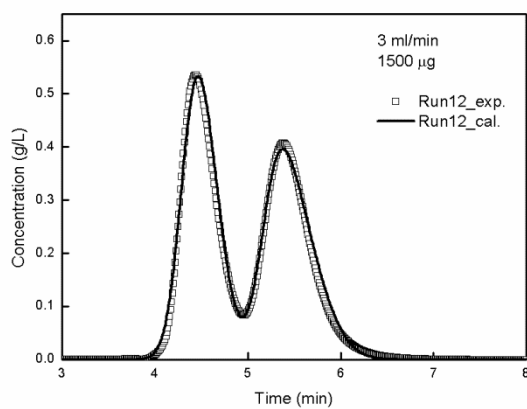
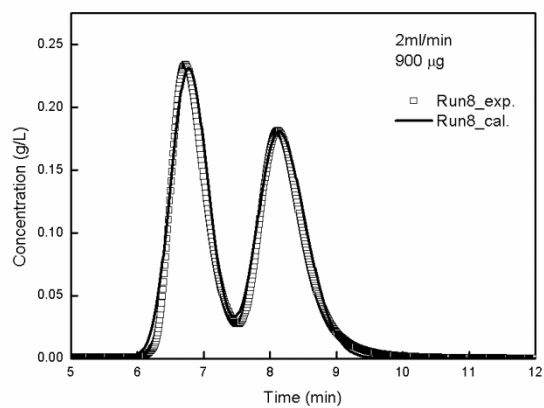


**Figure 3- 6: Best-fit of competitive modified Langmuir isotherm.**

To verify the accuracy and reliability of the derived isotherm parameters from inverse method, chromatographic experiments performed at higher (4mL/min), medium (3mL/min) and lower (2mL/min) elution flow rates with different injection amounts were used to examine the predicted elution profiles calculated from the best-fit isotherm parameters. Comparison of the measured and calculated band profiles at different elution flow rates are shown in Figures 3-7 to 3-9. All these comparisons demonstrate that the calculated and experimental elution profiles have a satisfying agreement. In addition, the adsorption isotherm obtained by frontal analysis was also used to verify the accuracy of the estimated isotherm parameters. The experiment data for the frontal analysis are shown in Table 3-5. Isotherm derived from inverse method has an acceptable agreement with that acquired from frontal analysis as shown in Figure 3-10. It shows that the inverse method is a reliable approach to estimate the parameters of adsorption isotherm and predict the elution profiles.



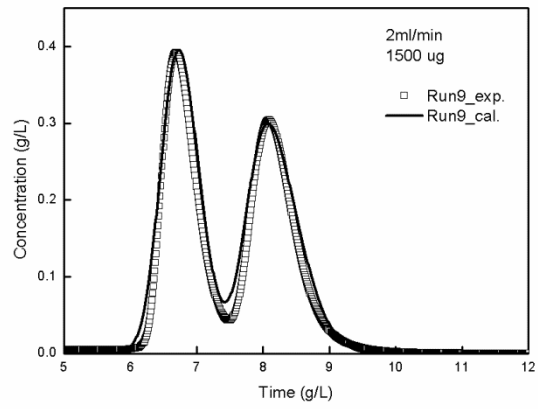
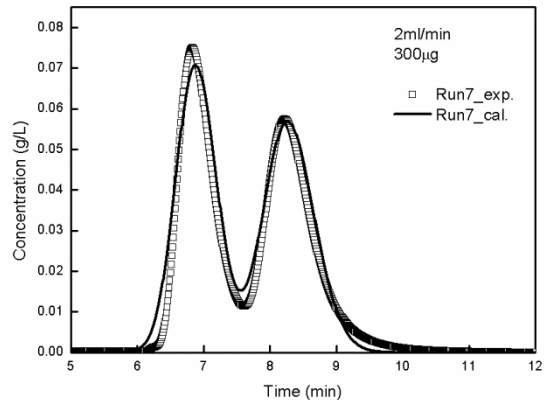


**Figure 3- 7: Verification of the best-fit isotherm parameters with lower elution flow rate.**

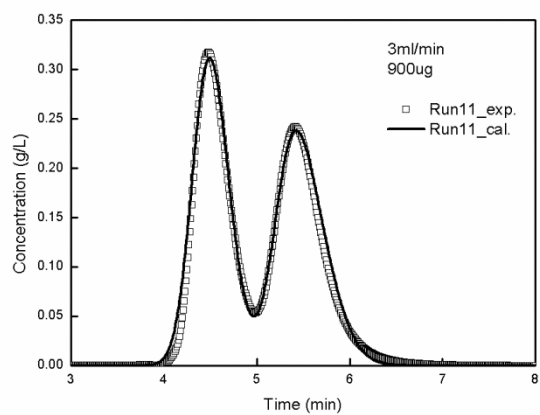
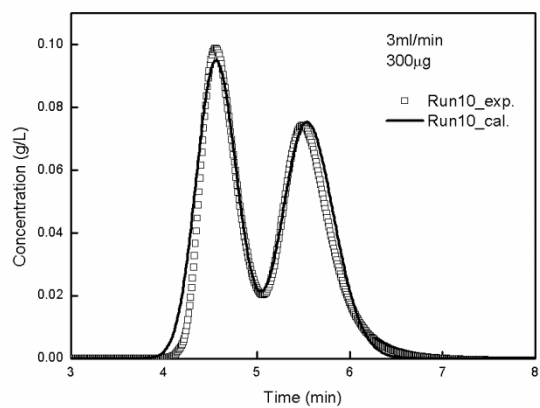


**Figure 3- 8: Verification of the best-fit isotherm parameters with medium elution flow rate.**

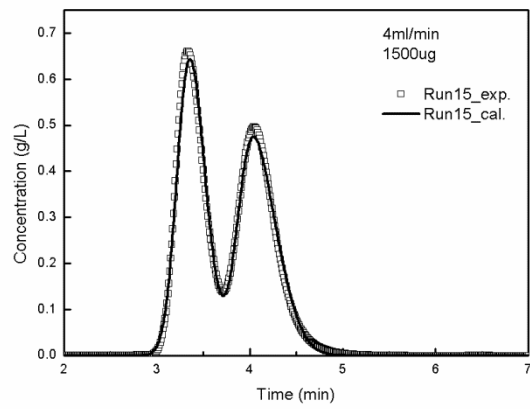
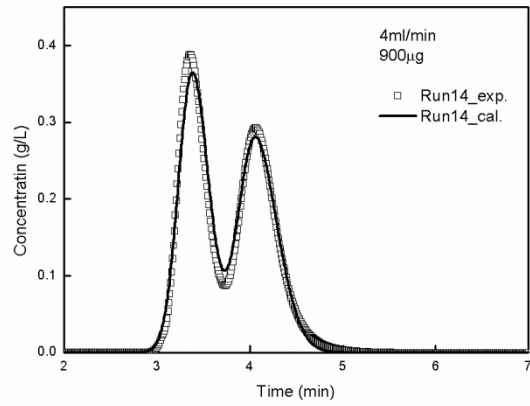


**Figure 3- 9: Verification of the best-fit isotherm parameters with higher elution flow rate.**

**Table 3- 5: The experimental data for frontal analysis**

$c_{F,1\_or\_c_{F,2}}$ (g/L)	$t_0$ (min)	$t_1$ (min)	$t_2$ (min)	$c_{m,1}$ (g/L)
0	0	0	0	0
0.13	2.13	4.63	5.64	0.11
0.33	2.13	4.57	5.61	0.35
0.66	2.13	4.43	5.46	0.69
0.98	2.13	4.39	5.42	1.03
1.31	2.13	4.25	5.25	1.33
3.28	2.13	4.24	4.98	3.30
6.55	2.13	4.09	4.73	6.75
9.83	2.13	4.08	4.56	11.80
13.10	2.13	3.98	4.42	14.73

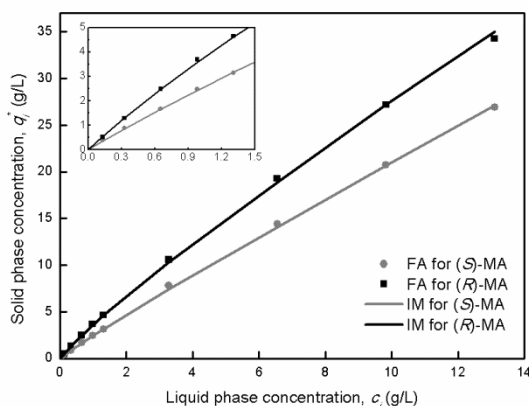


**Figure 3- 10: The competitive modifier Langmuir isotherm models for (R)- and (S)-MA obtained by frontal analysis and inverse method, where  $q_1=f(c_1, c_2=const)$  and  $q_2=f(c_1=const, c_2)$ .**

However, it still can be observed that there are small deviations between the calculated and experimental elution profiles from Figures 3-6 to 3-9. The main reason for the peak tailing comes from a heterogeneous thermodynamics. The strong and specific interactions taking place between solute molecules and certain regions of the surface of the packing materials could be the main origin of peak tailing, but this cannot be reflected precisely from the isotherm model.

### 3.5 Conclusions

Different mobile phases have been used to resolve (R,S)-MA on the cellulose tris(3,5-dimethylphenylcarbamate) chiral stationary phase. Results indicate that mobile phase consisting of hexane/IPA/TFA with 85/15/0.3 (v/v/v) gives the best resolution of (R,S)-MA. Both IPA and TFA concentrations in the mobile phase have great influence on the

retention and enantioseparation of (*R,S*)-MA. The retention time is decreasing with the increase of isopropanol content. And the higher TFA level in the mobile phase helps to reduce the peak broadening and decrease retention times of (*R*)- and (*S*)-MA.

Inverse method was used in this study to determine the competitive isotherm of (*R*)- and (*S*)-MA on the cellulose tris(3,5-dimethylphenylcarbamate) chiral stationary phase. By fitting three chromatograms simultaneously with different injection amounts and flow rates, the best-fit isotherm parameters for the competitive modified Langmuir were determined. Results suggest that competitive modified Langmuir isotherm gives better representation of the experimental data. Accuracy and reliability of the derived isotherm parameters were verified by comparing the model predicted band profiles with the experimental elution profiles under various experimental conditions. Results from the current study indicate the inverse method offers a rapid determination of competitive isotherm parameters of (*R,S*)-MA with minimal sample and solvent consumption and a satisfactory accuracy.

### 3.6 References

1. Felinger, A., A. Cavazzini, and G. Guiochon, *Numerical determination of the competitive isotherm of enantiomers*. Journal of Chromatography A, 2003. **986**(2): p. 207-225.
2. Felinger, A., D. Zhou, and G. Guiochon, *Determination of the single component and competitive adsorption isotherms of the 1-indanol enantiomers by the inverse method*. Journal of Chromatography A, 2003. **1005**(1-2): p. 35-49.
3. Guiochon, G., et al., *Fundamentals of preparative and nonlinear chromatography*. Vol. 2nd. 2006, Amsterdam: Elsevier Academic Press. 975.
4. Marchetti, N., et al., *Determination of adsorption isotherms by means of HPLC: Adsorption mechanism elucidation and separation optimization*. Journal Of Separation Science, 2009. **32**(5-6): p. 727-741.
5. Lisec, O., P. Hugo, and A. Seidel-Morgenstern, *Frontal analysis method to determine competitive adsorption isotherms*. Journal Of Chromatography A, 2001. **908**(1-2): p. 19-34.
6. Gritti, F. and G. Guiochon, *Influence of a buffered solution on the adsorption isotherm and overloaded band profiles of an ionizable compound*. Journal of Chromatography A, 2004. **1028**(2): p. 197-210.
7. Lindholm, J., P. Forssén, and T. Fornstedt, *Validation of the accuracy of the perturbation peak method for determination of single and binary adsorption isotherm parameters in LC*. Analytical Chemistry, 2004. **76**(16): p. 4856-4865.
8. James, F., et al., *Determination of binary competitive equilibrium isotherms from the individual chromatographic band profiles*. Chemical Engineering Science, 1999. **54**(11): p. 1677-1696.

9. Kaczmarski, K., *Estimation of adsorption isotherm parameters with inverse method-Possible problems*. Journal of Chromatography A, 2007. **1176**(1-2): p. 57-68.
10. Zhang, Y., K. Hidajat, and A.K. Ray, *Determination of competitive adsorption isotherm parameters of pindolol enantiomers on  $\alpha$ 1-acid glycoprotein chiral stationary phase*. Journal of Chromatography A, 2006. **1131**(1-2): p. 176-184.
11. Cornel, J., et al., *The direct inverse method: A novel approach to estimate adsorption isotherm parameters*. Journal of Chromatography A, 2010. **1217**(12): p. 1934-1941.
12. Vajda, P., A. Felinger, and A. Cavazzini, *Adsorption equilibria of proline in hydrophilic interaction chromatography*. Journal of Chromatography A, 2010. **1217**(38): p. 5965-5970.
13. Kaspereit, M., et al., *Impact of adsorption isotherm parameters on the performance of enantioseparation using simulated moving bed chromatography*. Journal of Chromatography A, 2002. **944**(1-2): p. 249-262.
14. Zhang, Y., S. Rohani, and A.K. Ray, *Numerical determination of competitive adsorption isotherm of mandelic acid enantiomers on cellulose-based chiral stationary phase*. Journal of Chromatography A, 2008. **1202**(1): p. 34-39.
15. Jacques, J., A. Collet, and S.H. Wilen, *Enantiomers, racemates, and resolutions*. 1981, New York ;; Toronto: Wiley. 447.
16. Lorenz, H., D. Sapoundjiev, and A. Seidel-Morgenstern, *Enantiomeric Mandelic Acid System-Melting Point Phase Diagram and Solubility in Water*. Journal of Chemical & Engineering Data, 2002. **47**(5): p. 1280-1284.
17. Zhang, Y., et al., *Nucleation and Growth Kinetics of (R)-Mandelic Acid from Aqueous Solution in the Presence of the Opposite Enantiomer*. Crystal Growth & Design, 2010. **10**(7): p. 2879-2887.



18. Ribeiro, A.E., et al., *Preparative separation of ketoprofen enantiomers: Choice of mobile phase composition and measurement of competitive adsorption isotherms*. Separation and Purification Technology, 2008. **61**(3): p. 375-383.
19. Arnell, R., P. Forssén, and T. Fornstedt, *Tuneable peak deformations in chiral liquid chromatography*. Analytical Chemistry, 2007. **79**(15): p. 5838-5847.
20. Arnell, R., et al., *Adsorption behaviour of a quinidine carbamate-based chiral stationary phase: Role of the additive*. Journal Of Chromatography A, 2009. **1216**(16): p. 3480-3487.
21. Forssén, P., et al., *Effects of a strongly adsorbed additive on process performance in chiral preparative chromatography*. Journal Of Chromatography A, 2008. **1212**(1-2): p. 89-97.
22. Ruthven, D.M., *Principles of adsorption and adsorption processes*. 1984, New York; Toronto: Wiley. 433.
23. Kasat, R.B. and S.K. Gupta, *Multi-objective optimization of an industrial fluidized-bed catalytic cracking unit (FCCU) using genetic algorithm (GA) with the jumping genes operator*. Computers and Chemical Engineering, 2003. **27**(12): p. 1785-1800.
24. Jacobson, J.M., J.H. Frenz, and C.G. Horvath, *Measurement of competitive adsorption isotherms by frontal chromatography*. Industrial & Engineering Chemistry Research, 1987. **26**(1): p. 43-50.
25. Kirkland, K., *Optimization of chiral selectivity on cellulose-based high-performance liquid chromatographic columns using aprotic mobile-phase modifiers*. Journal Of Chromatography A, 1995. **718**(1): p. 9-26.
26. Dossou, K.S.S., et al., *Enantioresolution of basic pharmaceuticals using cellulose tris (4-chloro-3-methylphenylcarbamate) as chiral stationary phase and polar organic mobile phases*. Journal Of Chromatography A, 2009. **1216**(44): p. 7450-7455.

27. Ribeiro, A.E., et al., *Optimization of the mobile phase composition for preparative chiral separation of flurbiprofen enantiomers*. Separation and Purification Technology, 2009. **68**(1): p. 9-23.
28. Zabkova, M., M. Zabka, and A.E. Rodrigues, *Separation of Racemic Chiral Drugs Using Immobilized CHIRALPAK IA: Methodology for Preparative Scale Development*. Separation Science And Technology, 2009. **44**(2): p. 275-303.
29. Miller, L., et al., *Preparative chromatographic resolution of enantiomers using polar organic solvents with polysaccharide chiral stationary phases*. Journal of Chromatography A, 1999. **865**(1-2): p. 211-226.
30. Ye, Y.K. and R.W. Stringham, *Effect of mobile phase acidic additives on enantioselectivity for phenylalanine analogs*. Journal Of Chromatography A, 2001. **927**(1-2): p. 47-52.
31. Putnam, J. and G. Guiochon, *Characterizing the Memory Effect on the amylose tris (3, 5-dimethylphenyl) carbamate stationary phase*. Journal Of Chromatography A, 2009. **1216**(48): p. 8488-8495.
32. Cussler, E.L., *Diffusion: Mass transfer in fluid systems*. 1997: Cambridge Univ Pr.
33. Hayduk, W. and H. Laudie, *Prediction of diffusion coefficients for nonelectrolytes in dilute aqueous solutions*. AIChE Journal, 1974. **20**(3): p. 611-615.
34. Baum, E.J., *Chemical property estimation: theory and application*. 1998: CRC.

## **Chapter 4**

### **Enantioseparation of Racemic Mandelic Acid by Simulated Moving Bed Chromatography Using Chiralcel OD Column**

A version of this chapter was published as:

Mao, S.; Zhang, Y; Rohani, S.; Ray, A.K. Enantioseparation of Racemic Mandelic Acid by Simulated Moving Bed Chromatography Using Chiralcel OD Column, submitted to Separation and Purification Technology.

## 4.1 Introduction

The enantioseparation of chiral compounds continues to be of great interest due to their prevalence in the pharmaceuticals, agrochemicals, and food additives [1-3]. It is well recognized that enantiomers often exhibit different biological and pharmacological responses. Chiral separation remains challenging due to the identical physical and chemical properties of enantiomers in an achiral environment, and research on specialized separation techniques continues to be developed to resolve individual enantiomers [4-7].

Direct resolution of enantiomers by high performance liquid chromatography has become the most popular and highly applicable technology due to the concomitant development of chiral stationary phases and efficient chromatographic techniques [8-12]. SMB technology, a continuous chromatographic technique, first developed by Broughton and Gerhold [13] has been proven efficient in resolution various enantiomers from their racemates and has been successfully applied to industrial-scale enantioseparations [14-17]. As an implement of continuous countercurrent chromatographic process, SMB unit as illustrated in Figure 4-1 is composed of several fixed-bed columns separated into four sections by valves and ports which can be switched periodically in the direction of the mobile phase to simulate the countercurrent movement. The separation takes place in sections 2 and 3. Sections 1 and 4 are functioned for the solid and solvent regenerations, respectively. The desired separation performance of binary mixtures can be reached by tuning the flow rate of mobile phase in each section and the switching time. Compared to the batch chromatography, SMB allows the maximization of the mass transfer driving

force which leads to less chiral stationary phase requirements and solvent consumptions as well as high efficiency. Moreover, the fixed-bed columns overcome the movement and erosion of the solid phase in the true moving bed process.

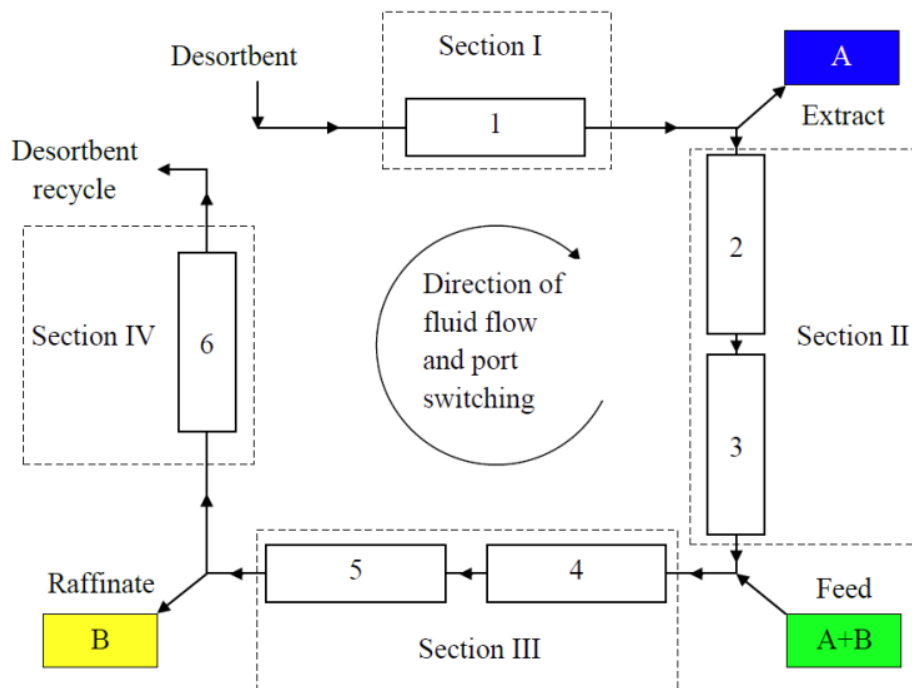


**Figure 4- 1: Schematic diagram of an open loop four section SMB unit.**

During the last decades, a large number of chiral stationary phases (CSPs) have been developed to achieve chiral separation of a wide variety of racemic compounds [16, 18-20]. Among more than one hundred commercially available CSPs, those based on the phenylcarbamates of polysaccharides including cellulose and amylose have been recognized as the most powerful for the resolution of a wide range of racemates, and nearly 90% of chiral compounds can be resolved at the analytical level using the polysaccharide-based CSPs [21].

In this study we have theoretically and experimentally investigated the preparative enantioseparation of racemic mandelic acid, (*R,S*)-MA, on the cellulose tris(3,5-dimethylphenylcarbamate) chiral stationary phase (Chiralcel OD column) by SMB chromatography. The goal of this study is to apply the triangle theory to the design and complete separation of (*R*)- and (*S*)-MA by SMB chromatography and then discuss the effects of switching time, feed concentration and column configuration on the separation performance.

## 4.2 Theoretical background

### 4.2.1 Isotherm model

Polysaccharide chiral stationary phases usually offer many interacting sites where pairs of enantiomers are discriminated. Therefore, isotherm models based on homogeneous surfaces are invalid for the resolution of enantiomers on this type of chiral stationary phases. In this study a competitive modified Langmuir isotherm model which assumes two different types of binding sites with either one being homogeneous on the surface of the stationary phase has been used to describe the phase equilibrium of (*R*)- and (*S*)-MA on the cellulose tris(3,5-dimethylphenylcarbamate) chiral stationary phase. Competitive modified Langmuir isotherm model is written as:

$$q_i^* = H_i c_i + \frac{q_s b_i c_i}{1 + \sum_{i=1}^2 b_i c_i} \quad (4-1)$$

where  $q_i^*$  is the adsorbed amount of component  $i$  in the stationary phase equilibrated with the mobile phase at the concentration  $c_i$ .  $H_i$  is the coefficient for the non-specific

adsorption sites. And  $q_s$  and  $b_i$  are the saturation capacities and the equilibrium constants for component  $i$  ( $i=A$  or  $B$ ), respectively. The components A and B represent the more retained component (( $R$ )-MA) and less retained component (( $S$ )-MA), respectively.

## **4.3 SMB model**

### **4.3.1 SMB modeling**

The column model, mass balance of nodes and the SMB performance equations constitute the mathematical model of SMB process. That is essential to the successful design and operation of SMB chromatography. In addition, the adsorption isotherm in the SMB shows the competitive behaviour since the SMB runs under overload operating conditions, which must be taken into account of the SMB design.

The column model was used to describe the migration of the mixture components concentration along the columns of a SMB system. The transport dispersive (TD) model assumes that the kinetics of adsorption–desorption is infinitely fast but not for the mass transfer kinetics [22-24]. The solid film linear driving force (LDF) model, which decouples the effect of finite mass transfer and axial dispersion, provides sufficient accuracy in modeling various chromatographic processes. The LDF model is based on the assumptions that the adsorbent particles are homogeneous; the flow in the column is characterized by a convective and a dispersive term, and a linear driving force for the mass transfer of the solute from fluid phase to the surface of the adsorbents. The LDF model is also capable to handle any kind of adsorption equilibrium isotherm. In the current study, TD model with the solid film linear driving force is used for the SMB

column model. The model equations as well as the initial and boundary conditions of each column in a SMB system are listed in Table 4-1.

**Table 4- 1: Transient model equations for SMB chromatography**

---

**Mass balance equations for component  $i$  in column  $j$**

$$\frac{\partial c_{ij}^N}{\partial t} + \frac{1-\varepsilon}{\varepsilon} \cdot \frac{\partial q_{ij}^N}{\partial t} + u_j \cdot \frac{\partial c_{ij}^N}{\partial z} = D_L \cdot \frac{\partial^2 c_{ij}^N}{\partial z^2}$$

**Lumped kinetic models**

$$\frac{\partial q_{ij}^N}{\partial t} = k_v(q_{ij}^{N*} - q_{ij}^N)$$

**Initial conditions**

When  $N = 0$ ,  $c_{ij}^0 = 0$  and  $q_{ij}^0 = 0$

When  $N \geq 1$ ,  $c_{ij}^N = c_{i,j+1}^{N-1}$  for  $j = 1 \sim (N_T - 1)$  and  $c_{ij}^N = c_{i,1}^{N-1}$  for  $j = N_T$

**Boundary conditions**

$$c_{i,1}^N \Big|_{z=0} = \frac{Q_4}{Q_1} c_{i,N_T}^{N-1} \Big|_{z=L} \text{ for eluent node}$$

$$c_{i,N_1+1}^N \Big|_{z=0} = c_{i,N_1}^N \Big|_{z=L} \text{ for extract node}$$

$$c_{i,N_1+N_2+1}^N \Big|_{z=0} = \frac{Q_2}{Q_3} c_{i,N_1+N_2}^N \Big|_{z=L} + \frac{Q_F}{Q_3} c_{F,i} \text{ for feed node}$$

$$c_{i,N_1+N_2+N_3+1}^N \Big|_{z=0} = c_{i,N_1+N_2+N_3}^N \Big|_{z=L} \text{ for raffinate node}$$


---

**4.3.1.1 SMB performance parameters**

Purities and recoveries of the two components in extract and raffinate streams were used to evaluate the performance of SMB process. The purities of raffinate and extract



streams,  $Pu_{Ra}$  and  $Pu_{Ex}$  and the recovery of the two enantiomers are defined as below for SMB operation.

$$Pu_{Ra} = \int_t^{t+t^*} \frac{c_{B,Ra}}{c_{A,Ra} + c_{B,Ra}} dt \quad (4-2)$$

$$Pu_{Ex} = \int_t^{t+t^*} \frac{c_{A,Ex}}{c_{A,Ex} + c_{B,Ex}} dt \quad (4-3)$$

$$Re_B = \frac{Q_{Ra}}{Q_F} \int_t^{t+t^*} \frac{c_{B,Ra}}{c_{B,F}} dt \quad (4-4)$$

$$Re_A = \frac{Q_{Ex}}{Q_F} \int_t^{t+t^*} \frac{c_{A,Ex}}{c_{A,F}} dt \quad (4-5)$$

### 4.3.2 Design of SMB

The prerequisite for the successful separation by SMB is choosing the operating conditions. Those conditions can be determined by the flow rate ratio between the net mobile and solid phase mass flow in each section,  $m_g$ , which are vital parameters to control the SMB performance.

$$m_g = \frac{Q_g t^* - V \varepsilon - V_g^D}{V(1-\varepsilon)} \quad (g = 1, \dots, 4) \quad (4-6)$$

$$\varepsilon = \frac{t_0 Q_j - V^D}{V} \quad (4-7)$$

According to the triangle theory, if complete regeneration of the adsorbent and desorbent is confirmed, a specific plane formed by  $m_2$  and  $m_3$  values, which are independent of  $m_1$  and  $m_4$  values, can be applied to determine the binary separation performance of a SMB unit. As demonstrated in Figure 4-2, a total of four regions, i.e.

the complete separation region, pure extract region, pure raffinate region and no pure outlet region, can be found in the  $(m_2, m_3)$  plane corresponding to different operating regimes. Certainly, the determination of the complete separation region in the  $(m_2, m_3)$  plane is of paramount importance. However, for nonlinear system in the presence of mass transfer resistance, determination of the complete separation region is not straightforward. Numerical simulation has to be applied to determine the boundaries of complete separation region because none of constraints for  $m_g$  values are explicit.

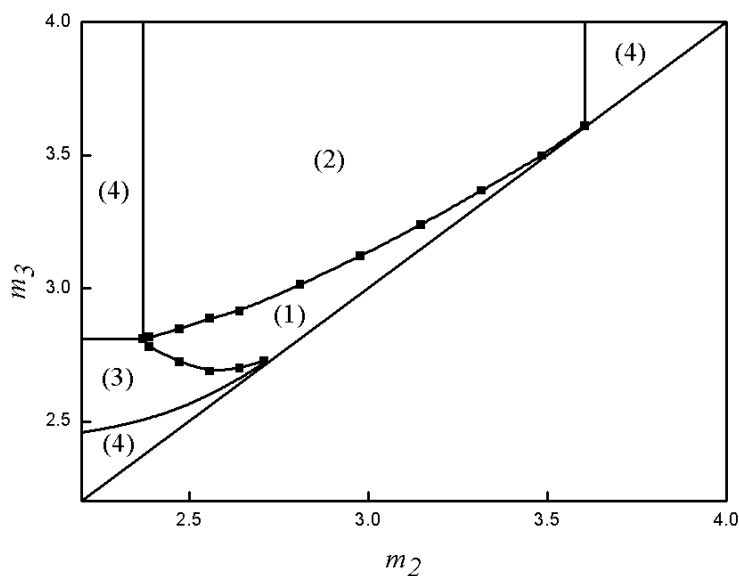


**Figure 4- 2: Separation of (R,S)-MA racemic compound using Chiralcel OD SMB system. Regions of ( $m_2$ ,  $m_3$ ) plane based on the purity of both outlet stream over 99% when the feed concentration is 30g/L and column configuration is 1/2/2/1. The numbers with the parenthesis in areas present the four different separation regions: (1) pure raffinate and extract; (2) only pure extract; (3) only pure raffinate; (4) no pure raffinate and extract.**

In this study, a simplified design method has been applied to obtain the complete separation region of (R,S)-MA using our laboratory SMB setup. Firstly, the explicit constraints of  $m_1$  and  $m_4$  for the complete regeneration of adsorbent and desorbent in sections 1 and 4 were obtained using the approach proposed by Susanto *et al.* [25] as given below:

$$m_1 > \left. \frac{dq_A}{dc_A} \right|_{c_A \rightarrow 0, c_B = 0} \quad (4-8)$$

$$m_4 < \left. \frac{q_B}{c_B} \right|_{c_A = 0, c_B = c_F} \quad (4-9)$$

These simplified constraints of  $m_1$  and  $m_4$  was proposed based on the analyses of the propagations of shock fronts and desorption fronts in various SMB systems and have been proved to be accurate when mass transfer between the fluid phase to the surface of the adsorbents in the TD model is fast [26].

The estimation of the flow rate in section 1,  $Q_1$ , is based on the limitations of the press drop of the SMB system and the pump performance since it is the highest flow rate in the unit. Coupling  $Q_1$  with  $m_1$ , the switching time can be determined by

$$t^* = \frac{V[(m_1(1-\varepsilon)+\varepsilon)]+V_1^D}{Q_1} \quad (4-10)$$

The flow rate in section 4,  $Q_4$  can then be determined directly by applying the constraint of  $m_4$  in Eq. (4-9). But the boundaries for complete separation region in the  $(m_2, m_3)$  plane has to be determined by numerical simulation. Once the complete separation in the  $(m_2, m_3)$  plane was obtained, operating parameters ( $Q_2$  and  $Q_3$ ) derived from any combination of  $m_2$  and  $m_3$  within the complete separation region could be selected for the SMB operation to achieve the complete separation of (R)- and (S)-MA.

## 4.4 Experiment setting

### 4.4.1 Materials and equipments

The 99% (*R,S*)-MA (Alfa Aesar, MA, USA) was isolated by the Chiralcel OD column (Chiral Technologies, PA, USA) which was packed with cellulose tris(3,5-dimethylphenyl carbamate) coated on 20  $\mu\text{m}$  silica-gel substrate with a length of 100mm, and a diameter of 10mm. The 99% (*R*)- and (*S*)-MA (Alfa Aesar, MA, USA) were used for calibration. The mixture of hexane, isopropanol (IPA) (85:15,v/v) (Calendon, Gergetown, ON, CA) and 0.3v% trifluoroacetic acid (Alfa Aesar, MA, USA) was used as the mobile phase. It is noted that all mobile phased used in this study is same and the solvents used in this study were all HPLC grade. The column void fraction,  $\epsilon$ , was determined by injecting 1,3,5-tri-tert-butylbenzene (TTB) (TCI American, Portland, USA) on each column and using Eq. (4-7), which is shown in Table 4-2. The value of average column void fraction is 0.698 which was used in the SMB simulation.

**Table 4- 2: The void fraction of each column in SMB unit**

Column	1	2	3	4	5	6	Average
$\epsilon$	0.708	0.697	0.699	0.699	0.693	0.694	0.698

The final products were analyzed on an analytical Chiralcel OD-H (Chiral Technologies, PA, USA) column (4.6mm $\times$ 250mm, 5 $\mu\text{m}$ ) and an Agilent 1200 series liquid chromatography system (Agilent Technologies, CA, USA), equipped with a vacuum degasser, a quaternary pump, an auto injector with a 100 $\mu\text{L}$  sample loop, a thermostatted column compartment, a diode array, multiple wave length UV detector and

the Agilent chemstation software. The UV detector was set at 254nm and the flow rate of the mobile phase was 0.5mL/min under the column temperature 23°C.

#### **4.4.2 SMB operation**

A SMB unit is composed of six semi-preparative Chiralcel OD columns arranged in a 1-2-2-1 configuration. Five 8-port multi-position valves (Vici-Valco, TX, USA) are applied for port switching to achieve the continuous movement of the solid phase, which is in the opposite direction of mobile phase flow. The check valves located at the inlet of each column are used to enforce the fluid direction. The two inlet streams, feed and desorbent flows, are delivered by two Jasco PU-2080 pumps (Jasco, Tokyo, JP), coupled with the online vacuum degasser (Agilent Technologies, CA, USA). And the two outlet streams, raffinate and extract flows are controlled by two mass flow controllers (Brooks Instrument, PA, USA). The flow rate of effluent leaving from the section 4 is determined by the overall mass balance. Since open loop operation of SMB unit is adopted, the outlet stream from the section 4 is collected in a glass container and recycled offline.

Before the SMB separation experiments were performed, the unit was firstly flushed with mobile phase for 3 hours under the selected operating conditions until the flow rates of the inlet and outlet streams were constant. Then feed was continuously injected into the system. The products of each cycle were collected from the raffinate and extract port separately. After 15 cycles, the SMB system reached the steady state. After the SMB experiment, each column in the system was washed by anhydrous ethyl alcohol (Et-OH) (Greenfield, ON, CA) for 3 hours with 1.25mL/min flow rate and then flushed with hexane and IPA(90/10,v/v) for storage.

## 4.5 Results and discussion

### 4.5.1 Isotherm parameters and rate coefficients

Acute equilibrium data is one of the most important keys to predict the overall SMB performance for chiral separation. Competitive isotherm parameters plus the rate coefficients used in the SMB simulation have been determined from the single column experiments presented elsewhere [27]. In addition, the apparent axial dispersion coefficient in each section of the SMB unit has been corrected with the real flow rate in that section based on the value obtained from the single column experiments. The isotherm and model parameters for the design and simulation of chiral separation of (*R,S*)-MA in the SMB chromatography were given in Table 4-3.

**Table 4- 3: Isotherm parameters and rate coefficients of (*R*)- and (*S*)-MA in SMB**

column				
Competitive isotherm parameters				
$H_A$	$H_B$	$q_s$ (g/L)	$b_A$ (L/g)	$b_B$ (L/g)
2.45	1.99	5.5	0.31	0.13
Model parameters				
$k_v$ ( $s^{-1}$ )	$D_L$ ( $\times 10^{-3} \text{cm}^2/\text{min}$ ) at $Q = 4.0 \text{ mL}/\text{min}$			
13.3	5.57			

### **4.5.2 Complete separation region**

Based on the design strategy described in section 2.3, complete separation of (*R*)- and (*S*)-MA in the SMB unit requires  $m_1$  value to be higher than 4.36 while  $m_4$  value to be lower than 2.26. The total dead volume of the SMB unit was measured to be 0.95 mL. The other operating conditions, i.e. switching time ( $t^*$ ), the flow rate in section 2, 3 and 4 ( $Q_2$ ,  $Q_3$ ,  $Q_4$ ) can be estimated based on the purity criteria. The operating conditions are listed in Table 4-4. The complete separation region for the (*R,S*)-MA, with a feed concentration of 30g/L was obtained when the purities of extract and raffinate outlet stream were over 99%, which is shown in Figure 4-2.

### **4.5.3 The effects of operating conditions on SMB performance**

In this section, the influences of the operating conditions on SMB performance are discussed. The operating conditions are listed in Table 4-4 and the SMB performance are shown in Table 4-5.



**Table 4- 4: Operation conditions and parameters for the SMB experiments**

Run	Operation conditions						Operation parameters			
	$c_{feed}$ (g/L)	Flow rate (mL/min)				$t^*$ (min)	Flow rate ratio			
		$Q_1$	$Q_2$	$Q_3$	$Q_4$		$m_1$	$m_2$	$m_3$	$m_4$
1	30	6	4	4.02	2.32	3.0	5.21	2.68	2.71	0.56
2	30	6	4	4.02	2.32	3.2	5.72	3.02	3.05	0.75
3	30	6	4	4.02	2.32	3.7	6.98	3.86	3.89	1.24
4	30	6	4	4.02	2.32	3.5	6.48	3.52	3.55	1.05
5	30	6	4	4.03	2.32	3.5	6.48	3.52	3.57	1.05
6	30	6	4	4.05	2.32	3.5	6.48	3.52	3.60	1.05
7	30	6	4	4.2	2.5	3.5	6.48	3.52	3.82	1.31
8	20	6	4	4.2	2.5	3.5	6.48	3.52	3.82	1.31
9	10	6	4	4.2	2.5	3.5	6.48	3.52	3.82	1.31
10	1	6	4	4.2	2.5	3.5	6.48	3.52	3.82	1.31
11	30	6	4.1	4.12	2.32	3.5	6.48	3.67	3.70	1.05
12	30	6	3.8	3.82	2.32	3.5	6.48	3.23	3.26	1.05
13*	1	6	4	4.2	2.5	3.5	6.48	3.52	3.82	1.31

\* The column configuration of Run 13 is 1/1/1/1.

**Table 4- 5: Separation performance of experiments on SMB**

%	Run												
	1	2	3	4	5	6	7	8	9	10	11	12	13
$Pu_{Ex}$	97.60	99.04	88.98	99.15	99.19	99.22	98.62	99.33	100	99.8	98.86	99.1	95.99
$Pu_{Ra}$	99.69	99.64	51.28	81.47	71.33	60.07	51.82	52.21	56.93	91.68	70.47	99.75	82.13
$Re_A$	92.27	89.13	5.67	77.4	60	33.71	7.12	11.83	24.16	90.94	55.42	97.17	78.8
$Re_B$	90.10	93.27	99.3	99.33	99.51	99.73	99.9	91.29	96.78	99.82	99.36	98.3	96.6

**4.5.3.1 Switching time,  $t^*$** 

Runs 1 to 4 were carried out by varying different switching time while keeping the flow rate and feed concentration constant as list in Table 4-4.

As shown in Figure 4-3a, the raffinate purity decreases from 99.69% to 51.58% with the switching time increasing from 3 to 3.7 min, while the extract purity increases from 97.60% to 99.15% initially but then decreases to 88.98% when the switching time increasing from 3.5 to 3.7 min. The increase of the switching time causes the values of  $m_2$  and  $m_3$  increasing. Along the diagonal line on the plane  $(m_2, m_3)$ , the operating points move from the left side of complete separation region where only the pure raffinate stream can be obtained, go through the complete separation region where both outlet streams are pure and reach the right side of triangle where both outlet streams are polluted. The changes of the purities of raffinate and extract streams are confirmed in Figure 4-3a. Moreover, the increasing switching time which leads to a relative high fluid to solid flow rate ratio, makes the more amount of the (S)-MA and (R)-MA elute with

mobile phase from the raffinate stream. This is why the recovery of (*S*)-MA in raffinate stream grows from 90.1% to 99.3% whereas the recovery of (*R*)-MA in extract stream declines from 92.27% to 5.67% as illustrated in Figure 4-3b.

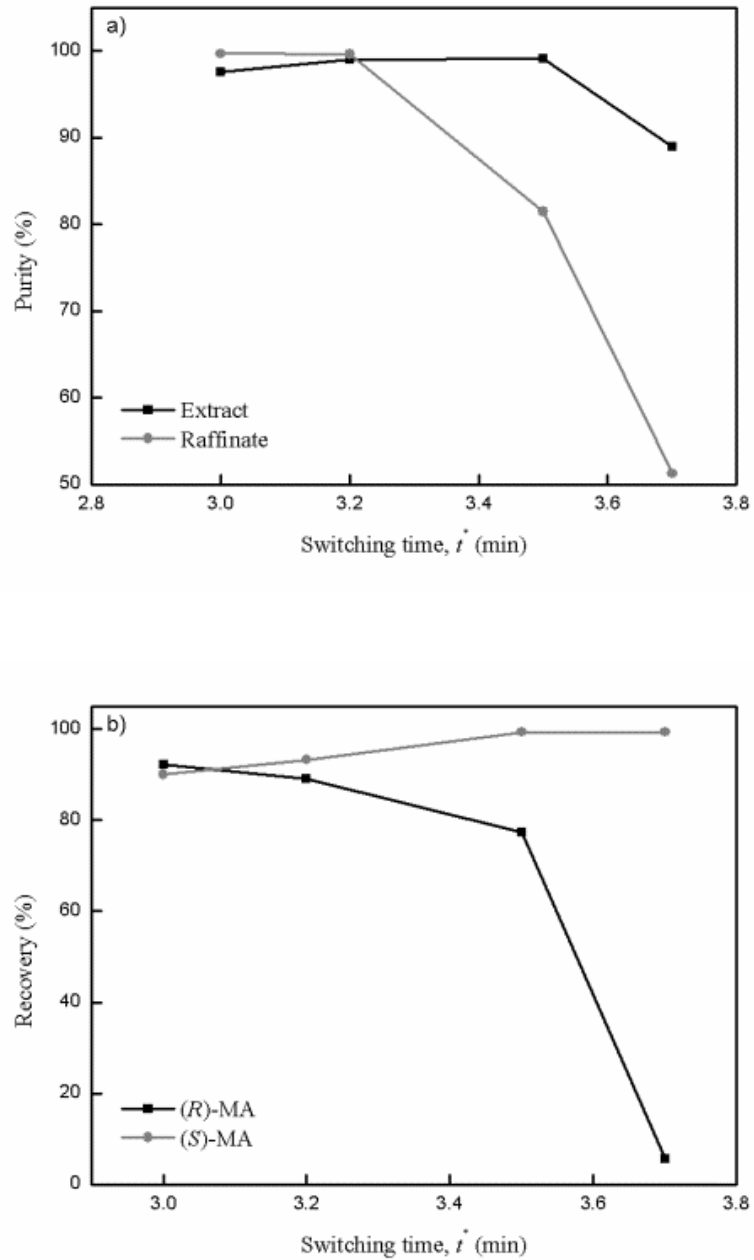


**Figure 4- 3: SMB performance as a function of switching time.**

#### 4.5.3.2 Feed concentration and flow rate, $c_f$ and $Q_f$

The SMB performance can be affected by the loading change in the SMB system which can be achieved by varying the feed concentration or flow rate. Runs 4 to 10 were carried out for those purposes.

It can be observed in the Figure 4-4a the extract purity decreases slightly from around 100% to 98.62%, whereas, the raffinate purity drops quickly from 91.68% to 51.82% with the feed concentration rising from 1g/L to 30g/L. The capacity of the adsorption sites on the solid phase remains constant with the same mobile phase. With the feed concentration increasing, the migration of concentration fronts of (*R*)-MA and (*S*)-MA becomes faster within the SMB system, as a result, certain amount of (*R*)-MA also elutes from the raffinate stream along with (*S*)-MA, which leads to a significant decline of the raffinate purity. The extract recovery as shown in Figure 4-4b also decreases from 90.94% to 7.12% due to the considerable loss of (*R*)-MA in the extract stream.

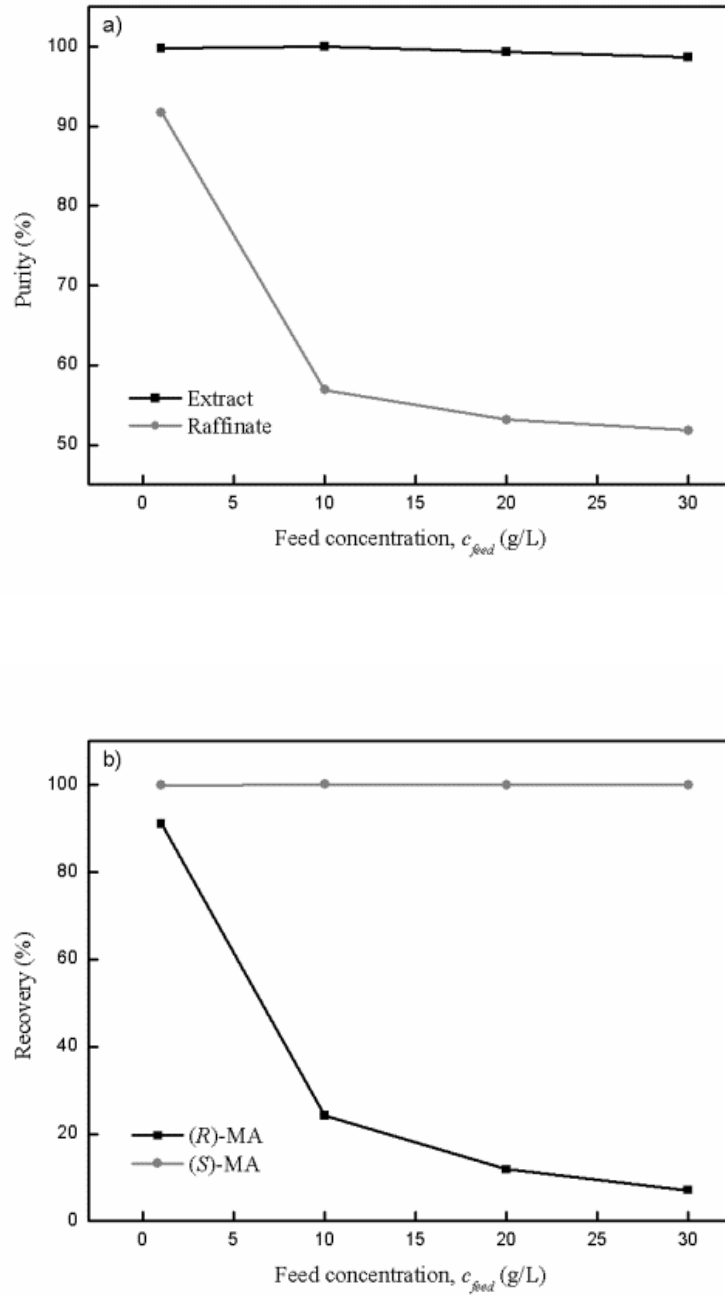


**Figure 4- 4: SMB performance as a function of feed concentration.**

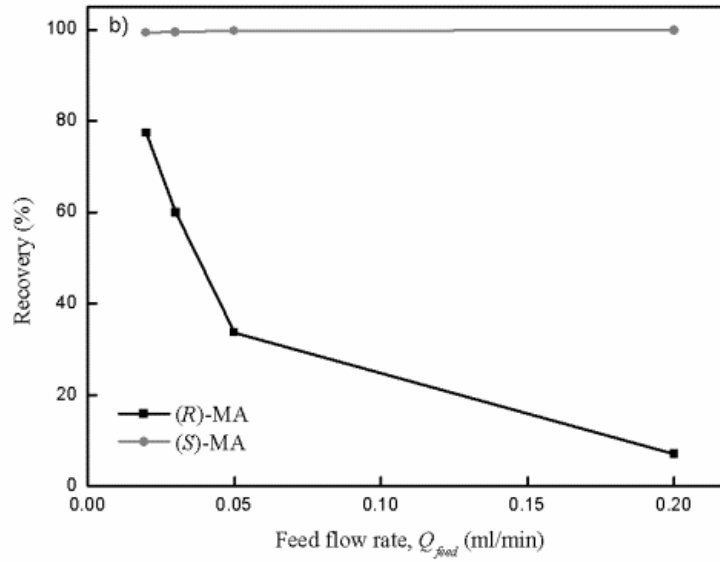
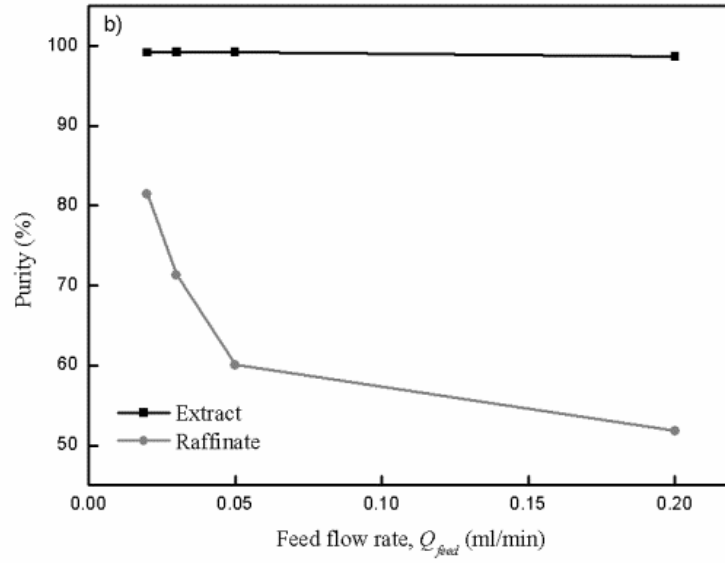


**Figure 4- 5: SMB performance as a function of feed flow rate.**

Increasing the feed flow rate causes the values of  $m_3$  increasing. The operating points on the plane  $(m_2, m_3)$  move from the complete separation region to the pure extract region or even the no pure outlet region. Similarly, the increased  $m_3$  value makes the more amount of (*S*)-MA and (*R*)-MA elute with mobile phase from raffinate stream. This can be verified from Figure 4-5 that the purity of extract stream is almost same while the purity of raffinate stream and the recovery of (*R*)-MA decrease remarkably.

#### **4.5.3.3 Extract flow rate, $Q_{ex}$**

Effect of the extract flow rate on the SMB performance was studied by keeping the feed flow rate, the flow rate of section 1 and 4 and the feed concentration constant as Runs 4, 11 and 12 shown in Table 4-4.

Figure 4-6 illustrates that the raffinate purity increases from 70.47% to 99.75% and the extract purity ascends from 98.86% to around 99.10% when the extract flow rate rises from 1.9 mL/min to 2.2 mL/min. The reason is that the increased extract flow rate leads to the decrease of flow rates in section 2 and 3, hence lower  $m_2$  and  $m_3$  values. As a result, with the increase of the extract flow rate, the operating points on the  $(m_2, m_3)$  plane move downward from the pure extract region to complete separation and finally reach the pure raffinate region or no pure outlet region.

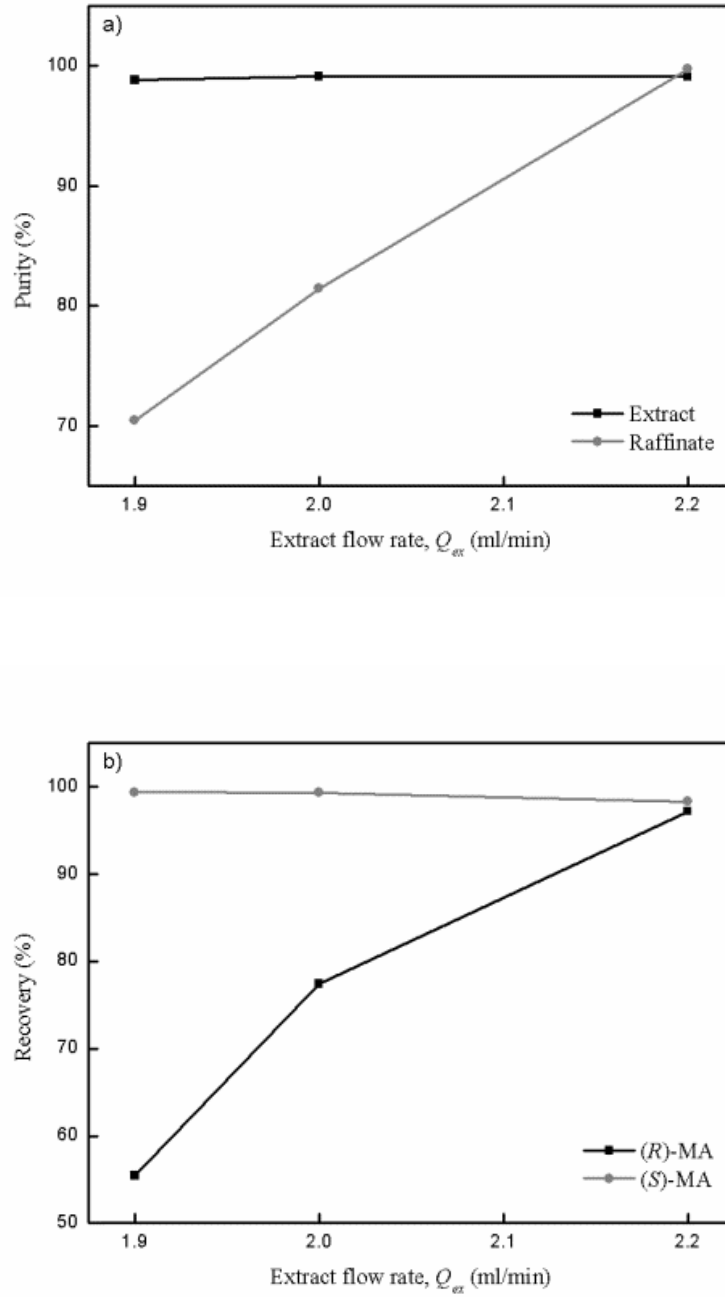
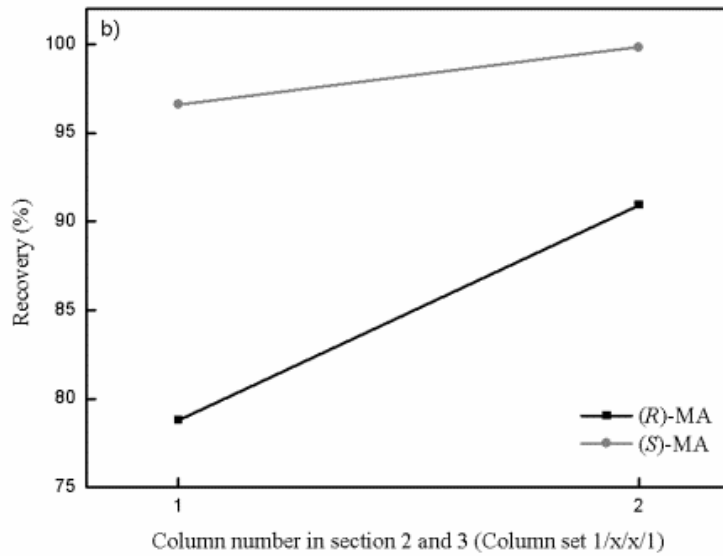
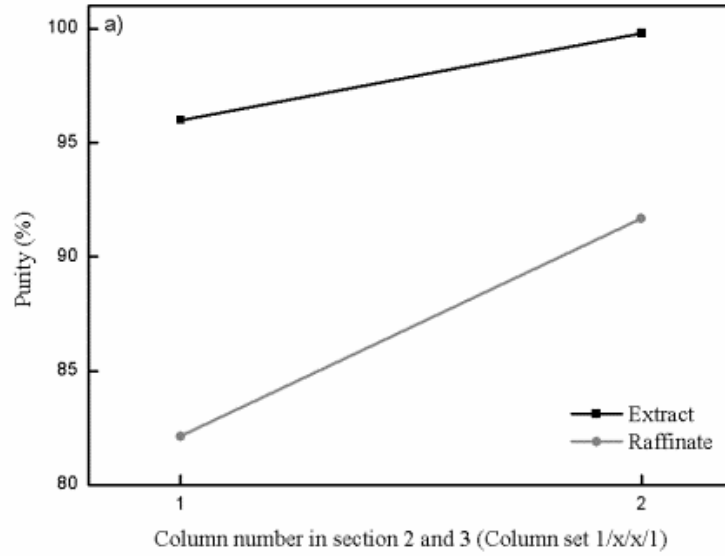


Figure 4- 6: SMB performance as a function of extract flow rate.



#### **4.5.3.4 Column configuration**

The SMB performance for the column configuration 1/1/1/1 of Run 13 and 1/2/2/1 of Run 14 are compared in Figure 4-7. With one more column being used in the two separation sections, the number of the theoretical plates in sections 2 and 3 doubled. Consequently, as illustrated in Figure 4-7, the purities and the recoveries of the raffinate and extract streams are both increased due to the enhanced separation power of the SMB system.



**Figure 4- 7: SMB performance as the column configuration.**

#### **4.5.4 Validation of the SMB model with the experimental data**

The experimental data of the purities and recoveries of the extract and raffinate streams obtained from different operating conditions were used to be compared with those calculated from the simulation. Here, take the data from Runs 2, 6 and 12 as examples. A good agreement between the experimental and simulated data in Figures 4-8 to 4-10 implies that this model with those parameters can reflect the separation process in the SMB properly. Although small deviations between the experimental data and model predictions caused either by numerical errors or the fluctuation of the flow rates of the outlet streams on the SMB experiments are observed from Figures 4-8 to 4-10, model predictions in this study can be considered with satisfactory accuracy in predicting the SMB performance.

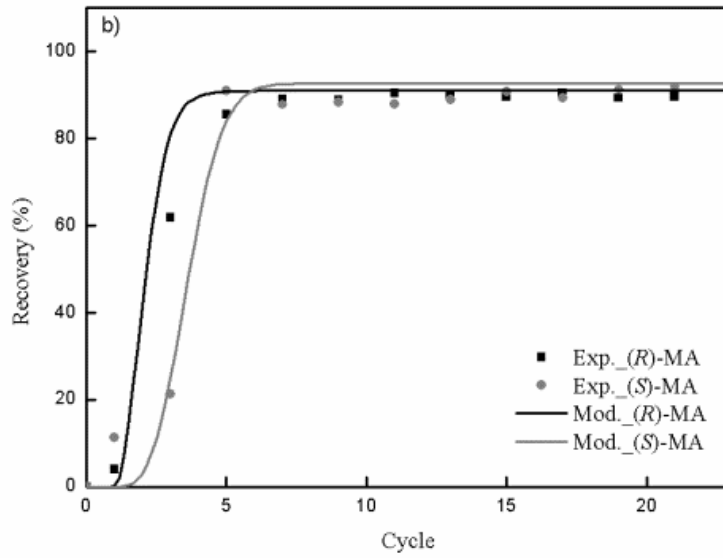
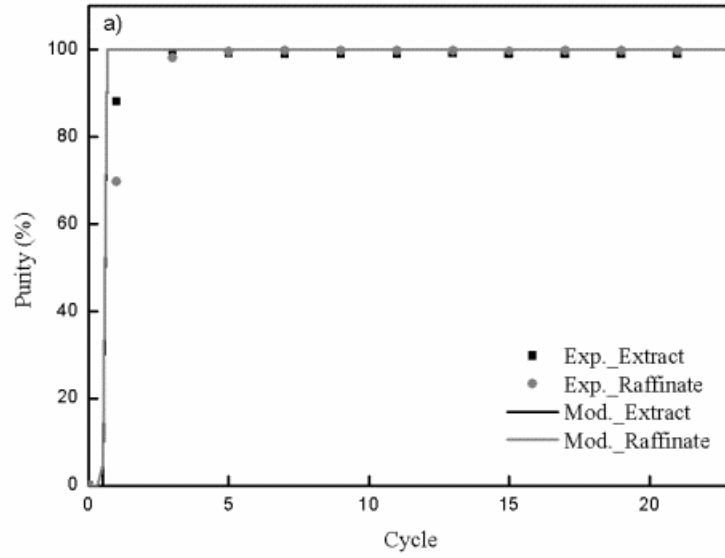


**Figure 4- 8: The experimental and simulated separation performance of Run 2.**

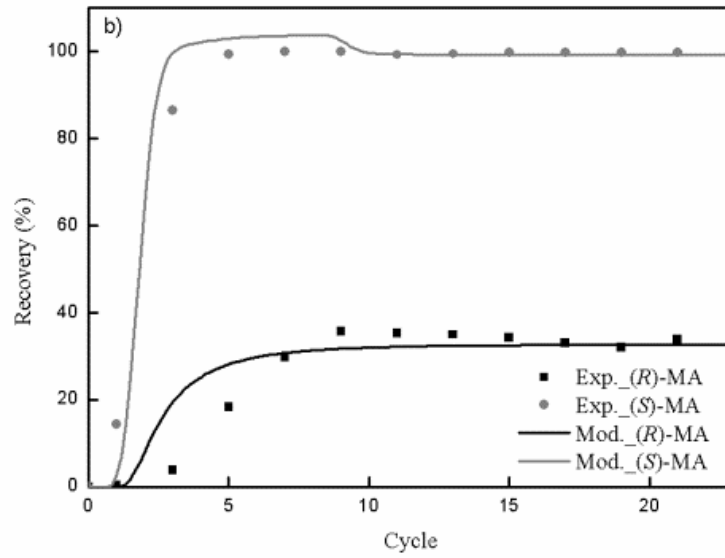
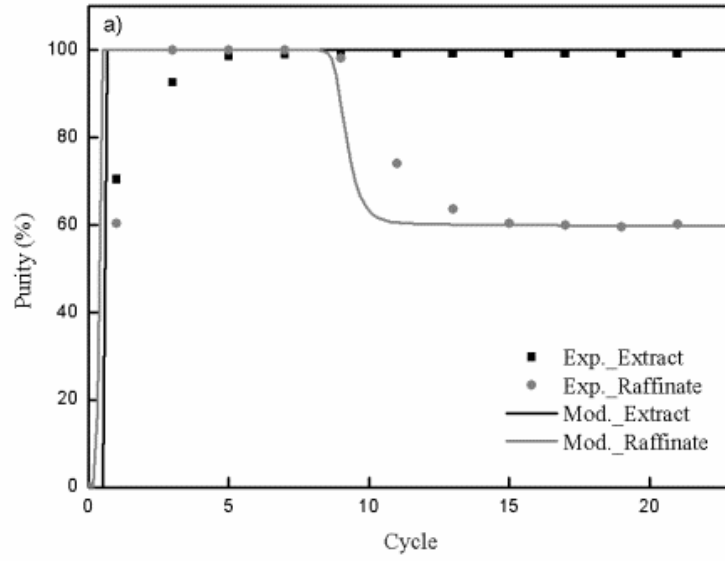


Figure 4- 9: The experimental and simulated separation performance of Run 6.

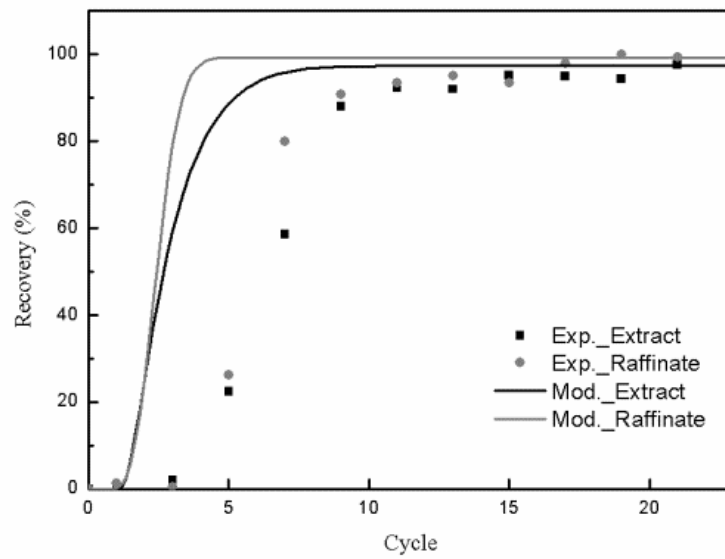
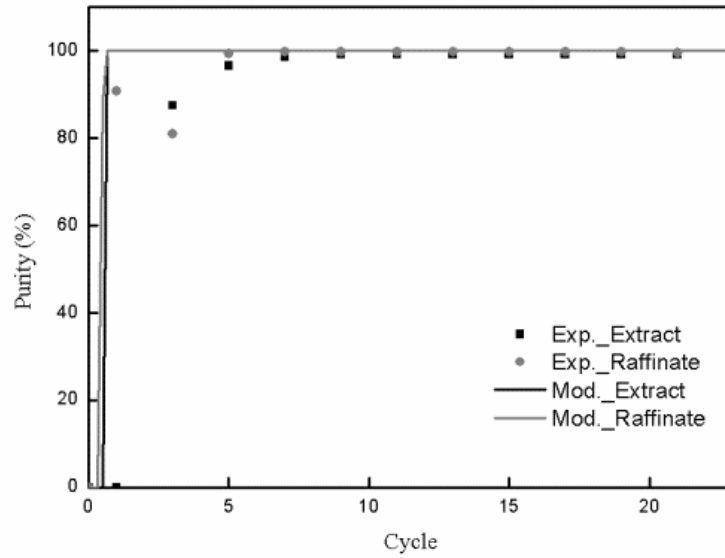


Figure 4- 10: The experimental and simulated separation performance of Run 12.

## 4.6 Conclusion

The results of this study prove that the racemic mandelic acid can be successfully separated on the Chiralcel OD columns using the four-section SMB unit. The dynamic behaviour of the SMB was simulated by the transport dispersive column model with a competitive modified Langmuir isotherm. The triangle theory was used to design of SMB. 13 experiments were performed to study the effect of the operation conditions on the SMB performance. With the switching time increasing, the raffinate recovery grows while the (*R*)-MA in extract stream declines. The raffinate purity decreases while the extract purity increases by the switching time increasing from 3 to 3.5 min. However, both of the raffinate and extract purities decline steeply when the switching time reaches 3.7 min. Increasing feed concentrations causes the purity and recovery of extract and raffinate stream decrease. And extract purity and recovery and raffinate purity also decrease when the feed flow rate decreases. With the extract flow rate increasing, the purities of raffinate and extract streams increase. The column set 1/2/2/1 is superior to 1/1/1/1 with the higher purities and recoveries of extract and raffinate. The SMB model and parameters are robust and can be used to predict the separation process on SMB with satisfactory accuracy.

## 4.7 Reference

1. Ahuja, S., *Chiral separation methods for pharmaceutical and biotechnological products*. 2010, Hoboken: Wiley Online Library.
2. Kurihara, N., et al., *Chirality in synthetic agrochemicals: bioactivity and safety considerations*. Pesticide Science, 1999. **55**(2): p. 219-219.
3. Maier, N.M., P. Franco, and W. Lindner, *Separation of enantiomers: needs, challenges, perspectives*. Journal Of Chromatography A, 2001. **906**(1): p. 3-33.
4. Nicoud, R.M., et al., *Preparative scale enantioseparation of a chiral epoxide: Comparison of liquid chromatography and simulated moving bed adsorption technology*. Chirality, 1993. **5**(4): p. 267-271.
5. Wan, H. and L.G. Blomberg, *Chiral separation of amino acids and peptides by capillary electrophoresis*. Journal Of Chromatography A, 2000. **875**(1): p. 43-88.
6. Subramanian, G., *Chiral separation techniques: a practical approach*. 2007, Weinheim: Vch Verlagsgesellschaft Mbh.
7. Svang-Ariyaskul, A., W.J. Koros, and R.W. Rousseau, *Chiral separation using a novel combination of cooling crystallization and a membrane barrier: Resolution of DL-glutamic acid*. Chemical Engineering Science, 2009. **64**(9): p. 1980-1984.
8. Feibush, B., et al., *Chiral separation of heterocyclic drugs by HPLC: solute-stationary phase base-pair interactions*. Journal Of The American Chemical Society, 1986. **108**(12): p. 3310-3318.
9. Gübitz, G., *Separation of drug enantiomers by HPLC using chiral stationary phases—a selective review*. Chromatographia, 1990. **30**(9): p. 555-564.
10. Loun, B. and D.S. Hage, *Chiral separation mechanisms in protein-based HPLC columns. 2. Kinetic studies of (R)-and (S)-warfarin binding to immobilized human serum albumin*. Analytical Chemistry, 1996. **68**(7): p. 1218-1225.
11. Tang, Y., *Significance of mobile phase composition in enantioseparation of chiral drugs by HPLC on a cellulose-based chiral stationary phase*. Chirality, 1996. **8**(1): p. 136-142.
12. Guiochon, G., *Preparative liquid chromatography*. Journal Of Chromatography A, 2002. **965**(1): p. 129-161.
13. Broughton, D.B. and C.G. Gerhold, *Continuous sorption process*. 1961.
14. Negawa, M. and F. Shoji, *Optical resolution by simulated moving-bed adsorption technology*. Journal of Chromatography A, 1992. **590**(1): p. 113-117.



15. Blehaut, J. and R.M. Nicoud, *Recent aspects in simulated moving bed*. *Analisis*, 1998. **26**(7): p. M60-M70.
16. Schulte, M. and J. Strube, *Preparative enantioseparation by simulated moving bed chromatography*. *Journal of Chromatography A*, 2001. **906**(1-2): p. 399-416.
17. Rajendran, A., G. Paredes, and M. Mazzotti, *Simulated moving bed chromatography for the separation of enantiomers*. *Journal of Chromatography A*, 2009. **1216**(4): p. 709-738.
18. Marle, I., et al., *Separation of enantiomers using cellulase (CBH I) silica as a chiral stationary phase*. *Journal of Chromatography A*, 1991. **586**(2): p. 233-248.
19. Küsters, E., G. Gerber, and F. Antia, *Enantioseparation of a chiral epoxide by simulated moving bed chromatography using Chiralcel-OD*. *Chromatographia*, 1995. **40**(7-8): p. 387-393.
20. Miller, L., et al., *Preparative chromatographic resolution of enantiomers using polar organic solvents with polysaccharide chiral stationary phases*. *Journal of Chromatography A*, 1999. **865**(1-2): p. 211-226.
21. Ikai, T. and Y. Okamoto, *Preparation and Chiral Recognition of Polysaccharide-Based Selectors*, in *Chiral Recognition in Separation Methods*, A. Berthod, Editor. 2010, Springer-Verlag: Berlin, Heidelberg. p. 33.
22. Lisec, O., P. Hugo, and A. Seidel-Morgenstern, *Frontal analysis method to determine competitive adsorption isotherms*. *Journal Of Chromatography A*, 2001. **908**(1-2): p. 19-34.
23. Gritti, F. and G. Guiochon, *Influence of a buffered solution on the adsorption isotherm and overloaded band profiles of an ionizable compound*. *Journal of Chromatography A*, 2004. **1028**(2): p. 197-210.
24. Zhang, Y., S. Rohani, and A.K. Ray, *Numerical determination of competitive adsorption isotherm of mandelic acid enantiomers on cellulose-based chiral stationary phase*. *Journal of Chromatography A*, 2008. **1202**(1): p. 34-39.
25. Susanto, A., et al., *Model Based Design and Optimization*, in *Preparative Chromatography*, H. Schmidt-Traub, Editor. 2005, Wiley-VCH Weinheim. p. 313-369.
26. Pais, L.S., J.M. Loureiro, and A.E. Rodrigues, *Separation of enantiomers of a chiral epoxide by simulated moving bed chromatography*. *Journal Of Chromatography A*, 1998. **827**(2): p. 215-233.
27. Mao, S., et al., *Chromatographic Resolution and Isotherm Determination of (R,S)-Mandelic Acid on Chiralcel-OD Column*. *Journal of Separation Science*, 2012.

## **Chapter 5**

### **Kinetics of (*R,S*)- and (*R*)-Mandelic Acid in an Unseeded Cooling Batch Crystallizer**

A version of this chapter was published as:

Mao, S.; Zhang, Y; Rohani, S.; Ray, A.K. Kinetics of (*R,S*)-Mandelic Acid and (*R*)-Mandelic Acid in an unseeded cooling batch crystallizer, *Journal of Crystal Growth*, 312(22), 3340-3348(2010).

## 5.1 Introduction

The recognition of differences in the pharmacological activity of enantiomeric molecules has created the need to obtain them as isolated enantiomers. Two alternative approaches, i.e. asymmetric synthesis or racemate resolution can be used to obtain the isolated enantiomers. Although remarkable progress has been achieved in the field of asymmetric synthesis in recent years, the enantiomeric excess obtained from this method is often not sufficient to fulfill the requirements of regulation authorities [1, 2]. Resolution methods are of great importance in acquiring the pure enantiomers.

Among the variety of enantioseparation methods, crystallization is a very powerful technique for preparation of pure enantiomers in the pharmaceutical industry [3, 4]. Besides the knowledge of the underlying thermodynamic equilibria, a quantitative understanding of nucleation and growth kinetics is important for the design and optimization of the process [5]. Therefore, crystallization kinetics of (*R,S*)- and (*R*)-MA was investigated respectively in an unseeded cooling batch crystallizer in this study.

Mandelic acid, as a racemic compound [6, 7], is widely used for antibacterial and the enantiomers of the mandelic acid are well known as the resolving agents in the resolution of the various other racemic mixtures. Previous studies have been concerned with the thermodynamics of mandelic acid system [8], preferential crystallization [9], and evaluation of the measurement techniques in the mandelic acid systems [10]. To the best of our knowledge, no rigorous work has been reported on the nucleation and growth kinetics parameters of the mandelic acid and the enantiomers of mandelic acid. Therefore, the crystallization kinetics parameters were obtained in this study.

To design a crystallization process and get the kinetics, knowledge of the metastable zone is essential. The solubility curve, the lower boundary of the metastable zone, can be obtained by measuring the solution concentration. The isothermal method is the classical method to measure the solubility, which requires separation of the phases prior to measurement. Recently new methods have been reported. For example, Dunuwila *et al.* [11] applied the attenuated total reflection (ATR) infrared spectroscopy to obtain the solubility without the phase separation, and Lorenz *et al.* [8] used a nonisothermal DSC method for measuring solubility of the pure enantiomers and the racemic mandelic acid. The upper bound of the metastable zone is the metastable limit, which is dependent on the cooling rate, impurity, and mixing [12]. Usually, the cloudiness of the solution detected by the naked eye, or the optical density changes detected by a focused beam reflectance measurement (FBRM) or a turbidimeter, can determine the metastable limit.

The change of solution concentration can be monitored by *in-situ* attenuated total reflection Fourier transform infrared (ATR-FTIR) spectroscopy [10, 13-16]. The FBRM is based on the characterization of the chord length distribution. In this work, FBRM was applied to detect the onset of the particle formulation during the cooling crystallization process. The principle of the ATR-FTIR is that the vibrational structure of material caused by the infrared radiation leads to the typical infrared spectrum in immediate contact with the ATR immersion probe. Since the thickness of the liquid phase barrier is larger than the depth of penetration of the exponentially decaying energy field, ATR-FTIR can be used to online measure the concentration with negligible interference from the solid phase in slurry.

We used the isothermal method and the ATR-FTIR to double check the solubility of mandelic acid systems. And ATR-FTIR coupled with FBRM was used to monitor the liquid and solid composition and determine the metastable zone width.

There are a few methods available in the literature for determination of crystallization kinetics such as the analysis of size distribution in a batch cooling crystallization [17], the induction time based on ATR-FTIR and FBRM [18], or the rigorous optimization using the population and mass balance [19-24].

The purpose of this work is to study the solubility and metastable zone limit of (*R,S*)-MA and (*R*)-MA and collect the necessary experimental data in an unseeded cooling batch crystallizer to determine the crystallization kinetics of the (*R*)-MA and (*R,S*)-MA, respectively. ATR-FTIR and FBRM data were used along with the dynamic mathematical model and optimization program to obtain the crystallization kinetics parameters of (*R,S*)-mandelic acid and (*R*)-mandelic acid.

## 5.2 Materials and methods

(*R,S*)-MA (99%) and (*R*)-MA (99%) were purchased from Alfa Aesar (Heysham Lancashire, UK). Distilled water available in the lab was used as the solvent for the crystallization process. A double jacketed 200 mL glass crystallizer, with a Teflon-coated stirrer at 300 RPM stirring rate, was used in all experiments. Temperature of the crystallizer was controlled by a Julabo FP 50 bath circulator (Allentown, PA). ATR-FTIR (Hamilton Sunstrand, Pomona, CA) was applied for online monitoring of the solute concentration continuously by IR spectra. FBRM (Lasentec, Redmond, WA) was used to

detect the onset of crystallization based on the number of the particles, the chord length of which was in the 1-10 $\mu$ m channel with a measurement duration of 5s. Malvern Mastersizer (Malvern Instruments, UK) with a Scirocco 2000 sample handling unit was used to analyze the volume mean size of final product.

### **5.2.1 Calibration for IR spectrum**

The solutions with specified amount of solute in distilled water as solvent were charged to a 200 mL glass crystallizer, mixed with a magnetic stirrer, and heated at a rate of 0.05  $^{\circ}$ C/min. The IR spectra were collected with the wave-number in the range of 800 to 1700  $\text{cm}^{-1}$  at certain temperature. The spectrum of the distilled water at room temperature was used as the background for each sample. Table 5-1 shows the solutions with different concentrations and temperatures used for obtaining the IR spectra calibration model.

**Table 5- 1: Mandelic acid solutions used for calibration model**

Construction of calibration model		Validation of calibration model
Concentration(g/L)	Temperature(°C)	Concentration(g/L)
25	15, 20, 25, 30, 35	0
50	15, 20, 25, 30, 35	53
75	15, 20, 25, 30, 35	61
90	22	73
100	25	83
110	27.1	100
115	28.6	126
120	29.7	150
125	30.9	200
130	32.1	230
135	33.0	—
140	33.7	—
180	34.6	—
250	35.2	—

## 5.2.2 Solubility determination

The solubility was measured over the temperature range from 0 to 35 °C. Precise weighted amounts of solute and solvent, the concentration of which was recorded as  $C^*$ , were mixed in the crystallizer for 1 hour. Then the temperature of the crystallizer was increased until all the solute was dissolved, and the FBRM signal showed almost zero readings. Temperature at this time was recorded as  $T_s$ .  $C^*$  is considered as the solubility at  $T_s$ . The solute concentration at that time was checked by the ATR-FTIR spectra based on the calibration model.

## 5.2.3 Measurement of metastable zone limit

To determine the metastable zone limit, the polythermal method [12] was applied. The (*R,S*)-MA and (*R*)-MA solutions of various concentrations were prepared in a 200 mL glass crystallizer. The solutions were heated to 3 °C above the saturation temperature,  $T_s$ , for 1 hour, and then cooled at 0.05 °C/min till visible crystals were detected by the FBRM measurement at temperature  $T_i$ , which was considered as the metastable zone limit. And the metastable zone width was estimated as  $\Delta T = T_s - T_i$ . The solubility of solution at this temperature was recorded as the  $C_{\Pi}^*$ .

## 5.2.4 Unseeded cooling batch crystallization

A saturated solution at the starting temperature was prepared in the crystallizer. The solution temperature was increased to 3 °C above its saturation temperature to dissolve solute crystals, if any, and kept there for 2 hours. Then the crystallizer was cooled down to saturation temperature and held at that temperature for 30 min. The experiment started



with a controlled cooling temperature profile. At the same time, ATR-FTIR and FBRM detected the change of the solute concentration in the liquid phase and the chord length in the solid phase, respectively. The different operating conditions of the seven crystallization bathes are list in Table 5-2.

**Table 5- 2: Operating parameters of cooling crystallization of (*R*, *S*)-MA and (*R*)-MA**

Parameter	<i>(R)</i> -MA		<i>(R,S)</i> -MA				
	Run1	Run2	Run3	Run4	Run5	Run6	Run7
Initial temperature (°C)	28	23	26	28	23	26	23
Mid temperature (°C)	20	15	18	20	15	18	10
Cooling rate <sup>a</sup> (°C/min)	0.04	0.04	0.05	0.04	0.04	0.05	0.04
Final temperature (°C)	15	7	15	12.5	2	12	–
Cooling rate <sup>b</sup> (°C/min)	0.1	0.1	0.1	0.1	0.1	0.1	–
Mass of solvent (g)	150	150	150	150	150	150	150
Initial total concentration (g/L)	113	90	104	203	136	172	136
Shape factor <sup>c</sup> (-)	0.5			1.5			

a, Cooling rate from initial temperature to mid temperature.

b, Cooling rate from mid temperature to final temperature.

c, Due to the shape factor depends on the different crystal faces and crystal size, the different shape factors are applied for (*R*)-Mandelic acid and (*R*, *S*)-Mandelic acid [25].

### 5.3 Modeling

The unseeded cooling batch was considered as a perfectly mixed batch crystallizer of constant volume with the crystal breakage and agglomeration neglected. The population balance equation (PBE), Eq. (5-1), for size independent growth rate [5, 26-28] and mass balance for the solute concentration in continuous phase, Eq. (5-2), were the main equations for the model. The crystallizer temperature was dictated by the selected cooling policy.

$$\frac{\partial n(L,t)}{\partial t} + G(t) \frac{\partial n(L,t)}{\partial L} = 0 \quad (5-1)$$

$$\frac{dC_{cal}(t)}{dt} = -\rho_c k_v \frac{d\mu_2}{dt} = -3\rho_c k_v G(t) \mu_2(t) \quad (5-2)$$

where  $n$  is the population density,  $G$  is the size-independent crystal growth rate,  $C$  is the solute concentration,  $\rho_c$  is the crystal density,  $k_v$  is the volume shape factor,  $\mu_2$  is the 2nd moment of the crystal size distribution,  $\mu_2(t) = \int_0^\infty n(L,t)L^2 dL$ .

The nucleation rate per unit mass of solvent and growth rate are described by the following power-law expressions.

$$B(t) = k_b \Delta C(t)^b \quad (5-3)$$

$$G(t) = k_g \Delta C(t)^g \quad (5-4)$$

where  $B$  is the nucleation rate,  $b$  is the nucleation order,  $G$  is the growth rate,  $g$  is the growth order and  $k_b$ ,  $k_g$  are the nucleation and growth rate coefficient as functions of the temperature, given by Eqs. (5-5) and (5-6), respectively.

$$k_b = k_{b0} \exp\left(\frac{-E_b}{RT}\right) \quad (5-5)$$

$$k_g = k_{g0} \exp\left(\frac{-E_g}{RT}\right) \quad (5-6)$$

where  $k_{b0}$  and  $E_b$  are the frequency factor and the activation energy of nucleation, respectively. And  $k_{g0}$  and  $E_g$  are the frequency factor and the activation energy of growth, respectively.

$$\Delta C = C_{cal} - C^* \quad (5-7)$$

where  $C_{cal}$  is the solution concentration calculated by the crystallization model and  $C^*$  is the solubility of the solute which is the function of the temperature. And the temperature is a function of time determined by the cooling profile.

The initial and boundary conditions are

$$C(0) = C_0 \quad (5-8)$$

$$T(0) = T_0 \quad (5-9)$$

$$n(0,t) = n^0 = \frac{B(t)}{G(t)} \Big|_{L=0} \quad (5-10)$$

$$n(L,0) = 0 \quad (5-11)$$

where  $C_0$  is the initial concentration and  $T_0$  is the initial crystallizer temperature.  $n^0$  and  $n(L,0)$  are the boundary and initial condition for population density. For the unseeded crystallizer, the initial value for the  $i$ th moment of the population density was assumed to be zero.

To solve the PBE, the partial differential equation (PDE) was discretized and transformed into a set of ordinary differential equations (ODEs) with initial values. Since these ODEs were stiff, the *ode15s* function in Matlab™ was used to solve these initial value problems (IVP) – ODEs, Eqs. (5-1), (5-2), (5-10), (5-11), based on the numerical differentiation formulas (NDFs).

## 5.4 Optimization and crystallization kinetics parameter estimation

The estimated kinetics parameters can be obtained by optimization. Using the optimization toolbox in the Matlab, the optimal set of parameter values,  $[k_{b0}, E_b, b, k_{g0}, E_g, g]$ , was calculated by the nonlinear optimization *lsqnonlin* routine. The least-squares fitting was performed using *Levenberg-Marquardt* method (see Eq. (5-12))

$$\phi(k_{b0}, E_b, b, k_{g0}, E_g, g) = \min f(C_i^{cal} - C_i^{exp}) = \sum_{i=1}^N (C_i^{cal} - C_i^{exp})^2 \quad (5-$$

1

2

)

where  $N$  is the number of experimental data. The optimization was performed to minimize the difference of concentration between the experimental and the predicted values by the dynamic model equation based on the successive guess values of the kinetic parameters. The optimization was validated by the measured volume weighted mean size  $L_{[4,3]}$  at the end of batch by Malvern Mastersizer™.

## 5.5 Results and discussion

### 5.5.1 Calibration model

To set up a calibration model which relates the IR spectra to the solute concentration, solutions with different concentrations at various temperatures were studied by IR spectra with the wave-number in the range of 800-1700  $\text{cm}^{-1}$ . The stretching vibrations occurring in the range 1000-1300  $\text{cm}^{-1}$ , representing the carbon oxygen single bond (C-O), were used for calibration. Figure 5-1a shows the raw data of the IR spectra. It can be seen that the absorbance peaks increase proportionally with the solute concentrations. But they are insensitive to solution temperatures. (See Fig. 5-2a)

Due to the low solubility of mandelic acid system in water, the contribution of noise in the FTIR data becomes significant and obtaining an accurate solution concentration measurement is difficult. In order to reduce the effect of noise, the absorbance intensity at 1136  $\text{cm}^{-1}$  was subtracted from absorbance intensity peak heights at 1068  $\text{cm}^{-1}$  and 1192  $\text{cm}^{-1}$ , Figure 5-1b and 5-2b show that the relative peak values are changed with concentration and are almost insensitive to temperature. So, the effect of temperature on concentration measured by IR spectra can be neglected.

The least squares method was used to estimate concentration from IR spectra. The calibration model is showed in Eq. (5-13).

$$C_{\text{exp}} = 4.17e^3 \times (P_{1068} - P_{1136}) - 2.04e^3 \times (P_{1192} - P_{1136}) \quad (5-13)$$

where  $C_{\text{exp}}$  is the (*R*)-MA or (*R,S*)-MA solute concentration calculated from the ATR-FTIR calibration model.  $P_{1068}$ ,  $P_{1136}$  and  $P_{1192}$  are the intensity values of absorbance peaks at 1068, 1136 and 1192  $\text{cm}^{-1}$ , respectively. Because the IR spectra represent the functional groups, not the optical rotation, the (*R*)-MA or (*R,S*)-MA in water can use the same calibration model to represent its solute concentrations.

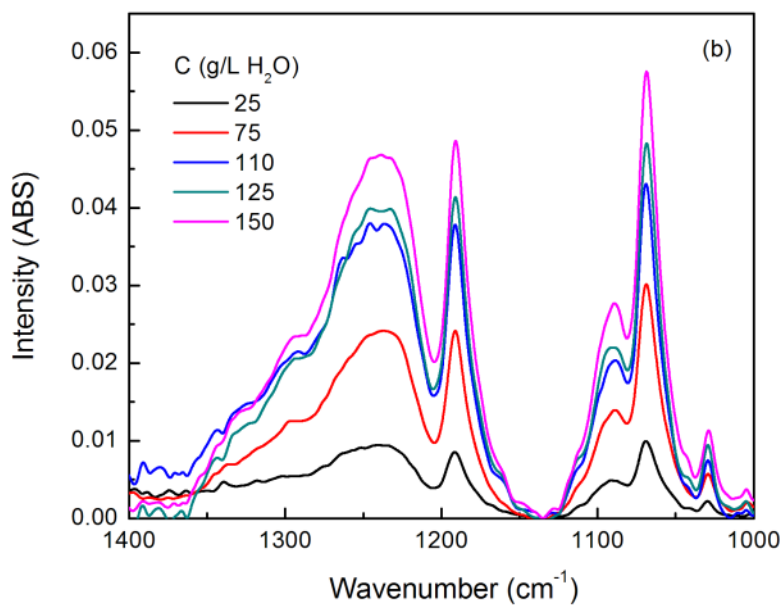
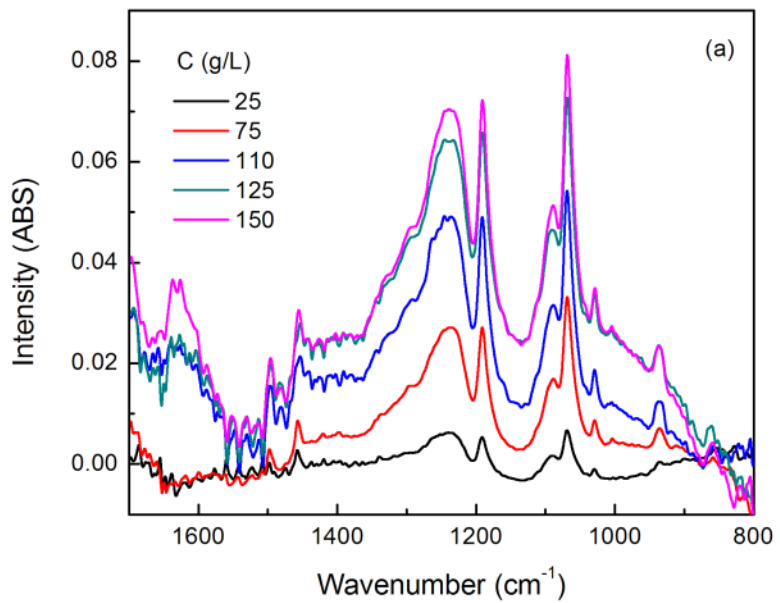


**Figure 5- 1: IR spectra of mandelic acid water solutions with different concentrations. (a, raw data; b, intensity difference with respect to the intensity height at  $1136 \text{ cm}^{-1}$  )**

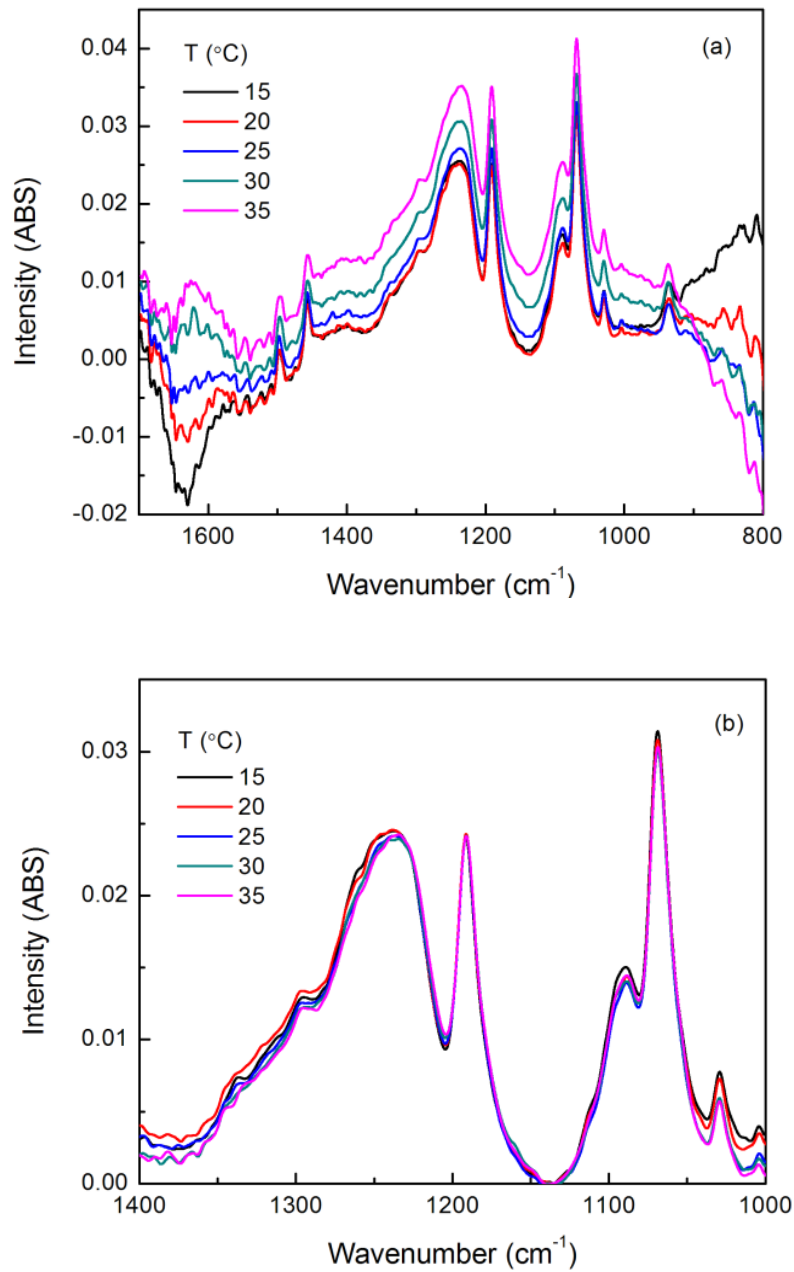


**Figure 5- 2: IR spectra of mandelic acid water solution at various temperatures. (a, raw data; b, intensity difference with respect to the intensity height at 1136 cm<sup>-1</sup> )**



The experimental data to validate the calibration model are showed in the Table 5-1. Comparison of the concentrations measured by gravimetry and those calculated from the calibration model is shown in Figure 5-3. Solubility data of mandelic acid system by the gravimetry and the ATR-FTIR methods are also compared in Figure 5-4. The standard deviations of solubility data between the two methods are less than 1.23 for (*R,S*)-MA and 2.11 for (*R*)-MA. These results show that the calibration model can accurately represent the actual solute concentration. Therefore, *in-situ* ATR-FTIR can be applied to monitor the concentration change in the cooling batch based on this calibration model.

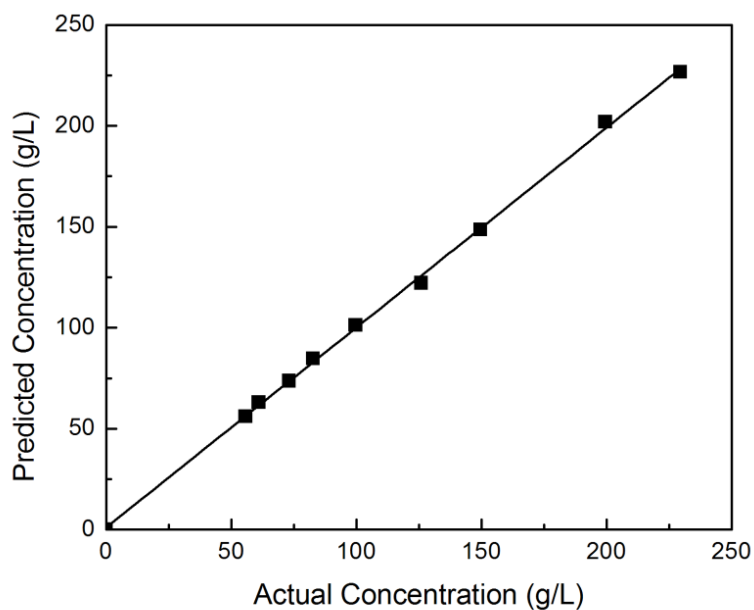


**Figure 5- 3: Concentration measurement from gravimetry method and from the ATR-FTIR calibration model at different temperatures.**

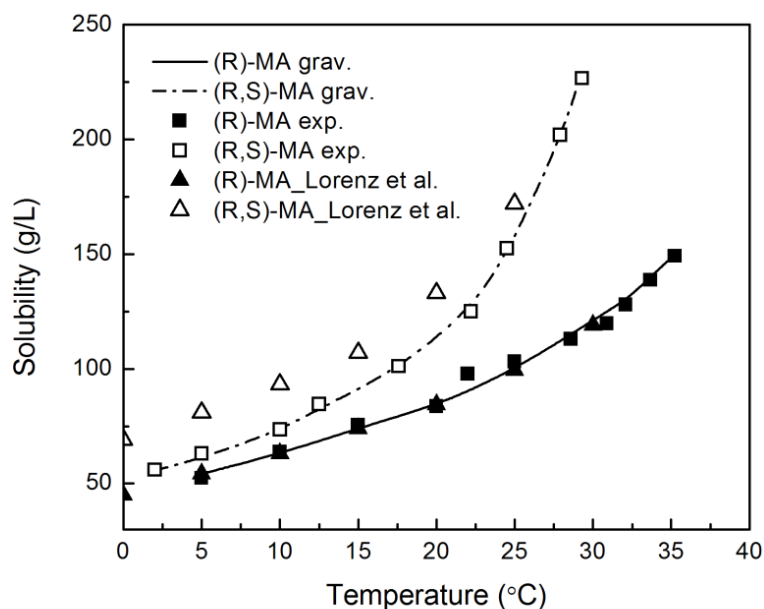


**Figure 5- 4: Solubility curves for (R)-MA and (R,S)-MA in water.**

## 5.5.2 Solubility

Measurement of the precise solubility is essential for obtaining the supersaturation. The ATR-FTIR spectra were used to determine the solubility of (R)-MA and (R,S)-MA within the temperature range from 0 to 35 °C based on the calibration model above. The solubilities of (R)-MA and (R,S)-MA as functions of the temperature are presented in Figure 5-4 showing reasonably good agreement with Lorenz *et al.* [8]. The slight scatter of the solubility can be contributed to the presence of impurities in the samples and water, and the fluctuations in the operating conditions during the experiment.

From the Figure 5-4, the solubility curves increase with the temperature especially beyond 30 °C. The difference between the solubility of (R,S)-MA and (R)-MA is much larger at higher temperatures. The racemic compound in solid form comprises of two

enantiomers coexisting in the same unit cell, which is different from the pure enantiomer. The attractive forces between different enantiomers in the same unit cell are weaker compared with those between the same enantiomers, which leads to higher solubility of the (*R,S*)-MA. The solubility data of (*R*)-MA and (*R,S*)-MA can be expressed by Eq. (5-14) and (5-15). The coefficients of polynomial were obtained by the least squares method.

$$C_{R\_MA}^* = 7.95e^{-2} \times T^2 - 1.44 \times T + 54.4 \quad (5-14)$$

$$C_{RS\_MA}^* = 2.69e^{-2} \times T^3 - 9.64e^{-1} \times T^2 + 11.5 \times T + 45 \quad (5-15)$$

### 5.5.3 Metastable zone width (MSZW)

The metastable zone is one of the most important prerequisites to study the primary nucleation and it is also very useful to study the chiral resolution by crystallization process. It is the region between the saturation of the solution and the maximum supersaturation of the solution, which is considered as the critical point for the spontaneous crystallization. When the supersaturation exceeds the metastable limit, the nuclei are born. The level of the nuclei burst depends on the degree of supersaturation, which will be discussed in section 5.5.5. This phenomenon can also be uncovered by the ATR-FTIR data which indicate the solution concentration is nearly constant during the metastable zone and the supersaturation significantly falls beyond the metastable zone limit.

The metastable zone width can be expressed by the maximum attainable supercooling of the metastable zone,  $\Delta T_{max} = T_s - T_b$ , or the maximum attainable supersaturation  $\Delta C_{max}$

$= C^* - C^*_{\pi}$ . It is affected by many factors, i.e. saturation temperature, the physical purity of the solution, the cooling rate, the seeds, the stirrer speed, and the solvent used.

The metastable zones of (*R,S*)-MA and (*R*)-MA in water are illustrated in Figure 5-5. Both of the metastable limits increase with the increase in temperature. Moreover,  $\Delta T_{max}$  increases as the initial concentration decreases. Runs 5 and 7 (See Fig. 5-10) show that the maximum supersaturation appears earlier as the cooling rate decreases. In other words, the metastable zone is wider at higher cooling rates. This is the reason that the slower cooling rate makes the solution reaches saturation faster. From Figure 5-5, it is evident that the MSZW of (*R*)-MA is narrower than that of (*R,S*)-MA. The same phenomenon has been reported in other racemic compound [29]. This is because more time is needed to form the crystals of the racemic compound due to the rearrangement of R and S molecules, compared to the time needed for the enantiomer pure crystals.

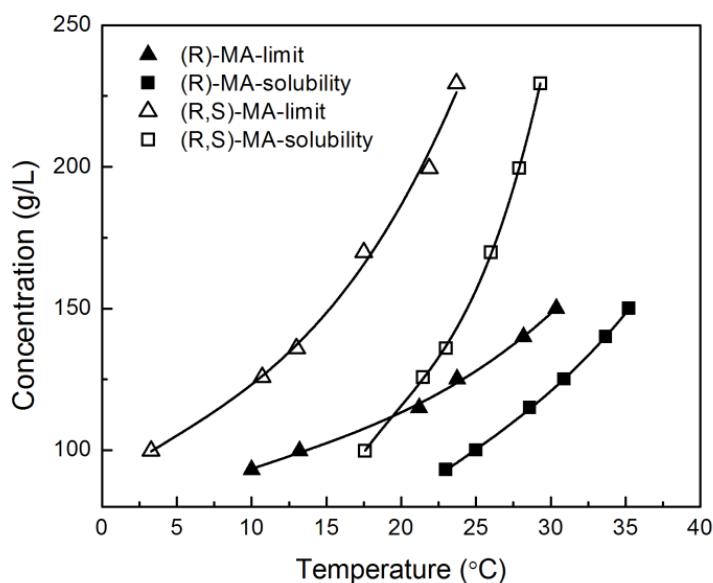


**Figure 5- 5: Metastable zone limits of (*R*)-MA and (*R,S*)-MA in water.**

#### 5.5.4 Kinetics estimation, optimization and validation

Four crystallization cooling batches were performed to study the kinetics of mandelic acid system, two batches for (*R*)-MA, Runs 1 and 2, and two batches for (*R,S*)-MA, Runs 4 and 5. The optimal nucleation and growth kinetic parameters are list in Table 5-3. With the optimized value, the concentration profiles calculated by the simulation compared with the experimental data are showed in Figure 5-6. The standard deviations for liquid concentration in crystallizer are 1.5 for Run 1, 1.9 for Run 2, 3.02 for Run 4 and 2.68 for Run 5. Although the ATR-FTIR spectra show some fluctuations, the results show a good agreement with those from the experiment. From the Figure 5-6, it can be noted that the solute concentration drops earlier when the initial concentration is higher. And with the same initial saturation temperature, the (*R*)-MA crystallizes earlier than (*R,S*)-MA, which is in accordance with the results in section 5.5.5.

**Table 5- 3: Estimated kinetics parameters**

Kinetic parameter	Estimated value	
	( <i>R</i> )-MA	( <i>R,S</i> )-MA
<i>b</i>	1.73 ± 0.26	1.56 ± 0.08
$k_{b0} \times 10^{-8}$ (No./L/s)(g/L) <sup>b</sup>	3.11 ± 0.16	55.5 ± 3.52
$E_b$ (kJ/mol)	37.97 ± 0.71	41.17 ± 1.68
<i>g</i>	1 ± 0.01	0.8 ± 0.12
$k_{g0} \times 10^{-2}$ (μm/s)(g/L) <sup>g</sup>	2.63 ± 0.17	3.38 ± 0.35
$E_g$ (kJ/mol)	24.57 ± 0.34	28.73 ± 0.59

Note: Confidence interval of the data above at the confidence level = 95% .

The optimal kinetics parameters listed in the Table 5-3 were used in the crystallization model to calculate the concentration profiles in Run 3 for (*R*)-MA and Runs 6 and 7 for (*R,S*)-MA (see Fig. 5-7). Those standard deviations for liquid concentration in crystallizer are less than 4. The calculated and experimental results of the final volume-weighted mean particle sizes are list in Table 5-4, which show that they are in good agreement. From the comparisons above, the estimated kinetics parameters and the crystallization model are proved to be reliable.

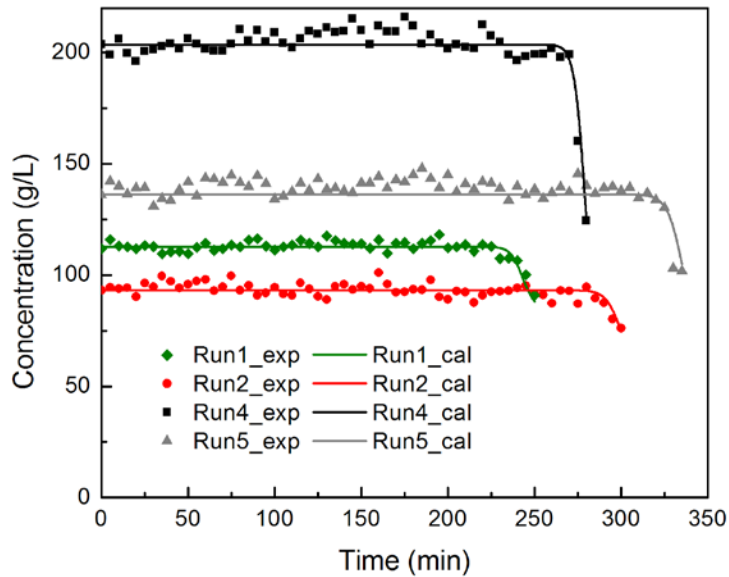


**Figure 5- 6: (R)-MA and (R,S)-MA concentration profiles by experimental measurement and model prediction.**

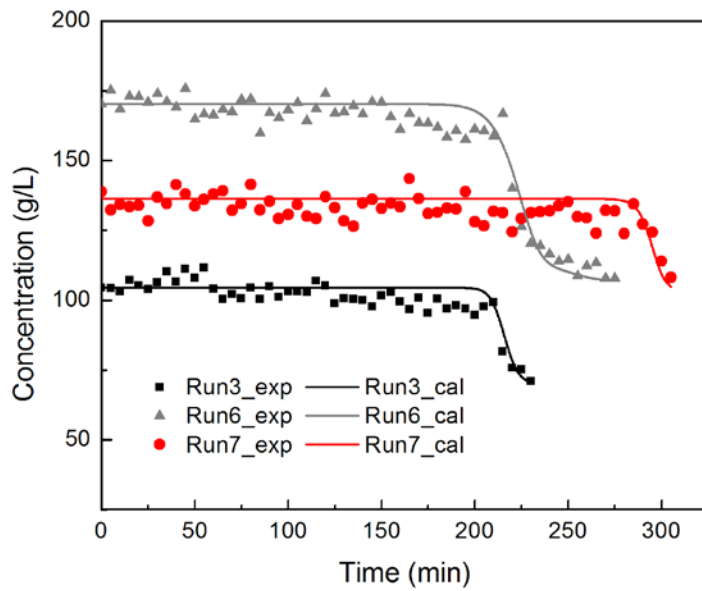


**Figure 5- 7: Model validation based on concentration profiles.**

**Table 5- 4: Comparison of volume weighted mean size**

Run	$L_{[4,3]}$ for Experiment	$L_{[4,3]}$ for Simulation	Relative deviation
1	327.53	325	0.01
2	360.18	354	0.02
4	115.53	110	0.05

Note: the relative deviation is defined by  $\frac{L_{[4,3]}^{\text{exp}} - L_{[4,3]}^{\text{sim}}}{L_{[4,3]}^{\text{exp}}}$ .

### 5.5.5 Supersaturation

The supersaturation was determined by the difference between solution concentration and the saturation concentration at the same temperature,  $\Delta C = C - C^*$ . Supersaturation is the driving force for the nucleation and growth of fresh nuclei in the unseeded cooling batch crystallization. In this study, the effects of initial concentration and cooling rate on the supersaturation are discussed below.

#### 5.5.5.1 Initial saturation concentration effect

Comparing Run 1 with Run 2, the supersaturations with the different initial saturation concentrations are shown in Figure 5-8a. The supersaturation is higher at higher initial concentration. It can be explained that, in mandelic acid system,  $\Delta C_{max}$  increases as the initial saturation concentration increases. And a smaller  $\Delta T_{max}$  at high initial saturated concentration makes the peak in supersaturation appear earlier. The earlier and larger



supersaturation leads to the earlier nucleation and higher nucleation rate, shown in Figure 5-8b. And the higher supersaturation leads to a higher nucleation rate. The result is a smaller final mean particle size [21], which can be confirmed by the final particle size analysis in Table 5-4. The same phenomenon can also be observed in (*R,S*)-MA shown in Figure 5-8d, 8e.

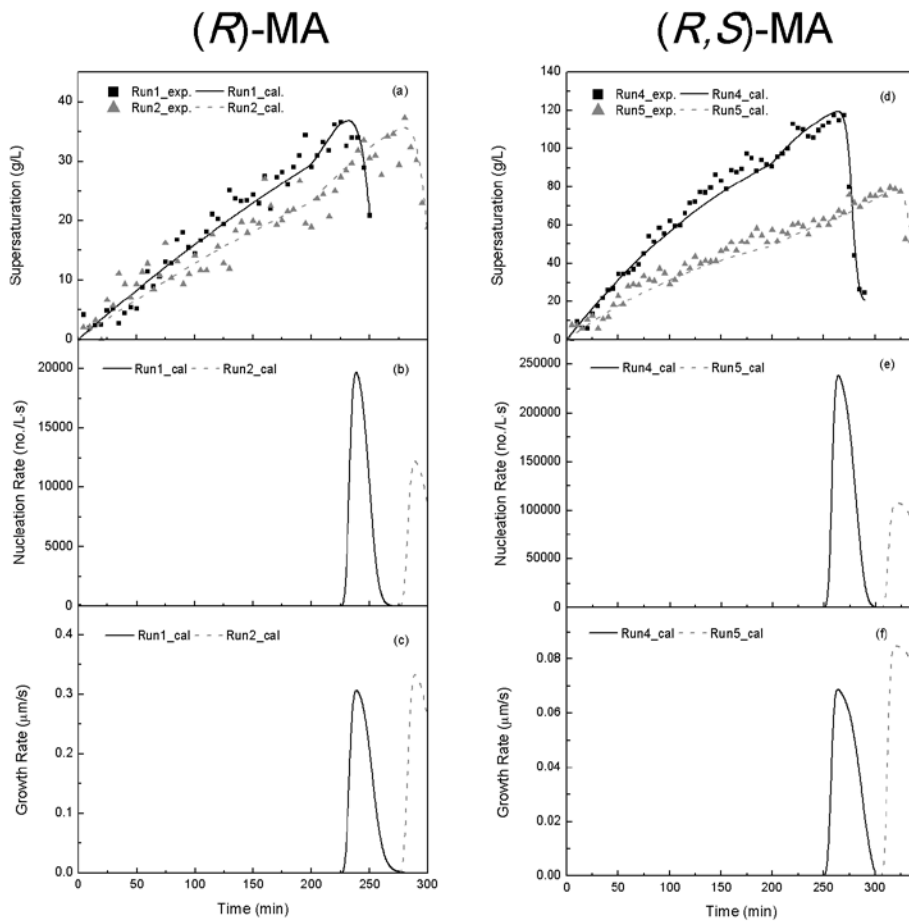


**Figure 5- 8: Effect of initial concentration on the nucleation and growth rate of (*R*)-MA and (*R,S*)-MA.**

The difference of the supersaturation and the nucleation rate between the (*R*)-MA and (*R,S*)-MA with the same initial saturation temperature are shown in Figure 5-9 (for Runs 1 and 4). The supersaturation of (*R,S*)-MA is much larger than (*R*)-MA. And it takes more time to accumulate before the nucleation. On the other hand, the nucleation rate for (*R*)-MA is slower than (*R,S*)-MA. Therefore, the  $L_{[4,3]}$  of (*R*)-MA is much bigger than that of (*R,S*)-MA shown in Table 5-4 and Figure 5-9c.

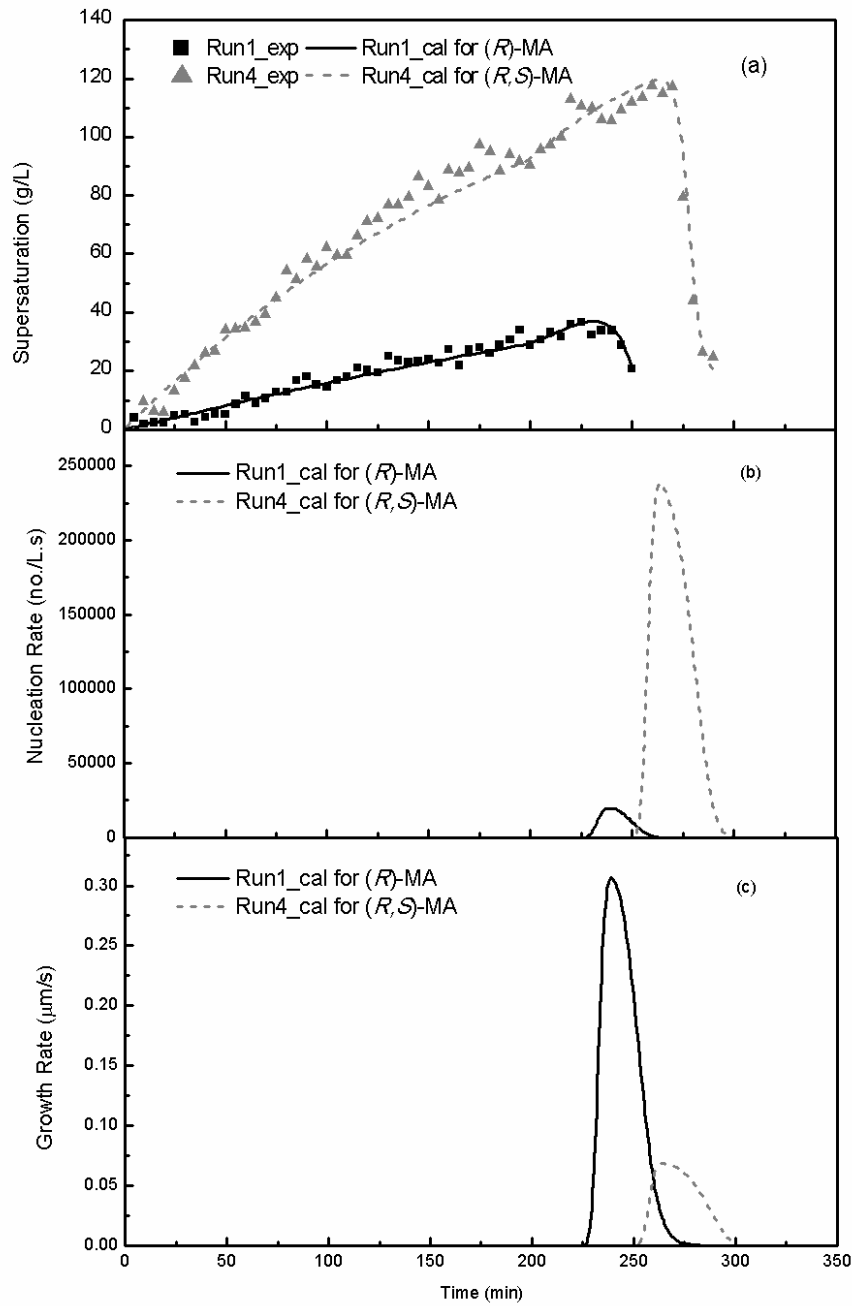


**Figure 5- 9: Comparison of nucleation and growth rates of (R)-MA and (R,S)-MA with the same initial saturated temperature.**

### **5.5.5.2 Cooling rate effect**

For Run 5, the initial cooling rate was 0.04 °C/min and 0.1 °C/min after 200 min. And the constant cooling rate for Run 7 was 0.04 °C/min (see Fig. 5-10a). Figure 5-10a shows that after 200 min, the supersaturation for Run 5 increases as the cooling rate increases. And the maximum supersaturation corresponding to the lower cooling rate occurs earlier than that of the higher cooling rate. Therefore, the metastable zone width will be narrower at the lower cooling rate. That makes the primary nucleation happen earlier and the nucleation rate lower as shown in Figure 5-10b.

# (R,S)-MA

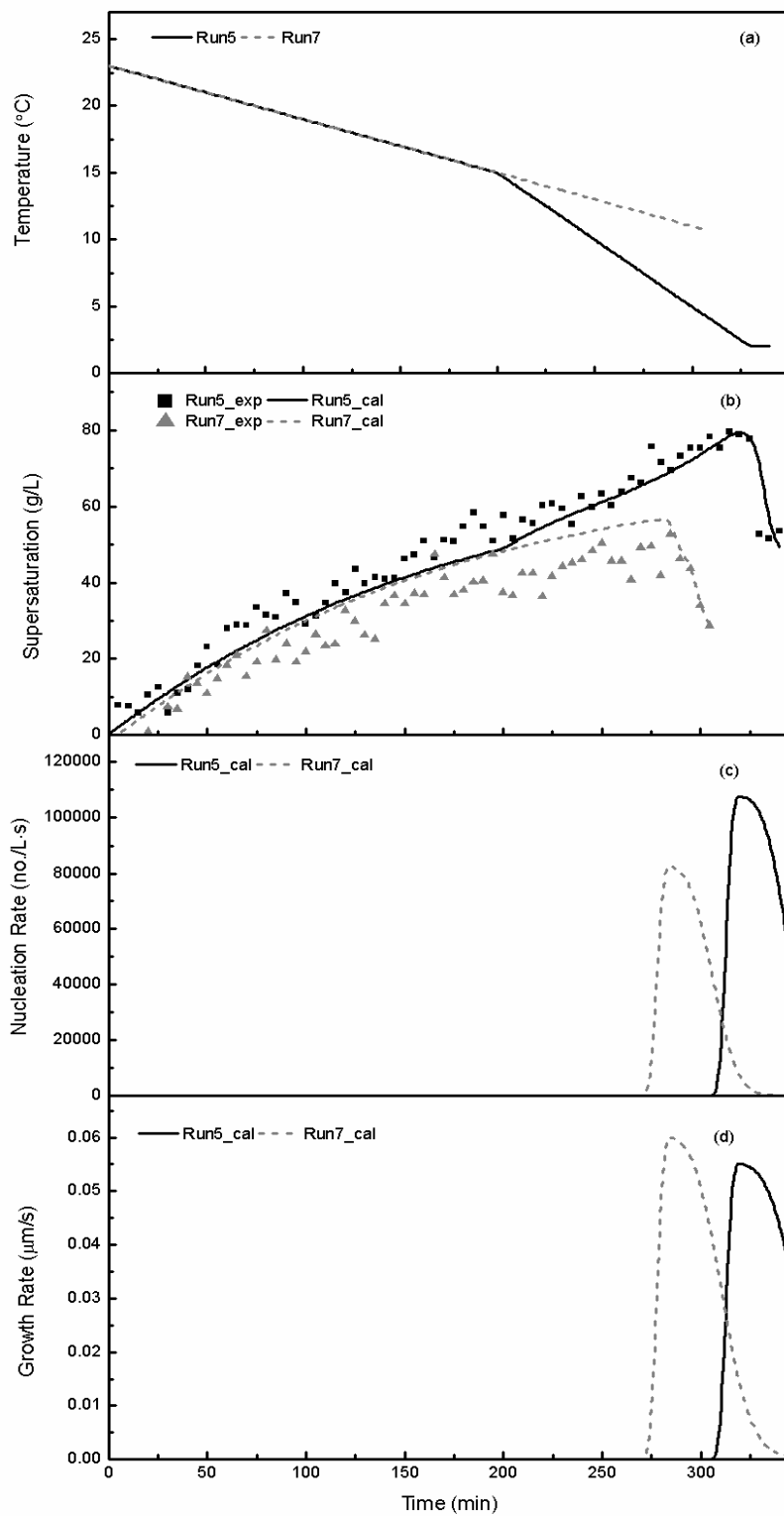


Figure 5- 10: Effect of cooling rate on the nucleation and growth rates of (R,S)-MA.

## 5.6 Conclusion

The kinetics of (*R,S*)-MA and (*R*)-MA in an unseeded cooling batch crystallizer were experimentally investigated. The *in-suit* ATR-FTIR was used to obtain accurate liquid concentration using a robust calibration model. The FBRM was applied to monitor the onset of crystallization. The solubility of the (*R,S*)-MA is higher than that of the (*R*)-MA and the difference is smaller at lower temperatures. The metastable zone (MSZ) of mandelic acid system is wider at higher temperatures. And the MSZ of the (*R,S*)-MA is wider than that of the (*R*)-MA. Moreover, the nucleation rate increases with increase of the initial concentration and cooling rate. The nucleation of (*R*)-MA occurs at lower supersaturations compared to that of (*R,S*)-MA under the same initial temperature. Moreover, high initial concentration and cooling rate cause a smaller final particle size. The kinetics parameters of nucleation and growth rates for the (*R*)-MA and (*R,S*)-MA systems in unseeded cooling batch crystallizers were obtained.

## 5.7 Reference

1. Subramanian, G., *Chiral separation techniques: a practical approach*. 2007: Vch Verlagsgesellschaft Mbh.
2. Rouhi, A.M., *Chiral Chemistry: Traditional methods thrive despite numerous hurdles, including tough luck, slow commercialization of catalytic processes*. Chemical & Engineering News, 2004. **82**(Journal Article): p. 47-62.
3. Ahuja, S., *Chiral separations and technology: an overview*. Chiral Separations, 1996.
4. Sheldon, R.A., *Chirotechnology :industrial synthesis of optically active compounds*. 1993, New York: Marcel Dekker. 423.
5. Randolph, A.D. and M.A. Larson, *Theory of particulate processes: analysis and techniques of continuous crystallization*. Vol. 1. 1971: Academic Press San Diego, CA.
6. Jacques, J., A. Collet, and S.H. Wilen, *Enantiomers, racemates, and resolutions*. 1981, New York ;; Toronto: Wiley. 447.
7. Lorenz, H. and A. Seidel-Morgenstern, *A contribution to the mandelic acid phase diagram*. Thermochemica Acta, 2004. **415**(1-2): p. 55-61.
8. Lorenz, H., D. Sapoundjiev, and A. Seidel-Morgenstern, *Enantiomeric Mandelic Acid System-Melting Point Phase Diagram and Solubility in Water*. Journal of Chemical & Engineering Data, 2002. **47**(5): p. 1280-1284.
9. Alvarez Rodrigo, A., H. Lorenz, and A. Seidel-Morgenstern, *Online monitoring of preferential crystallization of enantiomers*. Chirality, 2004. **16**(8): p. 499-508.
10. Perlberg, A., H. Lorenz, and A. Seidel-Morgenstern, *Crystal Growth Kinetics via Isothermal Seeded Batch Crystallization: Evaluation of Measurement Techniques and Application to Mandelic Acid in Water*. Industrial & Engineering Chemistry Research, 2005. **44**(4): p. 1012-1020.
11. Dunuwila, D.D., L.B. Carroll Ii, and K.A. Berglund, *An investigation of the applicability of attenuated total reflection infrared spectroscopy for measurement of solubility and supersaturation of aqueous citric acid solutions*. Journal of Crystal Growth, 1994. **137**(3-4): p. 561-568.
12. Nývlt, J., *The Kinetics of industrial crystallization*. Chemical engineering monographs ;. Vol. 19. 1985, Amsterdam ;; New York: Elsevier ;. 350.

13. Togkalidou, T., et al., *Solution concentration prediction for pharmaceutical crystallization processes using robust chemometrics and ATR FTIR spectroscopy*. Organic Process Research & Development, 2002. **6**(3): p. 317-322.
14. Yu, Z.Q., P.S. Chow, and R.B.H. Tan, *Application of Attenuated Total Reflectance–Fourier Transform Infrared (ATR–FTIR) Technique in the Monitoring and Control of Anti-solvent Crystallization*. Industrial & Engineering Chemistry Research, 2006. **45**(1): p. 438-444.
15. Bakhbaki, Y., P. Charpentier, and S. Rohani, *The Solubility of Phenanthrene in Toluene: In-situ ATR-FTIR, Experimental Measurement, and Thermodynamic Modelling*. The Canadian Journal of Chemical Engineering, 2005. **83**(2): p. 267-273.
16. Schöll, J., et al., *Antisolvent Precipitation of PDI 747: Kinetics of Particle Formation and Growth*. Crystal Growth & Design, 2007. **7**(9): p. 1653-1661.
17. Al Nasser, W., et al., *Determining kinetics of calcium carbonate precipitation by inline technique*. Chemical Engineering Science, 2008. **63**(5): p. 1381-1389.
18. Schöll, J., et al., *Precipitation of L-Glutamic Acid: Determination of Nucleation Kinetics*. Chemical Engineering & Technology, 2006. **29**(2): p. 257-264.
19. Tavare, N. and J. Garside, *Simultaneous estimation of crystal nucleation and growth kinetics from batch experiments*. Chemical Engineering Research & Design, 1986. **64**(2): p. 109-118.
20. Qiu, Y. and Å.C. Rasmuson, *Estimation of crystallization kinetics from batch cooling experiments*. AIChE Journal, 1994. **40**(5): p. 799-812.
21. Mohameed, H.A., B. Abu-Jdayil, and M. Al Khateeb, *Effect of cooling rate on unseeded batch crystallization of KCl*. Chemical Engineering and Processing, 2002. **41**(4): p. 297-302.
22. Ouiazzane, S., et al., *Estimation of sucrose crystallization kinetics from batch crystallizer data*. Journal of Crystal Growth, 2008. **310**(4): p. 798-803.
23. Hu, Q., et al., *Nonlinear kinetic parameter estimation for batch cooling seeded crystallization*. AIChE Journal, 2004. **50**(8): p. 1786-1794.
24. Trifkovic, M., M. Sheikhzadeh, and S. Rohani, *Kinetics Estimation and Single and Multi-Objective Optimization of a Seeded, Anti-Solvent, Isothermal Batch Crystallizer*. Industrial & Engineering Chemistry Research, 2008. **47**(5): p. 1586-1595.
25. Budz, J., A.G. Jones, and J.W. Mullin, *On the Shape-Size Dependence of Potassium Sulfate Crystals*. Industrial & Engineering Chemistry Research, 1987. **26**(4): p. 820-824.



26. Borissova, A., et al., *Modeling the Precipitation of l-Glutamic Acid via Acidification of Monosodium Glutamate*. *Crystal Growth & Design*, 2005. **5**(3): p. 845-854.
27. Cornel, J., C. Lindenberg, and M. Mazzotti, *Experimental Characterization and Population Balance Modeling of the Polymorph Transformation of l-Glutamic Acid*. *Crystal Growth and Design*, 2009. **9**(1): p. 243-252.
28. Zhang, Y., et al., *Nucleation and Growth Kinetics of (R)-Mandelic Acid from Aqueous Solution in the Presence of the Opposite Enantiomer*. *Crystal Growth & Design*, 2010. **10**(7): p. 2879-2887.
29. Wang, X., et al., *Intrinsic MSZW characteristics of racemic species: Implication for chiral crystallization*. *AIChE Journal*, 2008. **54**(9): p. 2281-2292.

## **Chapter 6**

### **Conclusions and Recommendations**

A systematic study of the chiral separation of (*R,S*)-MA by coupling crystallization and simulated moving bed (SMB) technology was presented in this thesis. Firstly, the optimal mobile phase was chosen, and the competitive adsorption isotherm parameters, dispersion coefficient and mass transfer coefficient were determined for the liquid chromatography resolution of (*R,S*)-MA. Then, the chiral resolution of the (*R,S*)-MA by SMB was first applied in preparative scale. Finally, the kinetics of (*R*) and (*R,S*)-MA in the unseeded cooling crystallizer were obtained experimentally and numerically. Those researches proved that the required purity of the racemic compound can be achieved by simulated moving bed and then the pure enantiomers can be obtained using crystallization in the partially enriched solutions.

## **6.1 Conclusions**

### **6.1.1 Simulated moving bed**

A good mobile phase and accurate adsorption and kinetics parameters are essential for chiral resolution by the liquid chromatography method. In this thesis, the resolution of racemic mandelic acid ((*R,S*)-MA) and numerical determination of binary competitive isotherm of (*R,S*)-MA on Chiralcel OD column have been investigated. As normal phase liquid chromatographic mode was used to resolve (*R,S*)-MA in this study, the choice for mobile phase has been restricted to the non-polar or weakly polar organic solvent, usually the mixture of hydrocarbon (hexane or heptane) and alcohol. Nevertheless, (*R,S*)-MA has very limited solubility in weakly polar organic solvents. In order to increase the solubility of (*R,S*)-MA in mobile phase, strongly polar alcohol needs to be used. The results also showed that the solubility of (*R,S*)-MA increased exponentially with the increase of IPA

concentration. However, the high IPA concentration resulted in a decrease in resolution. The experimental results proved that the retention time and resolution decreased when the IPA concentration increased from 10 to 30v%. In addition, the retention time and the resolution performance were also influenced largely by TFA concentration. The retention time decreased with the increasing TFA concentration from 0 to 3v%. And the increase of TFA concentration also helped to reduce the peak broadening and improve the separation performance. But too high concentration of acidic additive could damage the column, which has been mentioned on the column manual. Therefore, hexane/IPA/TFA with 85/15/0.3 (v/v/v) was demonstrated to be the optimal mobile phase for the resolution of (*R,S*)-MA. And the competitive adsorption isotherm was first studied for the racemic compound ((*R,S*)-MA) using inverse method. The axial dispersion coefficient was measured by the molecular diffusion and eddy diffusion which was adjusted by the interstitial mobile phase velocity. Accuracy and reliability of the derived isotherm parameters were verified by comparing the model predicted band profiles with the experimental elution profiles under various experimental conditions. It also proved that the inversed method is an efficient and economical method for the determination of adsorption isotherm.

Followed by the achievement of the adsorption isotherm parameters, the chiral separation of the racemic mandelic acid ((*R,S*)-MA) by simulated moving bed chromatography with Chiralcel OD columns was investigated experimentally and numerically. The transport dispersion model combined with the competitive modified Langmuir isotherm was applied to predict the dynamic behaviour and separation performance of the SMB process. The triangle theory was used to obtain the complete

separation region of the SMB operation based on those derived isotherm parameters. 13 experiments were performed to study the effect of the operation conditions on the SMB performance. With the switching time increasing, the raffinate recovery grew to 99.3% while the (*R*)-MA in extract stream declined to 5.67%. The raffinate purity decreased from 99.69% to 81.47% while the extract purity increased from 97.60% to 99.15% by the switching time increasing from 3 to 3.5 min. However, both of the raffinate and extract purities declined steeply to 51.58% and 88.98% when the switching time reached 3.7 min. Increasing feed concentrations from 1g/L to 30g/L caused the extract purity decreased slightly from around 100% to 98.62%, whereas, the raffinate purity dropped quickly from 91.68% to 51.82%. And the extract recovery decreased from 90.94% to 7.12%. And extract purity and recovery and raffinate purity also decreased when the feed flow rate decreased. With the extract flow rate increasing from 1.9 to 2.2mL/min, the purities of raffinate and extract stream increased from 70.47% to 99.75% and 98.86% to 99.10%, respectively. The column set 1/2/2/1 was superior to 1/1/1/1 with the higher purities and recoveries of extract and raffinate. Based on the comparison of the experimental and simulated data of the SMB under different operating conditions, it was proved that the SMB model and parameters were robust and could be used to predict the separation process on SMB with satisfactory accuracy.

### **6.1.2 Crystallization**

Firstly, the solubilities of the (*R*)- and (*R,S*)-MA in the water were determined by the polythermal method with the ATR-FTIR and FBRM device from 0 to 35 °C. To overcome the effect of noise caused by temperature and system, the relative peak values

which were measured by the absorbance intensity at  $1136\text{ cm}^{-1}$  subtracted from absorbance intensity peak heights at  $1068\text{ cm}^{-1}$  and  $1192\text{ cm}^{-1}$ , were applied. The results confirmed that the relative peak height values increased proportionally with the solute concentrations, but they were insensitive to solution temperatures. The ATR-FTIR calibration models including the intensity values of absorbance peak from the IR spectrum were presented by the least squares algorithm and were validated experimentally. It was shown that *in-situ* ATR-FTIR can be used to monitor the concentration change based on the calibration models. The metastable zone limit was also measured by *in-situ* ATR-FTIR and FBRM.

The results showed that the solubility of the (*R,S*)-MA was higher than that of the (*R*)-MA and the difference was smaller at lower temperatures. The metastable zone (MSZ) of mandelic acid system was wider at higher temperatures and at higher cooling rates. And the MSZ of the (*R,S*)-MA was wider than that of the (*R*)-MA. Then, the series of experiments was performed in the unseeded cooling batch crystallizer and the concentrations in the liquid phase were monitored by *in-situ* ATR-FTIR. The kinetics parameters of nucleation and growth of the (*R,S*)-MA and (*R*)-MA were obtained. The results showed that the (*R*)-MA crystallized earlier than (*R,S*)-MA with the same initial saturation temperature and the nucleation rate for (*R*)-MA was slower than (*R,S*)-MA since the supersaturation of (*R,S*)-MA was much larger than (*R*)-MA. For both of (*R*)-MA and (*R,S*)-MA, the supersaturation was higher at higher initial concentration which led to a higher nucleation rates and a smaller final mean particle size. Meanwhile, the supersaturation increased as the cooling rate increased. And the maximum

supersaturation of the lower cooling rate occurred earlier than that of the higher cooling rate, which made the nucleation rate increase.

## **6.2 Recommendation for future work**

In this thesis, the SMB and crystallization processes do not have been combined because of the following reasons. One reason is that the SMB and crystallization units are located in different lab and the hybrid system is not available physically. Another reason is that both of the two processes are complex and it took much time to learn each process deeply. Due to the limited time of Ph.D study, there is no enough time to complete the coupling of the two processes physically and mathematically. However, the studies in this thesis confirmed the feasibility of the coupling SMB and crystallization. Furthermore, there are some recommendations for the future work as follows.

In the SMB part, the multi-objective optimization should be done aiming to maximize the productivity and purity of the enantiomers and minimize the solid and liquid usage to control the cost of the chiral stationary phase and mobile phase. Moreover, since the SMB is very sensitive to the operating conditions, it is necessary to develop the control frame work to achieve the economic optimum as well as the guarantee of the specifications of the final outlets. The evaporation should be done since the solution flowing out from the SMB is very dilute.

In the crystallization process, the optimal operation conditions should be determined by the use of a multi-objective real-time optimal control methodology in the seeded

cooling batch crystallizer to realize the requirement of the particle size distribution and the purity of the final enantiomers.

The coupling SMB and crystallization process should be attained numerically. The SMB integrated with the crystallization process should be described by the mathematical model. And the optimization and control strategy should be generated to obtain the economic operating conditions since this coupling process characterizes a very complex dynamics.



## **Appendix A: Introduction to genetic algorithm**

Holland developed a search technique named Genetic Algorithm (GE) which mimics the process of natural evolution [1]. In a GA, the strings or chromosomes are composed of a set of decision variables which is represented in binary number (0 and 1). So, each chromosome is mapped into a set of real values of decision variables within the upper and lower boundaries of each variable. Each chromosome is employed in a process model and evaluated by the objective function to reflect its fitness. Then the best solutions are selected from the strings pool through a fitness-based process. The new generation can be obtained by choosing the parents' chromosomes randomly in the selected strings pool, copying them to form a 'mating pool' and breeding the children's chromosomes by the operation similar to those in genetic reproduction. Therefore, the fitness improves and the gene pool evolves.

Reproduction, crossover and mutation are three common operators used in simple genetic algorithm (SGA) to produce a next evolved generation. It is noticed that this GA mentioned here is simple genetic algorithm (SGA) which is discerned from its various adaptations. Reproduction is to generate the mating pool where those copied chromosomes are selected stochastically based on their fitness values. But no new chromosomes are formed in this stage. Using the methods of the crossover, the new chromosomes are created by exchanging the parts of the parent chromosomes in the crossover sites. Those new chromosomes typically share the characteristics of those parents. Those traits are beneficial or deleterious for the fitness of the new chromosomes. If the new chromosomes are worse than those parents, they will be eliminated slowly

during the next few generations. Some good strings in the mating pool are not be used for the crossover and are retained to the next generation directly. Following a crossover, mutation is performed to obtain the new generation by changing a binary number at random positions in the bit string from a 0 to 1 and vice versa with a small mutation probability ( $P_{mut}$ ) in order to maintain the genetic diversity in the next generation. To avoid the similar chromosomes, the site for mutation needs to be created in the neighborhood of the current site. The algorithm is looped until the maximum number of generations is reached or the values of the objective functions become lower than specified tolerance.

For a multi-objective function optimization, the optimal solutions as non-dominated (or Pareto-optimal) solutions can be obtained by the modified SGA, called Non-dominated Sorting Genetic Algorithm (NSGA). In the NSGA, the selection operator is performed by a ranking selection method to highlight the good chromosomes and a niching method to maintain the diversity of the population, which is the only difference between NSGA and SGA. During the selection stage, some chromosomes in the initial population of strings are recognized as a first group of non-dominated fronts and each of them is assigned a dummy fitness value based on its rank in the population. Then, the fitness sharing enforces reducing the dummy fitness of the chromosomes in the densely populated area using the niching method. A chromosome in crowded neighbors in decision variable space will have a large niche count, reduce the dummy fitness value and decrease the probability of selecting that chromosome as a parent. This procedure is repeated until all the members of the first front are performed. The remaining chromosomes classified as the next front are evaluated for non-dominance. These are all

assigned a dummy fitness value that is smaller than the lowest shared fitness values. Then, the fitness sharing takes place. The ranking and sharing process will be ended when all the chromosomes in the strings pool have their dummy fitness values. Immediately after, the reproduction, crossover and mutation are carried out. It is to be noted that the non-dominated chromosomes in the first fronts with less neighbors and higher dummy fitness values have the priority into the mating pool. The left chromosomes will be preserved in the gene pool to maintain the diversity of that pool. This algorithm can deal with any number of objectives function optimization problem.

## **Reference**

1. Holland, J.H., Adaptation in natural and artificial systems. 1975: University of Michigan press.

## Appendix B: Column dimension


---

Column Name	Length(mm)	Column Diameter(mm)	Particle Diameter ( $\mu\text{m}$ )
Chiralcel OD-H	250	4.6	5
Chiralcel OD	100	10	20


---

# Appendix C: Copyrighted material and permissions

6/8/12 RightsLink® by Copyright Clearance Center

 **Copyright Clearance Center** RightsLink®

Home Account Info Help

 **CRYSTAL GROWTH**

**Title:** Kinetics of (R,S)- and (R)-mandelic acid in an unseeded cooling batch crystallizer

**Author:** Shimin Mao, Yan Zhang, Sohrab Rohani, Ajay K. Ray

**Publication:** Journal of Crystal Growth

**Publisher:** Elsevier

**Date:** 1 November 2010  
Copyright © 2010, Elsevier

Logged in as: Shimin Mao  
LOGOUT

**Order Completed**

Thank you very much for your order.

This is a License Agreement between Shimin Mao ("You") and Elsevier ("Elsevier"). The license consists of your order details, the terms and conditions provided by Elsevier, and the [payment terms and conditions](#).

[Get the printable license.](#)

License Number	2924390731494
License date	Jun 08, 2012
Licensed content publisher	Elsevier
Licensed content publication	Journal of Crystal Growth
Licensed content title	Kinetics of (R,S)- and (R)-mandelic acid in an unseeded cooling batch crystallizer
Licensed content author	Shimin Mao, Yan Zhang, Sohrab Rohani, Ajay K. Ray
Licensed content date	1 November 2010
Licensed content volume number	312
Licensed content issue number	22
Number of pages	9
Type of Use	reuse in a thesis/dissertation
Portion	full article
Format	both print and electronic
Are you the author of this Elsevier article?	Yes
Will you be translating?	No
Order reference number	
Title of your thesis/dissertation	Chiral Separation of Racemic Mandelic Acid by the Coupling Crystallization Process and Simulated Moving Bed Technology
Expected completion date	Aug 2012
Estimated size (number of pages)	150
Elsevier VAT number	GB 494 6272 12
Permissions price	0.00 USD
VAT/Local Sales Tax	0.0 USD / 0.0 GBP
Total	0.00 USD

ORDER MORE... CLOSE WINDOW

Copyright © 2012 Copyright Clearance Center, Inc. All Rights Reserved. [Privacy statement](#). Comments? We would like to hear from you. E-mail us at [customer@copyright.com](mailto:customer@copyright.com)

<http://s100.copyright.com/AppDispatchServlet> 1/1



**Title:** Chromatographic resolution and isotherm determination of (R,S)-mandelic acid on Chiralcel-OD column

**Author:** Shimin Mao, Yan Zhang, Sohrab Rohani, Ajay K. Ray

**Publication:** Journal of Separation Science

**Publisher:** John Wiley and Sons

**Date:** Jul 17, 2012

© 2012 WILEY-VCH Verlag GmbH & Co. KGaA, Weinheim

Logged in as:  
Shimin Mao  
Account #:  
3000541635

LOGOUT

### Order Completed

Thank you very much for your order.

This is a License Agreement between Shimin Mao ("You") and John Wiley and Sons ("John Wiley and Sons"). The license consists of your order details, the terms and conditions provided by John Wiley and Sons, and the [payment terms and conditions](#).

#### [Get the printable license.](#)

License Number	2970340952704
License date	Aug 15, 2012
Licensed content publisher	John Wiley and Sons
Licensed content publication	Journal of Separation Science
Licensed content title	Chromatographic resolution and isotherm determination of (R,S)-mandelic acid on Chiralcel-OD column
Licensed content author	Shimin Mao, Yan Zhang, Sohrab Rohani, Ajay K. Ray
Licensed content date	Jul 17, 2012
Start page	n/a
End page	n/a
Type of use	Dissertation/Thesis
Requestor type	Author of this Wiley article
Format	Print and electronic
Portion	Full article
Will you be translating?	No
Order reference number	
Total	0.00 USD

ORDER MORE...

CLOSE WINDOW

Copyright © 2012 [Copyright Clearance Center, Inc.](#) All Rights Reserved. [Privacy statement](#).  
Comments? We would like to hear from you, E-mail us at [customercare@copyright.com](mailto:customercare@copyright.com)

# Curriculum Vitae

## Shimin Mao

### Education

**Ph.D. candidate, Chemical & Biochemical Engineering** 2012

*The University of Western Ontario, London, Ontario*

- Research Topic: *Chiral Separation of Racemic Mandelic Acid by the Coupling Crystallization Process and Simulated Moving Bed Technology*
- Project Supervisors: Dr. Ajay Ray and Dr. Sohrab Rohani

**M.Eng., Chemical & Biochemical Engineering** 2007

*The University of Western Ontario, London, Ontario*

**B. Eng., Biological Engineering** 2006

*Chengdu University of Technology (CDUT), Chengdu, China*

### Work Experience

**Graduate Research Assistant** 2008-2012

*The University of Western Ontario, London, Ontario*

**Graduate Teaching Assistant** 2008-2011

*The University of Western Ontario, London, Ontario*

### Awards & Scholarships

**Western Engineering Scholarship** 2008-2012

*University of Western Ontario, London, ON, Canada*

### Volunteers

**Volunteering for Guide Badge Day** 2012

*University of Western Ontario, London, ON, Canada*

- Greeted and directed the participant
- Helped the girls to finish the project

## **Publications**

- **Shimin Mao**, Yan Zhang, Sohrab Rohani and Ajay K. Ray. Kinetics of (R,S)- and (R)-mandelic acid in an unseeded cooling batch crystallizer. *Journal of Crystal Growth* (2010) pp 3340-3348.
- Yan Zhang, **Shimin Mao**, Ajay K. Ray, and Sohrab Rohani. Nucleation and growth kinetics of R-MA in the presence of counter-enantiomer. *Crystal Growth & Design* (2010) pp 2879-2887.
- **Shimin Mao**, Yan Zhang, Sohrab Rohani and Ajay K. Ray. Chromatographic Resolution and Isotherm Determination of (R,S)-Mandelic Acid. *Accepted for publication in the Journal of Separation Science*.
- **Shimin Mao**, Yan Zhang, Sohrab Rohani and Ajay K. Ray. Enantioseparation of racemic mandelic acid by simulated moving bed using Chiralcel-OD. *In progress*.

## **Conference Presentation**

- Chiral Separation by the hybrid SMB-crystallization process  
Present in *61st Canadian Chemical Engineering Conference*, London, Canada **2011**  
**First Prize Award** presentation in *Research Bridges Symposium*, Sarniar, Canada **2011**